JOURNAL OF GEOPHYSICAL RESEARCH, VOL. 112, E05S03, doi:10.1029/2006JE002682, 2007



# Compact Reconnaissance Imaging Spectrometer for Mars (CRISM) on Mars Reconnaissance Orbiter (MRO)

S. Murchie,[1] R. Arvidson,[2] P. Bedini,[1] K. Beisser,[1] J.-P. Bibring,[3] J. Bishop,[4] J. Boldt,[1] P. Cavender,[1] T. Choo,[1] R. T. Clancy,[5] E. H. Darlington,[1] D. Des Marais,[4] R. Espiritu,[6] D. Fort,[1] R. Green,[7] E. Guinness,[2] J. Hayes,[1] C. Hash,[6] K. Heffernan,[1] J. Hemmler,[1] G. Heyler,[1] D. Humm,[1] J. Hutcheson,[1] N. Izenberg,[1] R. Lee,[1] J. Lees,[1] D. Lohr,[1] E. Malaret,[6] T. Martin,[7] J. A. McGovern,[1] P. McGuire,[2] R. Morris,[8] J. Mustard,[9] S. Pelkey,[9] E. Rhodes,[1] M. Robinson,[10] T. Roush,[4] E. Schaefer,[1] G. Seagrave,[1] F. Seelos,[1] P. Silverglate,[1] S. Slavney,[2] M. Smith,[11] W.-J. Shyong,[1] K. Strohbehn,[1] H. Taylor,[1] P. Thompson,[1] B. Tossman,[1] M. Wirzburger,[1] and M. Wolff[5]

Received 22 January 2006; revised 31 July 2006; accepted 24 January 2007; published 30 May 2007.

[1] The Compact Reconnaissance Imaging Spectrometer for Mars (CRISM) is a hyperspectral imager on the Mars Reconnaissance Orbiter (MRO) spacecraft. CRISM consists of three subassemblies, a gimbaled Optical Sensor Unit (OSU), a Data Processing Unit (DPU), and the Gimbal Motor Electronics (GME). CRISM's objectives are (1) to map the entire surface using a subset of bands to characterize crustal mineralogy, (2) to map the mineralogy of key areas at high spectral and spatial resolution, and (3) to measure spatial and seasonal variations in the atmosphere. These objectives are addressed using three major types of observations. In multispectral mapping mode, with the OSU pointed at planet nadir, data are collected at a subset of 72 wavelengths covering key mineralogic absorptions and binned to pixel footprints of 100 or 200 m/pixel. Nearly the entire planet can be mapped in this fashion. In targeted mode the OSU is scanned to remove most along-track motion, and a region of interest is mapped at full spatial and spectral resolution (15–19 m/pixel, 362–3920 nm at 6.55 nm/channel). Ten additional abbreviated, spatially binned images are taken before and after the main image, providing an emission phase function (EPF) of the site for atmospheric study and correction of surface spectra for atmospheric effects. In atmospheric mode, only the EPF is acquired. Global grids of the resulting lower data volume observations are taken repeatedly throughout the Martian year to measure seasonal variations in atmospheric properties. Raw, calibrated, and map-projected data are delivered to the community with a spectral library to aid in interpretation.

**Citation:** Murchie, S., et al. (2007), Compact Reconnaissance Imaging Spectrometer for Mars (CRISM) on Mars Reconnaissance Orbiter (MRO), *J. Geophys. Res.*, *112*, E05S03, doi:10.1029/2006JE002682.

## 1. Introduction

[2] The MRO mission's primary objectives are (1) to characterize seasonal variations in dust and ice aerosols and water content of surface materials, recovering science lost with the failure of the Mars Climate Orbiter (MCO), (2) to search for evidence of aqueous and/or hydrothermal activity, and (3) to map and characterize the composition, geology, and stratigraphy of surface deposits. Its two secondary objectives are (4) to provide information on the atmosphere complementary to the reflown MCO investigations, and (5) to identify new sites with high science potential for future investigation. MRO will operate from a sun-synchronous, near-circular (255 × 320 km altitude), near-polar orbit with a mean local solar time of 3:10 PM. The Primary Science Phase, or nominal orbital mission,

[1]Applied Physics Laboratory, Laurel, Maryland, USA.
[2]Department of Earth and Planetary Sciences, Washington University, St. Louis, Missouri, USA.
[3]Institut d'Astrophysique Spatiale, Orsay, France.
[4]NASA Ames Research Center, Moffett Field, California, USA.
[5]Space Science Institute, Boulder, Colorado, USA.
[6]Applied Coherent Technology, Herndon, Virginia, USA.
[7]NASA Jet Propulsion Laboratory, Pasadena, California, USA.
[8]NASA Johnson Space Center, Houston, Texas, USA.
[9]Department of Geological Sciences, Brown University, Providence, Rhode Island, USA.
[10]Center for Planetary Sciences, Northwestern University, Evanston, Illinois, USA.
[11]NASA Goddard Space Flight Center, Greenbelt, Maryland, USA.


0148-0227/07/2006JE002682$09.00

**Table 1.** CRISM Science Strategy

| Objective | Implementation |
|---|---|
| Global characterization of crustal mineralogy and identification of targets that expose rocks diagnostic of past climate conditions and habitability. | Acquire global data with a subset of wavelengths sufficient to characterize mineralogy.<br>Target observations using results from previous Mars-orbiting instruments.<br>Identify targets using global multispectral survey data. |
| Identify and map surface mineralogy of key targets with high spatial and spectral resolutions and high SNR. | Along-track scanning used to cancel ground track motion to maximize spatial resolution (~20 m/pixel) while allowing sufficient integration times for SNR >400 at most wavelengths.<br>Coverage from ~400 nm to ~4000 nm with 545 channels provides high sensitivity to detect low abundances of key minerals such as carbonates.<br>In-flight calibration of background and responsivity provides radiometric accuracy. |
| Separate the signature of the surface from that of the atmosphere and characterize the spatial and temporal properties of the atmosphere. | Observe each targeted site over large range of emission angle (EPF) to quantify atmospheric effects.<br>Acquire repeated global EPF grids to provide averaged atmospheric correction to multispectral survey.<br>Global EPF grids provide important information on the atmosphere itself including aerosols, water vapor, and CO (putative methane?).<br>Acquire repeat measurements of standard regions at various illuminations to determine photometric functions. |

lasts for just over one Mars year beginning in November 2006. MRO's science objectives and an overview of the spacecraft and mission operations are given by *Zurek and Smrekar* [2007].

[3] MRO's instrument complement includes the Compact Reconnaissance Imaging Spectrometer for Mars (CRISM), the High Resolution Imaging Science Experiment (HiRISE) [*McEwen et al.*, 2007], the Mars Color Imager and Context Imager (MARCI and CTX) [*Malin et al.*, 2007], the Mars Climate Sounder (MCS) [*McCleese et al.*, 2007], and the Shallow Radar (SHARAD) [*Seu et al.*, 2007]. These instruments will be used in two observing modes to address MRO's five major objectives. First, the primary optical instruments (HiRISE, CRISM, and CTX) will be used to characterize the geology and mineralogy of thousands of sites at high spatial and spectral resolution. Second, CRISM, MARCI, MCS, and SHARAD will conduct regional to global surveys of the surface and atmosphere to characterize broad-scale surface and atmospheric properties, and to place the local, high-resolution observations into context.

[4] This paper provides an overview of the CRISM investigation and is divided into six major sections: (1) science background to CRISM's objectives, and how these objectives translate into an observing and analysis plan; (2) driving requirements on instrument design and how they were met; (3) mechanical and software design of the CRISM instrument; (4) overview of instrument testing, calibration, and performance; (5) instrument operations; and (6) processing of downlinked data, generation of reduced data products, and support of these data by the spectral library.

## 2. Science Objectives

### 2.1. Investigation Overview

[5] The *Mars Exploration Payload Analysis Group* (*MEPAG*) [2004] recommended 16 specific hyperspectral imaging investigations to characterize Martian geology, climate, and environments of present or past life. CRISM's three groups of science investigations (Table 1 and Figure 1) address all five of MRO's major objectives and all of MEPAG's recommendations (Table 2).

[6] CRISM will conduct its first group of investigations by making a global, 100–200 m/pixel, ~72-wavelength map. The gimbal is pointed at planet nadir, data are collected at frame rates of 15 or 30 Hz, and a commandable subset of wavelengths is saved and binned 5:1 or 10:1 cross-track. The combination of frame rates and binning yields pixel footprints of 100 or 200 m. This operating mode is referred to as the *multispectral survey*, and it will enable global characterization of surface mineralogy. The multispectral survey will also be used to search for evidence of aqueous activity that lacks morphologic expression and/or that is too small to be resolved by previous Mars-orbiting spectrometers. Thus the multispectral survey also addresses a secondary objective of MRO, to identify new sites with high science potential for future investigation, and it will be particularly important for identification of key Noachian deposits that may now exist only as mineralized spots in morphologically unremarkable eroded escarpments, crater ejecta, and talus. Much of the multispectral survey will be completed before MRO's highest downlink rates [*Zurek and Smrekar*, 2007] so that newly discovered sites can be targeted with full resolution coverage.

[7] CRISM's second group of investigations (Table 1) corresponds to two primary objectives of MRO: to search for evidence of aqueous and/or hydrothermal activity, and to map and characterize the mineralogy, geology, and stratigraphy of surface deposits. These investigations are implemented by high-resolution hyperspectral mapping of hundreds to thousands of high priority targets including candidate sedimentary deposits, volcanic regions, crustal sections exposed in steep escarpments, and sites which exhibit evidence for concentrations of aqueously formed minerals. To make such observations CRISM is operated differently, in *targeted mode*. The OSU is scanned to remove most along-track smear, and a region approximately 10 km × 10 km is imaged at full spatial resolution (15–19 m/pixel) and spectral resolution (544 channels covering

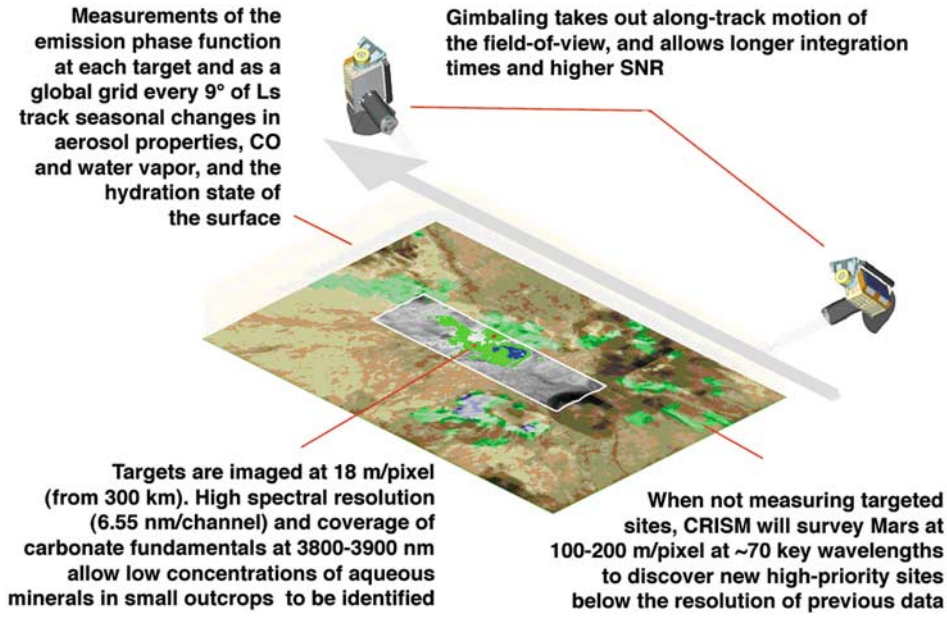


**Figure 1.** Schematic representation of CRISM's varied data acquisition strategy.

362–3920 nm). Ten additional abbreviated, spatially binned images are taken before and after the main image, providing an emission phase function (EPF) of the site for atmospheric study and correction of surface spectra for atmospheric effects.

[8] The final group of investigations addresses MRO's third primary objective, to characterize seasonal variations in atmospheric dust and ice aerosols and water content of surface materials, and one of MRO's two secondary objectives, to provide information on the atmosphere complementary to other MRO instruments. This group of investigations is implemented by measuring evenly spaced global grids of hyperspectral EPFs repeatedly throughout the Martian year, about every 10° of solar longitude.

**Table 2.** CRISM's Traceability to MEPAG's Recommendations for Hyperspectral Imaging of Mars

| MEPAG Goal and Objective | MEPAG Recommendation | CRISM Investigation |
|---|---|---|
| *Life* | | Near-global ~70-channel mapping at 100–200 m/pixel to characterize global mineralogic variations. |
| LB1: Find aqueous deposits. | Find aqueous mineralogies using hyperspectral mapping. | |
| LB2: Search for fossils. | | 15–19 m/pixel hyperspectral imaging to characterize key sites in detail. |
| LB3: Timing/duration of hydrologic activity. | Find aqueous mineral deposits and sedimentary structures. | |
| LC1: Search for complex organics in rock/soil. | Find aqueous environments possibly containing organics. | |
| LC2: History of change in carbon inventory. | Establish environments' correlations, stratigraphy. | |
| LA1: Water distribution. | Globally survey atmosphere, surface, ice caps. | EPF measurements of column abundances of water vapor, dust, ices. |
| LA4: Find energy sources. | Find "wet zones." | High-resolution measurements of ice grain size and composition in permanent caps. |
| *Climate* | | |
| CA1: Processes controlling water, dust cycles. | Observe seasonal cycles of water, dust in atmosphere, on surface. | Repeated global grid of EPFs to track seasonal variations in soil water and atmospheric gases and aerosols. |
| CA3: Long-term trends in dust, water in atmosphere. | Observe seasonal cycles of water, dust over years. | Assessment of interannual variations by coordination of observations with OMEGA and use of MGS/TES. |
| CB1: Find physical, chemical records of past. | Find aqueous mineral deposits and sedimentary structures. | Near-global ~70-channel mapping at 100–200 m/pixel to characterize global mineralogic variations. |
| CB2: Characterize past climate change. | | 15–19 m/pixel hyperspectral imaging to characterize key sites in detail. |
| *Geology* | | |
| GA2: Sedimentary history. | Identify/map crustal mineralogies and weathering products using hyperspectral imaging; associate them with structural features and stratigraphy by correlating with imaging. | |
| GA4: Igneous history. | | |
| GA5: Atmosphere-surface interactions. | | |
| GA6: Crustal composition. | | |
| GA7: Tectonic history. | | |

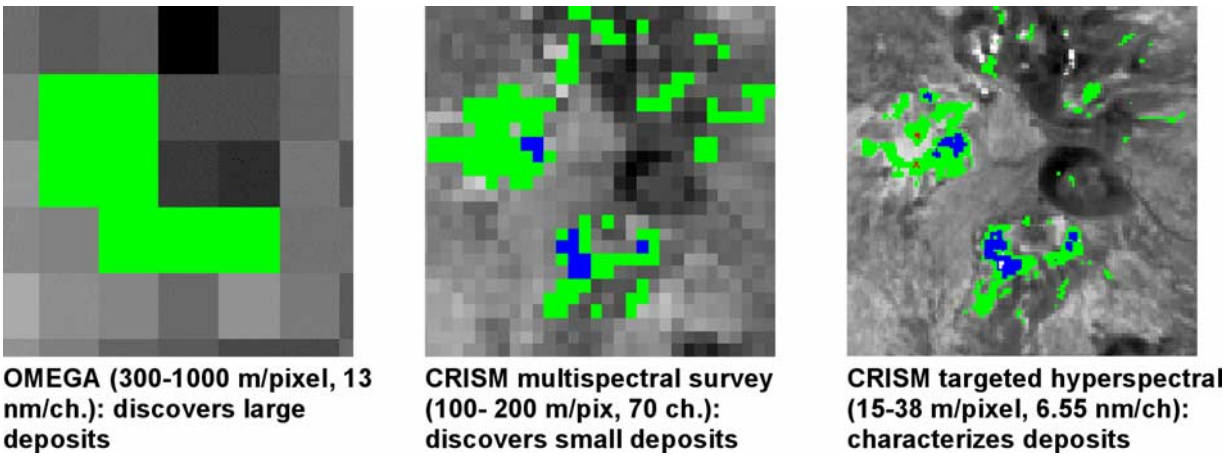


**Figure 2.** Simulation of OMEGA, CRISM multispectral mapping, and CRISM targeted observations of hydrothermal deposits. AVIRIS data covering hot spring deposits at Mauna Kea were resampled to the appropriate resolutions and classified using a spectral angle mapper. Colors represent different phyllosilicate phases.

Typically the spacing is 27° in longitude and 11° in latitude, but ten times per Martian year a denser grid is taken with 9° longitude spacing. EPF measurements allow accurate determination of column abundances of water vapor, CO, dust and ice aerosols, and their seasonal variations [*Clancy et al.*, 2000, 2003]. At the same time, the grid's repetitive coverage will track seasonal variations in water content of surface material. To take each point on a global EPF grid, CRISM is operated in targeted mode but all of the data are spatially binned to conserve data volume.

#### 2.1.1. Step 1: Discover the Deposits

[9] At visible-infrared (VISIR) wavelengths, there is evidence at all spatial scales for Martian deposits of secondary minerals formed in oxidative or aqueous environments. At the hundreds-of-kilometers scale, telescopic and Phobos 2/Imaging Spectrometer for Mars (ISM) observations show evidence for deposits of bulk, crystalline ferric minerals, particularly in Eastern Syrtis Major [*Bell et al.*, 1990; *Mustard et al.*, 1993] and Lunae Planum [*Murchie et al.*, 2000]. Data from the Observatoire pour la Mineralogie, l'Eau, les Glaces et l'Activité (OMEGA) on the Mars Express spacecraft show that a large arc around the north polar layered deposits is enriched in gypsum [*Langevin et al.*, 2005a]. Aqueous mineral deposits having scales of kilometers to tens of kilometers are more widely distributed across the planet [*Bibring et al.*, 2005] and include hydrated sulfate concentrations in Hesperian-aged layered deposits that unconformably overlie older terrains (Valles Marineris, Aram Chaos, Terra Meridiani) [*Gendrin et al.*, 2005; *Arvidson et al.*, 2006], and phyllosilicates in Noachian-aged basement (Mawrth Valles, Nili Fossae) [*Poulet et al.*, 2005a]. Even at the scale of boulders, multispectral imaging from Mars Pathfinder and MER reveals concentrations or encrustations of ferric minerals [*McSween et al.*, 1999; *Bell et al.*, 2004a, 2004b].

[10] Thermal IR mapping by TES and THEMIS has revealed evidence for more coarse-grained aqueous minerals, specifically gray hematite [*Christensen et al.*, 2000], typically in the same regions where OMEGA sees evidence for hydrated sulfates [*Bibring et al.*, 2005]. While TES data have yielded some evidence for sulfates and sheet silicates, such identifications are close to the detection limits of the instruments [e.g., *Bandfield*, 2002]. The difference in phases whose signatures appear at thermal and VIS-IR wavelengths is consistent with Martian aqueous minerals being predominantly very fine-grained (<50 microns), so that diagnostic mineral bands are spectrally subdued at thermal wavelengths but still strong in the VIS-IR [*Wagner and Schade*, 1996; *Kirkland et al.*, 2000].

[11] Regional to global VISIR coverage is therefore crucial for identifying targets for high-resolution observations by MRO and CRISM. OMEGA is paving the way by surveying the Martian surface at 0.4–5.1 $\mu$m, 0.3–4.8 km/pixel. As of MRO launch, global mapping was 90% complete. For the purpose of targeting CRISM observations, OMEGA data have been parameterized and mapped [*Pelkey et al.*, 2007] and used together with nighttime THEMIS image mosaics, Mars Orbiter Camera (MOC) images, and TES thermal inertia maps to locate areas of high scientific potential for CRISM targeted mode observations. These sites are recorded in an internal target list that serves as an input to uplink planning software. Instrument operations are discussed in greater detail in section 6.

[12] Even though OMEGA near-global coverage is crucial for CRISM target identification, OMEGA data lack the spatial resolution in most parts of the planet to find deposits that outcrop at <1-km scales. To find such deposits and to provide global coverage in key wavelengths at a higher resolution than acquired by OMEGA, CRISM utilizes its multispectral survey. The instrument points at nadir and operates at a 15 or 30 Hz frame rate, and data are binned spatially by 5x or 10x. Data from only 72 selected rows of the VNIR and IR detectors (selected wavelengths) are returned. The resulting data are 100 or 200 m/pixel. Simulations using Airborne Visible Infrared Imaging Spectrometer (AVIRIS) data [*Green et al.*, 1998] resampled to resolutions of OMEGA, CRISM in multispectral survey mode, and CRISM at full resolution verify that the several-fold increase in spatial resolution over OMEGA allows smaller targets of interest to be resolved (Figure 2). Targets

identified in CRISM's multispectral survey will be entered into the target list and followed up with high-resolution observations, as with targets identified from OMEGA data.

#### 2.1.2. Step 2: Obtain Measurements With High SNR and Spectral and Spatial Resolutions

[13] CRISM's along-track scanning produces imaging data with high spectral and spatial sampling and high SNR. The wavelength range 362–3920 nm is sampled at 6.55 nm/channel, enabling identification of a broad range of silicates, oxides, and salts. CRISM's highest spatial resolution (15–19 m/pixel) enables measurement of small deposits comparable to those observed with AVIRIS (Figure 2) and is essentially the same spatial resolution as THEMIS visible data. Signal-to-noise ratio (SNR) exceeds 400 at key wavelengths, and is ~100 at >3000 nm. More detail on spatial and spectral resolution and SNR is provided in section 5.

[14] The spatial resolution and wavelength range of CRISM's hyperspectral measurements will resolve deposits that have been investigated at lander scale by MER, and detect the variety of primary and secondary minerals that were found in those deposits. For example, the light-toned crater wall measured by MER-Opportunity at Endurance crater can be resolved in CRISM's full resolution targeted mode (Figure 3a). The primary igneous minerals olivine and pyroxene are distinguished by the positions and shapes of their broad absorptions near 1000 and 2000 nm (Figure 3b). Among alteration products, ferric minerals are distinguished mainly by the positions and relative strengths of absorptions from 400–1000 nm (Figure 3c) and phyllosilicates by the positions, shapes, and relative strengths of OH absorptions near 1400 and 2200–2300 nm (Figure 3d). The Ca and Mg sulfates detected or inferred from OMEGA and MER measurements are evidenced by absorptions at 1400–2500 nm due to their bound water (Figure 3e). Although there has not been a definitive detection of either carbonates or nitrates, these mineral classes are of great interest because they may contain trapped ancient atmosphere; CRISM's coverage of the 3000–3900 nm wavelength range enables detection of their strong fundamental absorptions (Figure 3f).

#### 2.1.3. Step 3: Separate Surface Mineralogy From Atmospheric Effects

[15] Atmospheric aerosols contribute a large fraction of Martian VISIR radiance measured from space, especially at wavelengths less than 2500 nm. Scattering and absorption by aerosols and attenuation by atmospheric gases alter apparent depths and positions of mineralogic absorptions [*Erard et al.*, 1994]. Analysis of the EPF at each target will provide well-constrained aerosol optical depths, plus accurate determinations of CO and $H_2O$ vapor column abundances. These measurements allow post-processing corrections for atmospheric effects in order to isolate spectral properties of the surface.

### 2.2. Science Background

#### 2.2.1. Aqueous Environments

##### 2.2.1.1. Background

[16] The environments most likely to preserve a Martian fossil record include pedogenic layers, paleolakes or paleoseas, and springs [*Farmer and Des Marais*, 1999]. In these environments, biologic materials are rapidly entombed by clays or chemical precipitates. Alteration products formed in these environments include iron oxides and oxyhydroxides, zeolites, carbonates, sulfates, hydrated silica, and phyllosilicates [e.g., *Allen and Conca*, 1991; *Banfield et al.*, 1991; *Robert and Goffé*, 1993; *Bishop et al.*, 2004]. The hydrated sulfates and iron oxides discovered by MER-Opportunity at Meridiani Planum are examples of these on Mars [*Squyres et al.*, 2004a, 2004b]. The mineralogy of ferric iron, phyllosilicates, zeolites, carbonates, and sulfates, in particular, are indicators of Eh-pH and salinity at the time of their deposition [*Surdam*, 1977; *Hay and Sheppard*, 1977; *Sherman et al.*, 1982; *Kodama et al.*, 1988; *Gíslason and Eugster*, 1989; *Gíslason and Arnórsson*, 1990; *Berkgaut et al.*, 1994; *McLennan et al.*, 2005]. One promising environment for a fossil record is hot springs: these environments combine an energy source with rapid entombment and are thought to have been crucial to early life on Earth [*Bock and Good*, 1996; *Farmer*, 1998].

[17] Evidence for the occurrence of aqueous mineralogies comes from both remotely sensed and in situ measurements. OMEGA data show evidence for two distinct types of aqueous deposits [*Bibring et al.*, 2005]. The first type, characterized by sulfates including gypsum and kieserite, is correlated spatially with layered deposits of Hesperian age that unconformably overly older terrains [*Gendrin et al.*, 2005]. The second type, rich in several different phases of phyllosilicates, is more limited areally and correlates spatially with exposures of Noachian material [*Poulet et al.*, 2005a]. The different ages and chemistries of the two types of deposits are suggestive of different genetic environments.

[18] The main evidence from landed measurements comes from MER. At the sites of both MER-Opportunity and MER-Spirit, there are non-basaltic materials enriched in oxidized iron and salts, especially sulfates [*Squyres et al.*, 2004a, 2004b]. Significantly, only the MER-Opportunity deposits exhibit a distinctive spectral signature in orbital data from TES and OMEGA. MER-Spirit's discovery of comparable deposits, despite lack of orbital spectral evidence for their existence, strongly suggests that CRISM's one to two orders of magnitude improvement in spatial resolution over TES and OMEGA will reveal additional sites of interest besides those summarized above.

##### 2.2.1.2. Key Questions and Measurement Objectives

[19] OMEGA's global mapping has identified several regions that contain outcrops of aqueous deposits. CRISM provides increased capabilities to map spatial structure of these materials due to its higher spatial resolution, and to resolve mineralogy due to its 2x increase in spectral resolution (6.55 nm spectral sampling. versus 13 nm for OMEGA at comparable wavelengths). Thus CRISM's measurement strategy focuses on finding small-scale deposits, characterizing their mineralogic variations, and improving the accuracy of mineralogic determinations.

[20] 1. What are the mineralogies and distributions of pedogenic layers? Diagenetic minerals in soils include ferric oxides and oxyhydroxides, carbonates, and sulfates. Besides entombing and preserving fossils on Earth [*Horodyski and Knauth*, 1994], pedogenic layers in the stratigraphic column provide important information on past weathering. Large parts of the Martian surface with a dark red visible color have been interpreted as duricrust [*Presley and Arvidson*, 1988; *Christensen and Moore*, 1992]. Such cemented

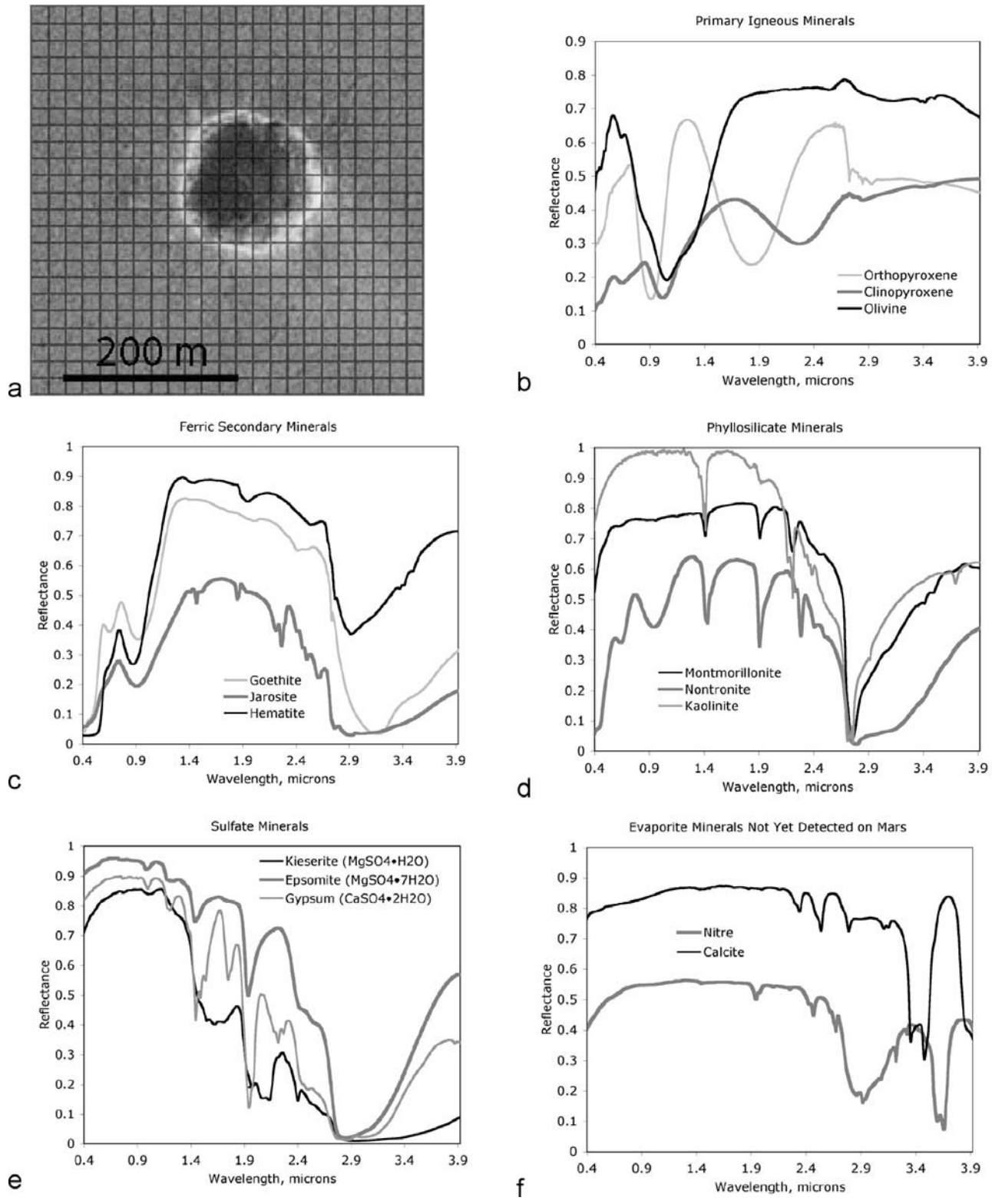


**Figure 3.** CRISM will provide hyperspectral maps at very high spatial and spectral resolutions to characterize the geology of key sites. (a) Endurance Crater at MER/Opportunity site as seen by MOC (squares, 18 m CRISM pixels). (b–e) Laboratory spectra of minerals identified by MER or OMEGA, at CRISM's wavelength range. (f) Laboratory spectra of salts whose discovery on Mars would have significant paleoclimatologic implications.

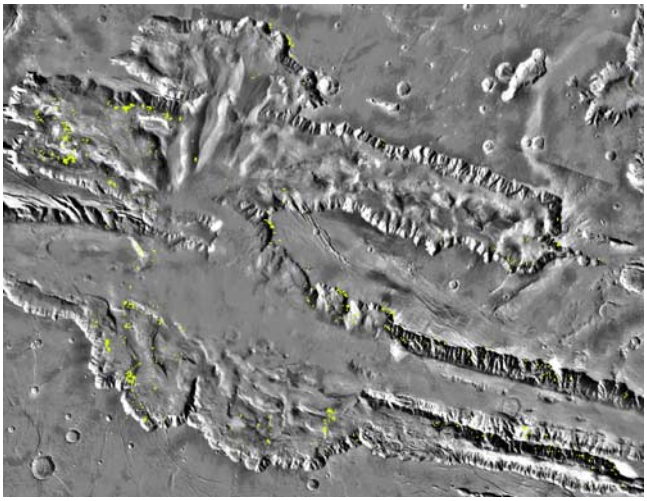

**Figure 4.** Spectral evidence from OMEGA for hydrated mineralogies in the layered deposits of Valles Marineris. Map of depth of 1900-nm absorption due to $H_2O$ in minerals, interpreted as polyhydrated sulfates, overlain on a map-projected digital image mosaic. Green areas have 1900-nm absorption depths greater than 2.5%.

materials may contain sulfates salts [e.g., *Bishop et al.*, 2002a]. In the VISIR duricrust areas show evidence for enrichment in hydrated and ferric minerals [*Murchie et al.*, 1993, 2000]. In its 200-m/pixel multispectral survey mode, CRISM will characterize such deposits over broad expanses; on escarpments the high spatial resolution targeted observations will image exposed stratigraphic sections to search for vertical zonation in suspected pedogenic layers.

[21] 2. What deposits formed in standing water? Lacustrine and marine environments are favorable for fossil preservation, especially if rich in precipitates [*Forsythe*, 1990; *Farmer and Des Marais*, 1999]. Hundreds of highland craters [*Forsythe and Blackwelder*, 1998; *Cabrol and Grin*, 1999] and Valles Marineris [*Nedell et al.*, 1987] have interior deposits that may be lacustrine. In saline environments, chemical precipitates are often layered in the sequence carbonates to sulfates to halides [*Eugster and Hardie*, 1978]. Where clastic sediments dominate, these may exhibit diagenetic mineralization that can fossilize biologic materials [*Berner*, 1968]. Investigations by MER-Spirit in the Columbia Hills show evidence for diagenetic mineralization and enhanced concentrations of salts in the interior deposits of Gusev crater [*Klingelhöfer et al.*, 2005; *Wang et al.*, 2005]. VISIR studies of Valles Marineris using ISM data show possible evidence for ferric mineralization in western Candor Chasma [*Murchie et al.*, 2000; *Mustard and Murchie*, 2001] and OMEGA data show evidence for interbedded sulfate-rich layers scattered throughout the Valles Marineris layered deposits [*Gendrin et al.*, 2005] (Figure 4). Layered deposits in Terra Meridiani show several lines of mineralogic evidence for standing water in the distant past: hematite mineralization in TES data [*Christensen et al.*, 2000], in situ detection of high levels of sulfates and hematite by MER-Opportunity, and orbital detection by OMEGA of sulfate deposits in eroded exposures of the layered materials [*Arvidson et al.*, 2006]. CRISM will take high-resolution measurements of these and comparable deposits to determine their mineralogic variations on small horizontal and vertical scales. For example, MER-Opportunity has found elemental, mineralogical, and textural (climbing ripples) evidence that indicate the sulfate rich deposits beneath Meridiani Planum formed in a playa-dune environment characterized by acid-sulfate evaporates that were reworked by wind during a period of rising groundwater table [*Grotzinger et al.*, 2005]. Given that MER-Opportunity has examined the top of a ~300 m section of etched terrain materials that are exposed over hundreds of thousands of square kilometers, there will be numerous targets to be covered by CRISM to characterize regional variations in mineralogy and implications for paleoclimatic conditions and habitability.

[22] 3. Are ancient hot spring or cold spring deposits preserved? Approaching the higher-temperature cores of hot springs from their cooler, distal margins, phyllosilicates change from smectite-chlorite to talc-kaolinite, and ferric oxides become dominated by hematite [e.g., *Kristmannsdóttir*, 1982; *Mehegan et al.*, 1982; *Shau and Peacor*, 1992]. There are many environments in which Martian hot springs may have formed, especially around volcanoes. Ancient (>3 Ga) hot spring deposits may however be cryptic, existing only as mineralized spots in morphologically unremarkable eroded escarpments, crater ejecta, and talus [*Farmer and Des Marais*, 1999]. One of the more provocative findings from OMEGA are concentrations of phyllosilicates in exposures of Noachian crust near Nili Fossae, surrounding the volcanic shield Syrtis Major, and in deeply excavated Noachian materials in Mawrth Valles [*Poulet et al.*, 2005a]. The mineralogy of these deposits (Fe-rich smectite clays) indicate a low temperature alteration perhaps in the shallow subsurface. In situ investigation of etched terrains in Terra Meridiani by MER-Opportunity revealed evidence for preferential cementation in fracture zones [*Arvidson et al.*, 2003], suggesting that cold springs once existed in this region of Mars. Using higher spatial resolution, CRISM will seek to resolve the compositional structure and identify the specific minerals present in these and other possible spring deposits.

#### 2.2.1.3. Measurement and Analysis Approach

[23] Initial targets will focus on layered deposits (possible sediments), highland volcanic regions including possible hydrothermal deposits, and duricrusts. Those are being selected on the basis of evidence from MOC, TES, THEMIS, and OMEGA. Between targeted observations, the multispectral survey will identify new sites with spectral signatures of aqueous mineralogy that are below the spatial resolution of OMEGA and those sites will be followed up with targeted observations.

[24] Data analysis is facilitated using two CRISM-specific analysis tools, the Rapid Environmental Assessment and Compositional Tool (REACT) and the CRISM Analysis Tool (CAT). REACT is developed by Applied Coherent Technologies, Inc., and provides standard capabilities to visualize data cubes, to apply calibrations from raw units of DN to units of radiance or I/F (these transformations are discussed in section 5.3.2), or to map-project the data. CAT is based on ENVI, a commercial software package from ITT Visual Information Solutions, but is customized to CRISM. It can perform analyses such as

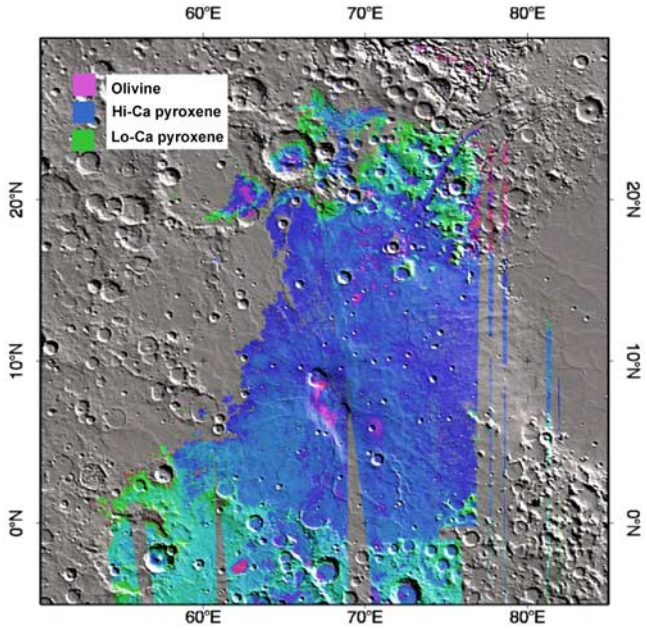


**Figure 5.** Spectral unit map of Syrtis Major from OMEGA data, based on parameterized depths of mineralogic absorptions at 1, 1.15, and 2 microns.

spectral angle mapping (applied to simulated CRISM data in Figure 2), mixture modeling [*Mustard and Pieters*, 1987; *Sunshine et al.*, 1990] and principal components analysis [e.g., *Murchie et al.*, 2000].

[25] As a tool to support analysis of CRISM data, a spectral library has been provided to the community through the PDS (see section 7). This library contains spectra and ancillary information for Mars analog materials that have been measured over CRISM's wavelength range under desiccating conditions like those at the surface of Mars. Previous publicly released spectral libraries do not cover the full spectral range of CRISM, and typically their contents were not measured under desiccating conditions like those on Mars. The ambient terrestrial environment induces significant spectral differences from what would occur in the Martian environment due to enhanced $H_2O$ absorptions in hygroscopic minerals.

### 2.2.2. Crustal and Surface Composition and Processes

#### 2.2.2.1. Background

[26] The igneous mineralogic composition of the Martian crust has been examined through remotely sensed data, meteorites, and in situ observations by landers and rovers [*McSween et al.*, 1999, 2003; *Squyres et al.*, 2004a, 2004b]. Meteorites exhibit the greatest petrologic diversity but are, with the exception of one sample, <1.3 Ga in age and young compared to typical Martian surface ages.

[27] Remotely sensed and landed measurements imply that the crust is dominantly basaltic, composed mostly of feldspar and pyroxene [*Mustard et al.*, 1997; *Bandfield et al.*, 2000]. The upper crust is composed of hundreds of interbedded layers accumulated to kilometers in thickness [*McEwen et al.*, 1999; *Malin and Edgett*, 2001] that range in age from Noachian through Amazonian [*Scott and Tanaka*, 1986; *Greeley and Guest*, 1987]. Several classes of volcanic edifices occur, ranging from shields to highland paterae composed of interbedded friable and resistant units [*Greeley and Spudis*, 1981]. Resistant units are interpreted as flows, whereas friable units are considered phreatomagmatic or pyroclastic [*Crown and Greeley*, 1993].

[28] Two major divisions in crustal mineralogic composition are recognized on the basis of their thermal infrared spectral signatures in TES data [*Bandfield et al.*, 2000]. Type I material, predominantly in the equatorial highlands, is interpreted as basaltic in agreement with earlier interpretations based on VISIR data acquired telescopically [*Singer et al.*, 1979] and by Phobos-2/ISM [*Mustard et al.*, 1993, 1997]. Type II, found predominantly in the northern lowland plains, has been interpreted to be andesite or basaltic andesite [*Bandfield et al.*, 2000], altered basalt with a significant component of aqueous weathering materials [*Wyatt and McSween*, 2002; *Morris et al.*, 2003], oxidized basalt [*Minitti et al.*, 2002], or silica-coated basalt [*Kraft et al.*, 2003]. Some outcrops of ancient crust exhibit high concentrations of olivine [*Hoefen et al.*, 2003] and low-calcium pyroxene (LCP) in thermal emission data [*Hamilton et al.*, 2003]. Granitoid compositions, suggesting evolved magmas, are observed in northwest Syrtis Major [*Bandfield et al.*, 2004].

[29] OMEGA's higher spatial resolution than TES provides additional information on the geologic context of olivine and LCP enriched units. Additionally, OMEGA's complementary wavelength coverage provides additional constraints on the composition of type I and type II materials. Olivine occurs throughout the stratigraphic column, from outcrops in Noachian terrains to high concentrations in Hesperian volcanics (Figure 5) and on crater floors [*Bibring et al.*, 2005; *Mustard et al.*, 2005]. Thus olivine-normative magma compositions have occurred throughout Martian history. High concentrations of LCP are found only in Noachian-aged cratered terrains (e.g., Figure 5). In type I materials, high-calcium pyroxene (HCP) at a 10–15% abundance is found in combination with LCP, consistent with earlier results from ISM [*Mustard et al.*, 1997].

[30] OMEGA has sampled broad areas of type II materials in the northern lowlands. The spectral properties of these regions are best characterized as low albedo with a decreasing reflectance as a function of wavelength from 900–2600 nm [*Mustard et al.*, 2005]. A weak 2 $\mu$m absorption band is observed in some areas north of Arabia but there is no well defined or apparent 1 $\mu$m band. There is no evidence for enhanced vibrational absorptions due to $H_2O$ and/or OH- which could indicate the presence of alteration products and phyllosilicates. However, the absence of these features is consistent with many nanophase and poorly crystalline alteration products observed in altered volcanic material [*Morris et al.*, 2001; *Bishop et al.*, 2002b]. The lack of evidence of phyllosilicates or hydrated minerals indicates that either the altered basalt contains primarily nanophase and poorly crystalline phases, or that andesite/basaltic andesite is present. The lack of distinct mafic mineral bands indicates that minerals or volcanic glasses expected in andesite are not expressed in these data. However, thin alteration rinds or coatings as observed at the Mars Pathfinder [*McSween et al.*, 1999; *Murchie et al.*, 2004] and Gusev landing sites [*Morris et al.*, 2004] could mask such signatures.

#### 2.2.2.2. Key Questions and Measurement Objectives

[31] CRISM's investigation of Martian crustal lithology focuses on questions addressed through improved spatial resolution, primarily vertical crustal structure, and the sensitivity of VISIR wavelengths to altered phases.

[32] 1. How did Martian volcanism evolve with time, as evidenced by superposed units of different age? Martian meteorites provide evidence of extensive igneous differentiation [*McSween et al.*, 2003]. The lithologies recognized (dunites, ortho- and clinopyroxenites, basalts to basaltic andesites) have diagnostic differences in mafic mineral absorptions at VIS-IR wavelengths that correspond with some (but not all) of the spectral types identified to date. Techniques for remotely determining pyroxene composition using spectral analyses are well known [*Adams*, 1974; *Cloutis and Gaffey*, 1991; *Sunshine et al.*, 1990], but their accuracies in complicated mixed lithologies common on Mars are limited to a few tens of percent [*Mustard et al.*, 1997]. OMEGA, TES, and THEMIS data covering regions with spectral heterogeneity [*Mustard et al.*, 2005; *Hamilton and Christensen*, 2005] together provide the first insights into the temporal evolution of Martian magma source regions, described above. CRISM will build on these findings.

[33] 2. What parts of plains units are volcanic, and what parts are interbedded sedimentary materials? Interbedded sediments or soil horizons would be recognizable if they contain mineralogies associated with evaporitic or diagenetic environments. TES and THEMIS data have been interpreted to show evidence for horizons enriched in gray hematite [*Christensen et al.*, 2000] and OMEGA data show evidence for interbedded sulfate-rich materials in the Valles Marineris layered deposits and in the unconformable deposits in Meridiani and western Arabia [*Bibring et al.*, 2005; *Arvidson et al.*, 2006].

[34] 3. What are the mineralogic differences between type I and type II lithologies? OMEGA data do not provide supporting evidence for several proposed compositions of type II material, because to date they cannot distinguish between palagonite [*Bishop et al.*, 2002a; *Morris et al.*, 2003] and poorly crystalline coatings [e.g., *Kraft et al.*, 2003; *Bishop et al.*, 2003]. CRISM is well suited to further constrain the mineralogy of type II materials because its VNIR wavelengths (400–1000 nm) are well-suited to detection of the nanophase ferric materials characteristic of altered volcanic material, and its higher spatial resolution allows searching for small regions in which a coating has been scoured away to expose substrate.

[35] 4. Do friable and resistant volcanic layers have different compositions, or do their physical differences arise from other mechanisms such as mode of emplacement or incorporation of water? Different compositions could be reflected by changes in pyroxene mineralogy or the presence of amphiboles. Incorporation of water during emplacement would be evidenced by glassy or palagonitic materials [*Farrand and Singer*, 1991]. CRISM wavelengths and resolutions have the ability to address these issues.

#### 2.2.2.3. Measurement and Analysis Approach

[36] Initial targets will include sections exposed in escarpments, transects across volcanic edifices, and systematic sampling of plains units. Targets are initially being preselected on the basis of previous studies, especially areas where nighttime THEMIS images indicate increased blockiness or bedrock exposures, or where OMEGA data indicate exposures of diverse lithologies.

[37] The multispectral survey will identify new targets and put all targets into a regional context. Science results will include the composition, stratigraphy, and spatial extent of major crustal units, interpretation of the history of volcanic provinces, and the relative roles of igneous and sedimentary materials in crustal structure.

### 2.2.3. Aerosols, Volatiles, and Volatile Cycling

#### 2.2.3.1. Background: Water and Dust in the Atmosphere

[38] The current Martian climate exhibits annual cycles involving variations in the abundance of $H_2O$ vapor, CO, water ice aerosols, and dust [*Zurek et al.*, 1992; *Kahn et al.*, 1992; *Clancy*, 1999; *Smith*, 2004]. The perihelion southern summer season exhibits the greatest dust loading and most variability. Global dust storms in this season occur only infrequently but regional dust storms have shown surprising repeatability across different Martian years [*Clancy et al.*, 2000; *Smith et al.*, 2001; *Cantor et al.*, 2002; *Smith*, 2004]. In contrast, the aphelion northern summer season is characterized by lower temperatures, a tropical water-ice cloud belt, minimal dust loading, and water vapor saturation at low altitudes [*Clancy et al.*, 1996, 2000; *Smith et al.*, 2001, *Smith*, 2004]. Atmospheric $H_2O$ vapor varies in abundance seasonally, with greatest abundance ($\sim$100 pr-$\mu$m) in summertime at northern high latitudes [*Jakosky and Farmer*, 1982; *Smith*, 2002, 2004]. CO abundance should also vary at high winter latitudes and provide a tracer for atmospheric circulation [*Joshi et al.*, 2003]. Systematic observations of aerosols and gases are needed to assess interannual variability and to understand its causes.

[39] Dust and water ice can contribute as much as 20–30% of Martian radiance measured from space over much of the CRISM spectral range. Thus accurate recovery of surface spectral properties also requires measurement and characterization of scattering and attenuation throughout the entire atmospheric column. Aerosol effects are summarized in Figure 6, where total radiance from the surface, atmospheric gases, and aerosols is ratioed to the radiance from the surface alone. Figures 6a–6c show the anticipated effects on VISIR reflectance spectra of three major types of aerosols identified in TES data: dust (Figure 6a), "seasonal" circumpolar water ice with a 1–2 $\mu$m particle diameter (Figure 6b), and coarser 2–4-$\mu$m diameter water ice in the equatorial aphelion cloud belt (Figure 6c). These spectra were modeled at CRISM's spectral resolution on the basis of analysis of TES EPFs [*Clancy et al.*, 2003] and incorporating a discrete ordinates multiple-scattering radiative transfer algorithm, detailed $CO/CO_2/H_2O$ gas transmissions, and composition- and size-dependent aerosol optical properties. Aerosol contributions are modestly wavelength-dependent over wavelengths <2500 nm but distinct near 3000 nm due to the strong absorption of water ice. The displayed dust model manifests a low spectral contrast across the CRISM range, whereas both types of water ice have a strong 3000 nm absorption feature. Aphelion water ice is distinguished from smaller-grained seasonal water ice by stronger 1500-nm and 2000-nm absorptions as well as by its continuum.

[40] Scattering and attenuation by aerosols also partially masks atmospheric gas absorption features; effective path

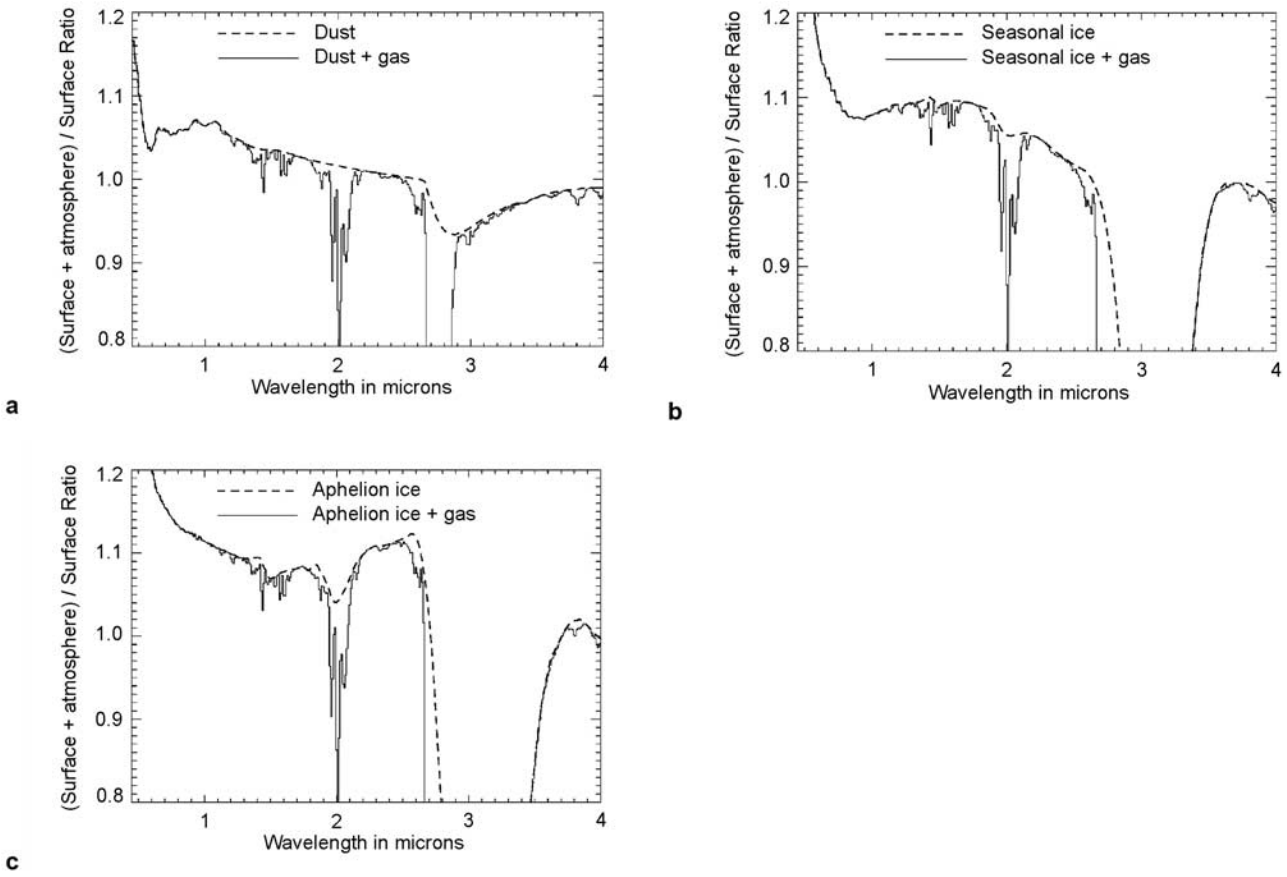


**Figure 6.** Model spectra of Mars radiance with a standard atmosphere and different aerosol types, ratioed to the spectrum of the surface alone, with the aerosols consisting of (a) dust, (b) seasonal water ice, and (c) aphelion water ice.

lengths are reduced from geometric path lengths by >20% even under modest aerosol loading conditions. Gas absorption features therefore also need to be analyzed in concert with aerosols for accurate determinations of column abundances.

**2.2.3.2. Background: Volatiles at the Surface**

[41] From ground-based observations of the 3000-nm $H_2O$ absorption, molecular water is known to be present in the regolith [*Moroz*, 1964; *Houck et al.*, 1973; *Pimental et al.*, 1974]. Pre-OMEGA orbital measurements of the 3000-nm absorption by Mariner 9 IRS and Phobos 2 ISM showed that $H_2O$ is enriched in some formations and spectral units [*Erard et al.*, 1991; *Murchie et al.*, 1993, 2000; *Calvin*, 1997]. OMEGA data show two types of concentrations of $H_2O$ evidenced by an increased 1900-nm and/or 3000-nm band. In the first type, increased 1900 nm absorptions are associated with specific geologic formations, and additional vibrational absorptions attribute these to sulfate and phyllosilicate phases [*Bibring et al.*, 2005; *Gendrin et al.*, 2005; *Arvidson et al.*, 2006; *Langevin et al.*, 2005a; *Poulet et al.*, 2005a]. In the second type, an increased 1900 nm absorption is observed without accompanying mineral bands, or increases in the 3000 nm absorption are observed without an observed 1900 nm band. This occurs most prominently in the circumpolar region, in soils from which the seasonal polar cap recently ablated [*Schmitt et al.*, 2005; *Poulet et al.*, 2005b]. Strength of the 1900-nm band increases poleward from midlatitudes, but there are no accompanying bands to suggest sulfates or phyllosilicates [*Milliken et al.*, 2006]. This trend suggests that the water exists in adsorbed form that is retained in the H-enriched regions at high-latitudes [*Boynton et al.*, 2002; *Feldman et al.*, 2002]. Adsorbed water is expected to vary in abundance seasonally [*Jakosky and Haberle*, 1992] but it is not yet clear from OMEGA data where and when the abundance of water in the regolith varies [*Jouglet et al.*, 2006].

[42] $H_2O$ and $CO_2$ also exist as seasonal and perennial polar ices. The perennial caps were long thought to consist mostly of $H_2O$ in the north and $CO_2$ in the south [*Kieffer et al.*, 2000]. TES discovered discrete layers in the southern cap with a temperature warmer than $CO_2$ ice, and it was thus inferred that there is a significant component of water ice [*Titus et al.*, 2003]. OMEGA reflectance spectra show that the southern cap's $CO_2$ ice is widespread but surficial, and MOC high-resolution images constrain it to be a veneer no more than ~10 m in thickness [*Byrne and Ingersoll*, 2003], covering a massive cap in which $H_2O$ ice is intermixed with $CO_2$ ice and dust [*Bibring et al.*, 2005]. The seasonal caps have an upper layer of $CO_2$ ice in both fine- and coarse-grained forms [*Titus et al.*, 2001]. At least in the northern seasonal cap there is also a significant $H_2O$ ice component: fine-grained $H_2O$ ice remains after ablation of the $CO_2$ ice, and then itself ablates leaving coarse-grained

$H_2O$ ice [*Bibring et al.*, 2005; *Langevin et al.*, 2005b; *Poulet et al.*, 2005b].

[43] No other large reservoirs of $CO_2$ other than the polar deposits and atmosphere have been recognized. In particular, OMEGA has not detected any kilometer-scale outcrops of carbonate minerals despite its sensitivity to percent-level abundances. The lack of large carbonate reservoirs provides no evidence for retention of an earlier, thicker $CO_2$-rich atmosphere [*Bibring et al.*, 2005].

**2.2.3.3. Key Aerosols and Volatiles Questions and Measurement Approach**

[44] OMEGA is providing a baseline on kilometer-scale spatial variations in contents of $H_2O$, OH, and carbonate in surface materials, but its spectral resolution of 13–20 nm/channel cannot distinguish OH-minerals with similar absorption bands. CRISM's surface volatile measurement strategy emphasizes temporal variations, small-scale deposits, and accurate mineralogic determinations.

[45] 1. How does the water content of the regolith change seasonally? To monitor interannual variations in seasonal cycling of $H_2O$ in the regolith, CRISM's repeated global grids of EPFs will be used to observe midlatitude regions repeatedly in a fashion that allows separation of seasonal variations in atmospheric water and water adsorbed on surface materials.

[46] 2. What are the characteristics of dust and water ice aerosols and how do they vary with location and season? Building on TES and THEMIS observations of the Martian atmosphere through several years, CRISM will provide a new perspective allowing frequent, detailed characterizations of dust and water ice aerosol properties.

[47] 3. Where and how have volatiles been sequestered in the Martian surface? CRISM will target the sulfate and phyllosilicate deposits identified by OMEGA to determine their mineralogic compositions and mineralogic variations at small spatial scales. In addition, CRISM's multispectral survey will detect small-scale clay, carbonate, or $H_2O$-enriched deposits below the spatial resolution of OMEGA and expand the range of environments.

[48] 4. What is the composition of the layers in the polar caps? Representative sections of each perennial polar cap will be measured to search for interlayer variations in mineralogic composition.

[49] 5. What are the processes that govern the seasonal deposition and removal of water and $CO_2$ frosts and how have they changed with time? Growth and ablation of the seasonal polar caps will be monitored in representative locations to determine the sequence of deposition and removal of $CO_2$ and coarse- and fine-grained $H_2O$ ices. Systematic measurement of the seasonal caps will add significantly to the legacy of past missions.

**2.2.3.4. Measurement and Analysis Approach**

[50] Key properties to be measured include column abundances of $CO_2$, CO, and $H_2O$ gases, and the optical depth and scattering behaviors of dust and water ice aerosols. CRISM will determine these quantities using measurements of local EPFs. An EPF sequence views the same spot on the surface at a range of different emission angles. The resulting known variation in path length and scattering geometry, while surface illumination remains essentially fixed, allows the retrieval of well-constrained total column abundances of aerosols and gases. Both dust and ice aerosols lead to increased VISIR atmospheric radiance at higher emission angles, corresponding to longer path lengths. However, they are distinguished by both the wavelength dependence of the increased radiance (Figure 6) and by the distinct scattering behavior as a function of phase angle [e.g., *Clancy et al.*, 2003]. This latter effect leads to an asymmetric emission angle dependence of atmospheric radiance, particularly for ice aerosols.

[51] A complete EPF sequence with 11 emission angles covering the range from $-70°$ to $+70°$ will be obtained for each targeted surface observation to determine associated atmospheric properties and to support the separation of surface and atmospheric signatures. In addition, a global grid of EPF sequences will be taken every $\sim 10°$ of $L_s$. This repeated global survey will determine spatial and seasonal variability in CO, $H_2O$, and aerosol column abundances as well as constrain the physical properties of dust and ice aerosols. In addition, such retrievals will form the basis of atmospheric "correction" re-processing for the multispectral survey (initial processing will be done with climatological data based on observations from MGS TES [*Smith*, 2004]).

[52] Analysis of CRISM EPFs will be based upon the approach taken for TES [*Clancy et al.*, 2003] and Viking IRTM [*Clancy and Lee*, 1991]. Both TES's and CRISM's EPF measurements are typically obtained at fixed-incidence and moderate phase angles ($\sim 40°$–$100°$), in which case surface photometric variations are minimized with respect to atmospheric effects. The key radiative transfer tool will be the discrete ordinates, multiple-scattering algorithm DISORT [*Stamnes et al.*, 1988]. The models shown in Figures 6a–6c were produced using a version of the DISORT-based code of *Clancy et al.* [2003]. Initially, we will use the dust and water ice scattering phase functions from upward-looking Pathfinder observations [*Tomasko et al.*, 1999] and TES EPF global analyses [*Clancy et al.*, 2003], with extensions to additional CRISM wavelengths using the indices of refraction published by *Wolff and Clancy* [2003]. These will be augmented with analysis of a small number of EPFs being obtained by OMEGA. Each CRISM EPF observation will be analyzed to retrieve aerosol/gas optical depths and aerosol type. These atmospheric properties are well-constrained by the simultaneous retrieval from the range of EPF angles.

[53] These analyses will result in atmospherically corrected surface spectra for targeted observations as well as for the global grids of EPF measurements. CRISM's atmospheric measurements will also complement observations by other MRO instruments. Its coverage of VISIR wavelengths characterizes solar absorption and particle size properties of the aerosols while limb observations by MARCI [*Malin et al.*, 2007] provide insight into the vertical distribution of aerosols. Together, these two data sets can be used to constrain thermal and microphysical forcing of Mars global circulation and water vapor saturation conditions [e.g., *Clancy et al.*, 1995, 1996; *Rodin et al.*, 1999]. Furthermore, CRISM's $H_2O$, CO, and aerosol abundance determinations, together with MARCI ozone and MCS [*McCleese et al.*, 2007] water vapor and water-ice cloud observations, will enable detailed study of Martian atmospheric photochemistry.

**Table 3a.** CRISM Driving Requirements and As-Built Performance

| Requirement | Required Value | Achieved | Comment/Justification |
|---|---|---|---|
| | *Primary Requirements, Driven by the MRO Project* | | |
| Spectral range | 400–3600 nm to 4050 goal | 362 – 3920 nm | coverage to >3600 nm allows greater sensitivity to carbonate |
| Spectral sampling | better than 10 nm | 6.55 nm | measured dispersion |
| Swath width | >7.5 km at 300 km (>1.45° FOV) | 9.4 to 11.9 km | central 1.8° of 2.12° FOV unvignetted |
| Spatial sampling | <37 m/pixel @ 300 km (resolve 75-m spot) | 15.7 to 19.7 m/pixel resolves 38-m spot | from 255 km × 320 km orbit |
| Lifetime | 1.8 years; goal 5.4 | >4 years | estimate based on heat load, MTTF of 12000 hrs per cryocooler |
| | *Selected Secondary Requirements, Internal to CRISM* | | |
| IR detector temperature | <120 K | ~100 K attainable | operational temperature commandable |
| Spectrometer housing temperature | <198 K | <194 K | 184 K to 194 K depending on orbit |
| SNR | >400 at 2300 nm | 425 at 2300 nm, >100 at 400 and 3600 nm, for average material at 30° phase angle | estimated from ground calibration data |
| System MTF | 0.2 at 9.25 cycles/mm | 0.73 VNIR; 0.4 IR | analysis uses as built measurements of PSF, pointing jitter, estimate of orbital image smear |
| Pointing | ±60° along track | ±60° along track | ground and flight testing |
| Scan jitter | 48 $\mu$rad from aimpoint | 25 $\mu$rad from aimpoint | ground and flight testing |
| Spectral full width half-max | better than 20 nm; goal <9 nm | 7.9–10.1 nm VNIR 9–19 nm IR | limited by diffraction, FOV effects, aberrations, and alignment |
| Spectral smile (VNIR) | <1.2 pixels | 1.3 pixels | from monochromatic sources |
| Keystone (VNIR) | <±0.4 pixels | <±0.42 pxls | measured point source dispersion |
| Spectral smile (IR) | <1.2 pixels | 1.3 pixels | from monochromatic sources |
| Keystone (IR) | <±0.4 pixels | <±0.42 pxls | measured point source dispersion |
| Spectral profile, VNIR | <2%, 3 pixels from peak | $\ll$1% | measured response to monochromator |
| Spectral profile, IR | <2%, 3 pixels from peak | typically <2% | measured response to monochromator |
| Out of field stray light | <2% | <1% | quartz halogen lamp out of field |

[54] For targeted and multispectral observations, targeting, data analysis, and deliverable products will parallel those for aqueous deposits and crustal materials. Absorptions due to ices and other volatile-containing phases are recognizable even through overlapping gas bands by virtue of the latter's emission-angle dependence in EPFs. To monitor the seasonal variation in $H_2O$ content of surface materials, surface radiances measured in the global grid will be analyzed using the time series of latitudinally and longitudinally binned global maps.

## 3. Instrument Requirements and System Design Impacts

### 3.1. Requirements and Performance

[55] CRISM's high-level requirements are tabulated in Table 3a, and compared with as-built performance. The most basic requirements (spatial and spectral sampling and wavelength range) are level 1 requirements of the MRO project; others are internal requirements to CRISM. Both are derived from a requirements study of post-OMEGA imaging spectroscopy of Mars [*Kirkland et al.*, 1999] and from the Science Definition Team requirements for imaging spectroscopy on MRO [*Zurek et al.*, 2001].

### 3.2. System Overview

[56] CRISM's system design is summarized as a block diagram in Figure 7, and the as-flown hardware is shown in Figure 8. The optical design is summarized in Figure 9. Key system parameters are given in Table 3b. A 10 cm diameter Ritchey-Critien telescope feeds a pair of Offner convex-grating spectrometers. Along-track-scanning to remove image motion smear is accomplished by mounting the entire optical assembly on a one-axis gimbal attached to the nadir deck of the MRO spacecraft. One spectrometer, denoted as visible-near infrared (VNIR), uses array of silicon photodiodes. The other, denoted as infrared (IR), uses an array of HgCdTe diodes. Both detectors, which were developed by Rockwell Science Center (RSC), have a 640 × 480 (spatial × spectral) format of 27-$\mu$m square pixels bonded to a TMC 6604A Read Out Integrated Circuit (ROIC). *Silverglate and Fort* [2004] describe in detail the system design trades that led to this configuration. The most significant results of those trades include the following:

[57] 1. A fully gimbaled optical system with a compact Ritchey-Chretien design rather than a scan mirror feeding a fixed telescope provides a more compact overall configuration and lower scattered light.

[58] 2. The field of view is oversized relative to the minimum required 1.45°, in order to provide margin in covering discrete targets.

[59] 3. Spatial sampling is a factor of 2 better than the minimum requirement, so that the implicit spatial resolution requirements are met once diffraction effects are taken into account.

[60] 4. An in-flight calibration system equipped with a shutter and an integrating sphere is used to characterize subtle instrument artifacts including variation in thermal background with spectrometer cavity temperature, variation of responsivity or dark current with detector temperature,

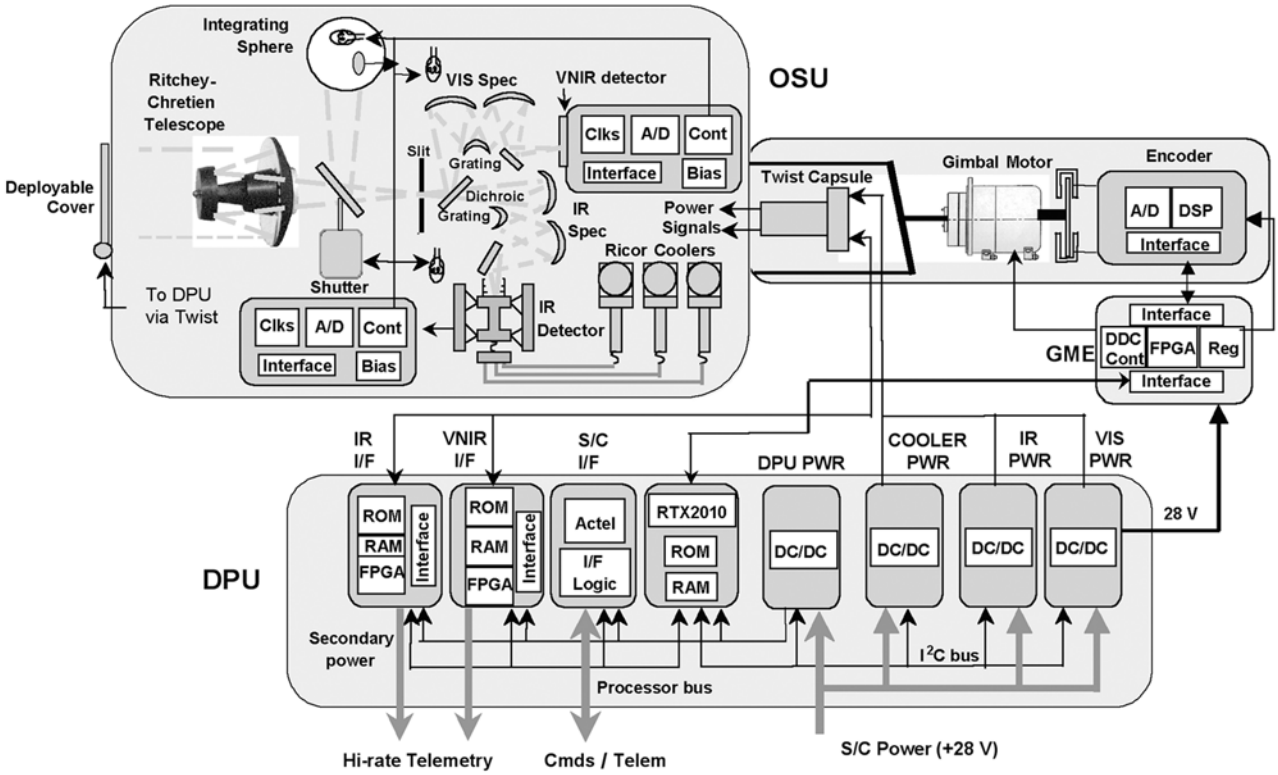


**Figure 7.** Block diagram illustrating CRISM's key components and functions. OSU, Optical Sensor Unit; DPU, Data Processing Unit; GME, Gimbal Motor Electronics; S/C, spacecraft; DC/DC, direct current to direct current voltage converter; ROM, read-only memory; RAM, random-access memory; Cont, controller; DDC Cont, Data Device Corporation controller; Reg, regulator; A/D, analog to digital signal converter; Clks, clocks; FPGA, field programmable gate arrange; I/F, interface; PWR, power; RTX2010, Harris RTX2010 microprocessor; I2C, inter-integrated circuit; and DSP, digital signal processor.

drift in bias levels or response uniformity, or accumulation of nm-thick ice on the extremely cold (∼100°K) IR detector from condensation of water desorbed by the spacecraft body.

[61] 5. HgCdTe IR detector material with a 4050 nm long-wavelength cutoff was used in preference to InSb to provide lower sensitivity to instrument thermal background.

[62] 6. Silicon photodiodes provide better sensitivity than CCDs in the VNIR wavelength range, and eliminate image smear during frame transfer. The use of identical formats and read out systems for VNIR and IR also simplified electrical design and allowed for direct matching of optical magnification.

[63] 7. Active cooling of the IR array was chosen over passive cooling. MRO is required to point off-nadir frequently by up to 30°, and the desirable orbit has a mid-day local solar time. Passive cooling would be problematic under these conditions, with MRO's limitations on CRISM's mass, volume, and development schedule. A novel design, using three RICOR K508 Integral Sterling cryocoolers connected in parallel with cryogenic diode heat pipes, avoided the unacceptably large mass and the schedule impact of procuring a long-lived pulse-tube cooler.

## 4. System Design

### 4.1. Mechanical Overview

[64] CRISM consists of three boxes; the Optical Sensor Unit (OSU) which includes the optics, gimbal, focal planes, cryocoolers, radiators, and focal plane electronics; the Gimbal Motor Electronics (GME), which commands and powers the gimbal motor and encoder and analyzes data from the encoder in a feedback loop; and the Data Processing Unit (DPU), which accepts and processes commands from the spacecraft and accepts and processes data from the OSU and communicates it to the spacecraft. Figure 8 shows the fabricated boxes.

### 4.2. Optics

[65] CRISM's optomechanical structure is all-aluminum to minimize change in focus with temperature. Overall optical design is shown in Figure 9. Components are mounted to an optical bench (Figures 10 and 17) which also serves as a Mars-facing radiator that cools the optics to minimize IR background, and as a mount for the shutter and internal integrating sphere.

[66] Light is focused by a 100-mm aperture, 441-mm focal length Ritchey-Chretien on-axis telescope onto a slit. Both the primary and secondary mirrors (telescope M1 and M2, or first and second mirrors) are coated aluminum, and are baffled to block out-of-field paths to the slit. The secondary is mounted by a spider and obscures 29% of the aperture. The telescope is protected by a composite baffle with flexure mounts to the optical bench (Figure 10). The interior of the baffle is vaned to attenuate off-axis scattered light. The end of the baffle is covered by a hinged,

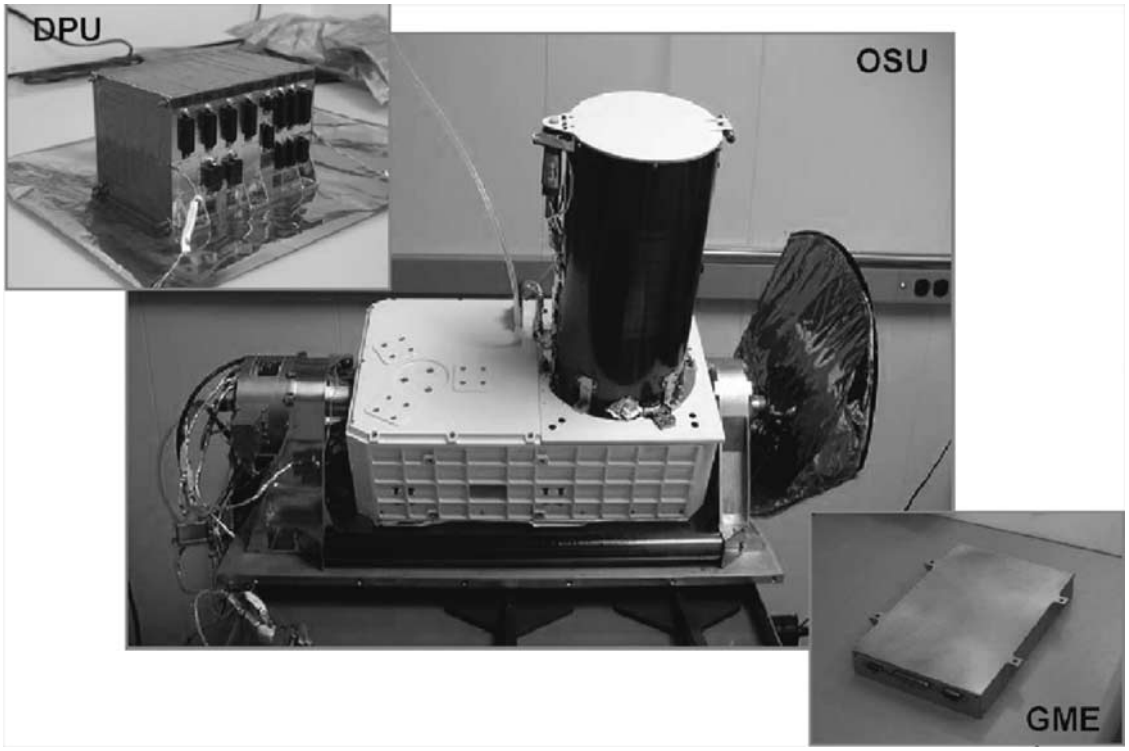


**Figure 8.** Photographs of the Optical Sensor Unit (OSU), Data Processing Unit (DPU), and Gimbal Motor Electronics (GME).

solid-composite, one-time deployable cover. Deployment occurs using a high-output paraffin actuator with redundant heaters. Either heater is sufficient to release the cover, and each can be commanded independently. The cover has a contact sensor that indicates whether the cover is closed or not. The cover will be opened following MRO's aerobraking into its science orbit.

[67] The slit (Figure 11) is 27 $\mu$m wide and 16.3 mm long and is mounted in an assembly for fastening to the optical bench. The slit is mounted on a 76-mm radius cylindrical surface whose axis is perpendicular to the slit, to improve focus. The slit is constructed of nickel and its telescope facing side is gold plated, both to resist effects of heating and to dissipate incident solar energy in the event of a direct view of the sun. Irregularities in slit width cause along-slit variations in system response at the percent level; the maximum irregularity is a burr that attenuates incoming light by only 10%.

[68] Following the slit is the spectrometer optics. A wedged, ZnSe dichroic beamsplitter reflects the VNIR

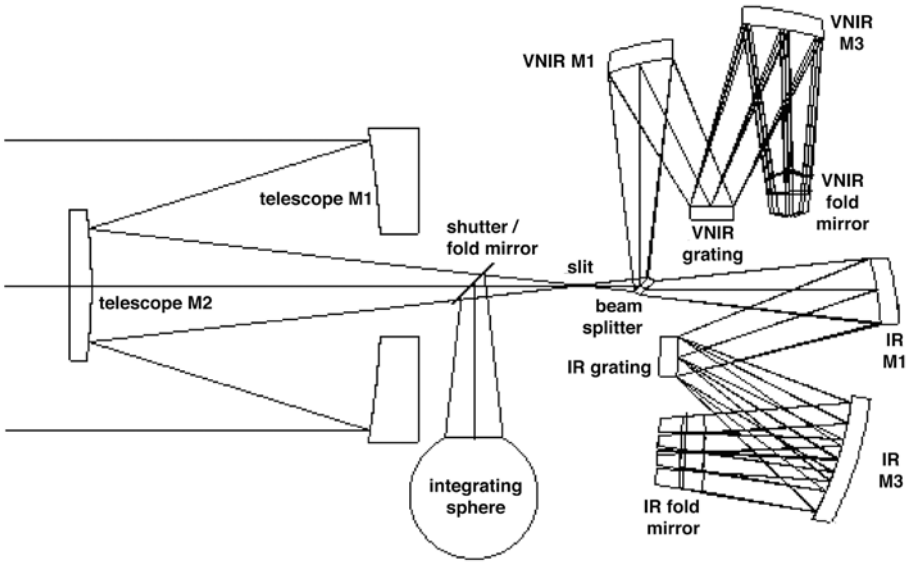


**Figure 9.** Optical design of CRISM's telescope and spectrometers.

**Table 3b.** CRISM System Parameters

| Parameter | Value |
|---|---|
| Mass | 32.92 kg |
| Power (during normal operations) | 44.4–47.3W |
| Power (during standby with subsystems off) | 16.1W |
| Aperture | 100 mm |
| Focal length | 441 mm |
| Detector pixel pitch | 27 $\mu$m |
| Field of view | 2.12° |
| Instantaneous FOV (pixel angular size) | 61.5 $\mu$rad |
| Spectral range | VNIR: 362–1053 nm<br>IR: 1002–3920 nm |
| Spectral sampling | 6.55 nm/channel |

while transmitting the IR (Figure 12), each to its own modified Offner spectrometer and focal plane assembly. The wedge directs internal reflections in the transmitted IR light out of its nominal path, so that the reflections can be blocked by the order-sorting filter on the detector. The two modified Offner spectrometers disperse the light and focus it onto their respective focal planes. In the VNIR spectrometer the first and third reflective optical elements (VNIR M1 and M3, for mirror 1 and mirror 3) are prolate ellipsoids and the grating (VNIR M2) is mounted on a spherical surface. In the IR spectrometer IR M1 and IR M2 are spherical and IR M3 is a generalized asphere approximating an oblate ellipsoid. Both spectrometers account for the curved slit, thereby creating a flat, well-corrected slit image at the detector. Each spectrometer also has a fold mirror after M3 that directs the light out of plane to focus on the focal plane assembly (FPA) mounted on the side of the spectrometer for thermal control. Nominally each spectrometer has unity magnification, but due to manufacturing tolerances the angular sizes of the two FOVs differ by 1.2%.

[69] The diffraction gratings (Figure 13) are an aluminized polymer manufactured by JPL using an electron beam process [*Wilson et al.*, 2003]. Each is dual-zone, with each zone blazed to maximize efficiency in either the longer- or shorter-wavelength parts of the VNIR or IR spectral range. The areas of each zone are sized to balance SNR in their two wavelength ranges. CRISM uses first-order diffracted light; higher orders from the gratings are blocked by fixed-mounted filters on the detectors.

**Figure 11.** Photograph of the flight slit assembly.

### 4.3. Detectors

#### 4.3.1. VNIR

[70] The VNIR focal plane consists of a silicon photodiode detector array indium bump-bonded to a TCM 6604A multiplexer. The focal plane consists of 640 column × 480 rows with 27-$\mu$m elements, and the long axis oriented in the along-slit direction. There are four quadrants each 160 columns in width. Readout occurs one row (wavelength) at a time, and each quadrant's output is sent to a separate analog-to-digital converter that digitizes it to 14 bits. Component-level calibration (section 5.1) showed that read noise is approximately 180 e-, and gain is 80 e- per 14-bit DN. Full well is approximately 780,000 e-, and response is quasi-linear up to about 93% of full well. A bias voltage applied to the detector assures that, even with the minimum signal and dark current, 14-bit DNs are significantly greater than zero.

[71] The columns in the detector have three types of exposure to light. By design, approximately 10 columns at each edge are physically masked by a metallic coating to serve as a reference for dark current. Inside the masked columns, another ~10 columns on each side are not masked but neither are they exposed to direct illumination through the slit. These columns measure glare from the grating and other components internal to the spectrometer. The central 600 columns are intended to image the slit. Due to manufacturing and alignment tolerances, the actual dimensions of

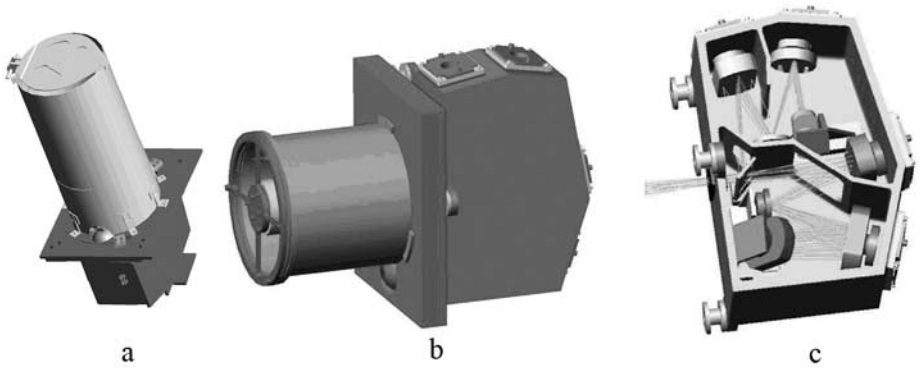


**Figure 10.** CAD renderings of the optomechanical assembly showing (a) the full assembly with baffle and cover in a non-deployed position, (b) the assembly with the baffle removed, and (c) a cutaway of the coplanar dual spectrometer with representative rays.

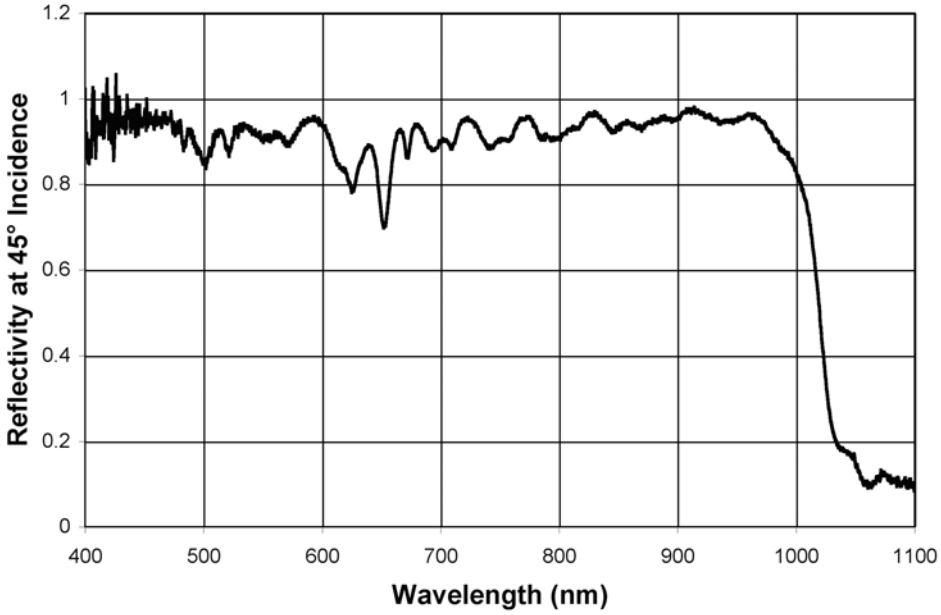


**Figure 12.** Reflectivity of the beamsplitter in the VNIR wavelength range.

the three illumination regions of the detector are slightly different than the design (section 5.2).

[72] A fixed mounted filter on the detector blocks higher orders from the grating (Figure 14a). By design the boundary is near 650 nm. The filter, composed of two distinct filter glasses, stands approximately 0.2 mm off the detector surface. A mask at the filter boundary, consisting of a black stripe 216 microns wide, was microlithographically placed on the filter surface. The mask blocks scatter off the joint between the two glasses and, although it does attenuate the scene at adjacent wavelengths, because it is out of focus the transmission is not reduced to zero. Spectral information is not lost, and the shadowing attenuation can be calibrated out (section 5.2). By design, only 107 out of the 480 available rows have useful amounts of dispersed light. 363 of the remaining 373 rows are physically masked; the 10 rows adjacent to the 107 useful rows are unmasked to provide margin for detector alignment in the instrument.

[73] The detector is mounted in a focal plane assembly (Figures 15a and 15b). The FPA holds the detector at the proper angle to the spectrometer housing to locate it at the optical focal plane, and thermally isolates it from the colder spectrometer housing while allowing translation and rotation relative to the side of the spectrometer housing to minimize spectral smile and keystone distortions. The detector's temperature is thermostatically controlled to $-60^{\circ}$C in order to maintain quantum efficiency at wavelengths >900 nm.

[74] The VNIR detector has a dedicated electronics board in the base of the gimbal that provides the required clock signals and bias voltages, and separately digitizes the video data from each quadrant of the focal plane. The digitized data are transmitted through a twist capsule to the DPU. The focal plane electronics control redundant focal plane lamps in the spectrometer housing that can illuminate the focal plane, permitting a non-uniformity calibration. They also

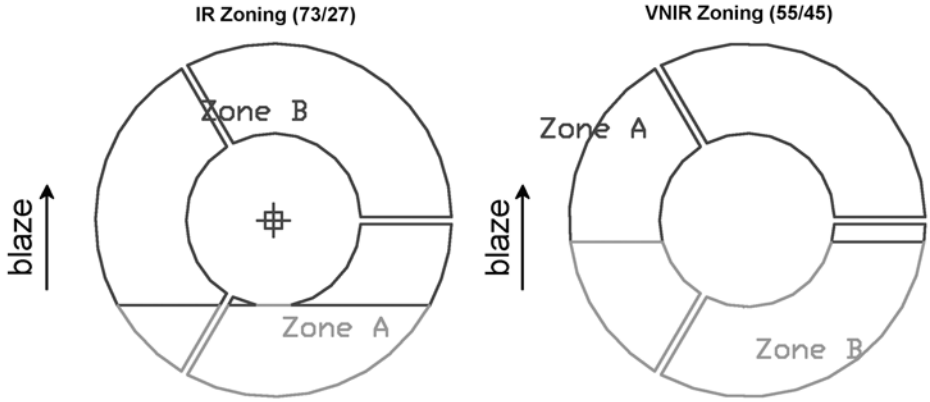


**Figure 13.** View from infinity of zoning of the IR and VNIR gratings, projected through the instrument aperture and showing obscuration of the gratings by the telescope secondary mirror and spider. On each grating, zone A is optimized for shorter wavelengths, and zone B is optimized for longer wavelengths.

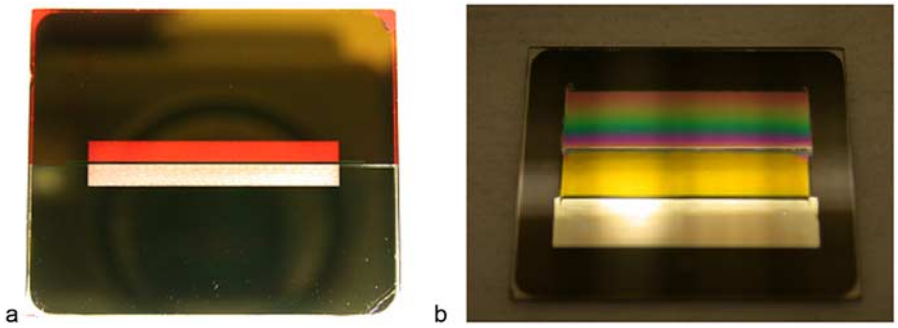


**Figure 14.** Views of the VNIR and IR fixed mounted filters from the optics, showing (a) VNIR order sorting filter zones 1 and 2 (bottom to top) and (b) IR filter zones 1, 2, and 3 (bottom to top). In each case, shorter wavelengths are to the bottom.

control one of the two redundant lamps in the internal integrating sphere. The board monitors its own temperature and current, shutter motor current, and temperatures of the detector, spectrometer housing, telescope, and baffle. Both the VNIR or IR board can control one of two redundant sets of windings in the shutter motor; in a contingency situation in which the shutter resists movement, both windings can be used together.

#### 4.3.2. IR FP

[75] The infrared (IR) focal plane consists of a HgCdTe detector array indium bump-bonded to a TCM 6604A multiplexer, the same as used in the VNIR array. The HgCdTe detector was grown on a CdTe substrate by molecular beam epitaxy (MBE) by the Rockwell Science Company (RSC). Dimensionally, electrically, and optically, the IR detector resembles the VNIR detector except for differences summarized below. Read noise is slightly lower at 140 e-, but gain and full well are similar.

[76] The fixed-mounted filter is a three-zone interference filter designed to block not only higher orders from the grating, but also thermal background to which the detector responds at wavelengths <4250 nm (Figure 14b). Zones 1 and 2 are band-pass filters that transmit wavelengths of 1000–1810 nm and 1580–2840 nm, respectively (Figure 16). Zone 3, covering longer wavelengths, is a linearly variable filter with an 80-nm band pass and a linear variation in center wavelength scaled to match the dispersion of the IR spectrometer. All three zones overlap in order to eliminate

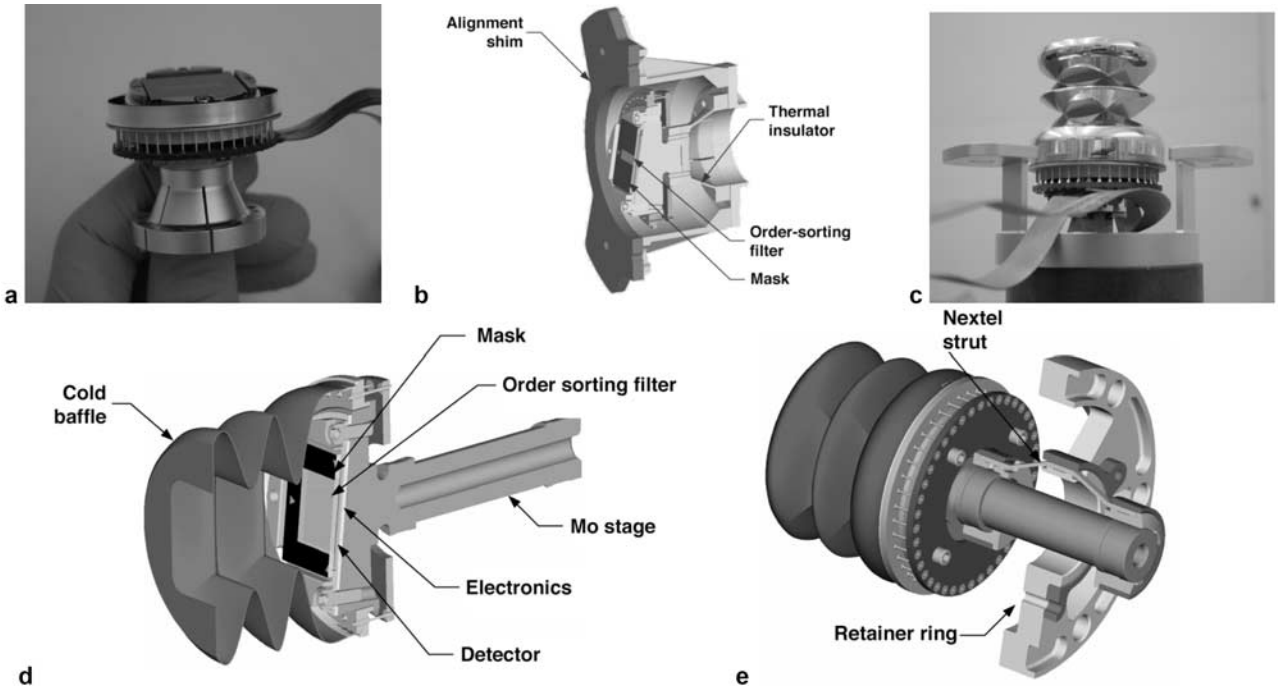


**Figure 15.** (a) VNIR focal plane assembly showing mounted detector, thermal isolation mount, and connecting cables. (b) CAD rendering of cutaway view of VNIR FPA. (c) IR focal plane assembly, including the gold-coated cold shield and connecting cables. The cold shield is bellowed to baffle scattered light. (d) CAD rendering of cutaway view of the cryogenic portion of the IR FPA. (e) CAD rendering of the cryogenic portion of the IR FPA mounted in its retaining ring showing the thermal isolation struts.

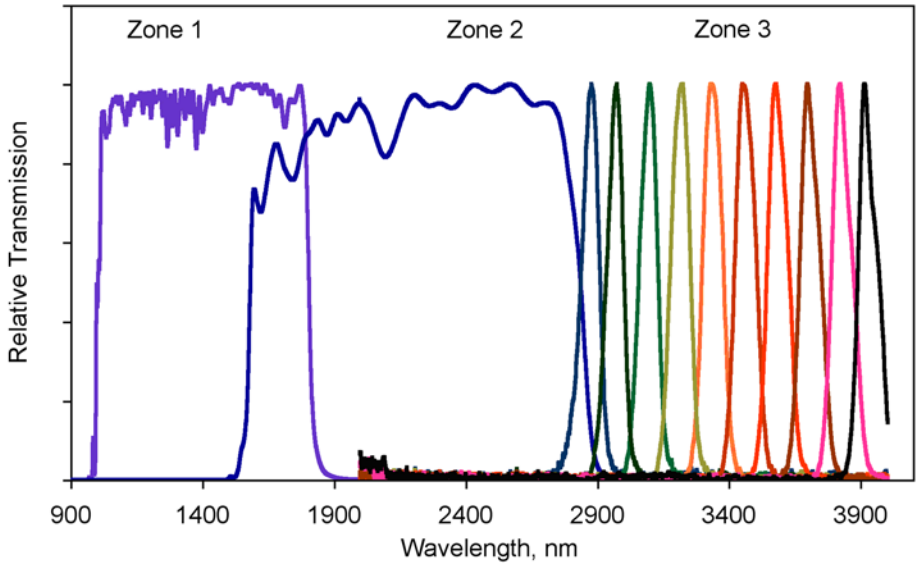


**Figure 16.** Relative transmission of IR order sorting filters, including zones 1 and 2 and representative locations in zone 3. Figure produced with permission of Rockwell Science Company.

"leaks" of thermal background to the detector. At the zone 1/zone 2 boundary there is no gap in transmission, but there is a narrow gap in transmission about 40 nm wide at the zone 2/zone 3 boundary from about 2720–2760 nm. In addition, thermal background in excess of that within zones 2 and 3 is admitted at the boundary of the two zones, but this can be calibrated out.

[77] The IR focal plane assembly (Figures 15c–15e) is more complicated than the VNIR assembly, due to the three times larger temperature contrast that has to be maintained between the detector and spectrometer housing. The cryogenic part of the FPA is mounted to a molybdenum core, and includes the detector held at proper angle to the spectrometer housing to locate it at the optical focal plane, as well as associated electronics. A cold shield, blackened on the interior, limits the view of the spectrometer housing to that necessary to admit the cone of light from the spectrometer optics, in order to reduce thermal background. Baffling attenuates off-axis scatter of thermal background through the baffle's rectangular aperture. A low-emissivity gold coating on the cold shield's outer surface limits radiative coupling of the baffle to the spectrometer housing. The detector's temperature is maintained at either of two setpoints, 104° or 108°K, using an active cryogenic system described in section 4.5, in order to minimize dark current. The cryogenic portion of the FPA is thermally isolated from its retaining ring by rigid, low thermal conductivity nextel struts. The struts resist creep in the orientation of the cryogenic core in the face of repeated thermal cyclings. The design of the IR assembly is discussed in more detail by *Lees et al.* [2005].

[78] Like the VNIR board, the IR focal plane electronics board is located in the base of the gimbal and provides clock signals and bias voltages, and separately digitizes the video data from each quadrant of the focal plane. It transmits digitized data through the twist capsule to the DPU, controls redundant focal plane lamps, controls one of the two redundant integrated sphere lamps, and monitors its own temperature and current, shutter motor current, and temperatures of the detector, spectrometer housing, telescope, and cryogenic coolers. In addition the IR board monitors the temperature of the integrating sphere and current of the IR-controlled sphere lamp.

### 4.4. Calibration Subsystem

[79] CRISM has several internal calibration capabilities that allow monitoring bias, dark current and thermal background, detector nonuniformity, and responsivity of the parts of the system behind the slit.

[80] Two parts of the calibration subsystem, a shutter and an integrating sphere, are built into the optical bench (Figure 17). The shutter is an aperture-filling vane with a polished aluminum rear surface, attached to a 33-position

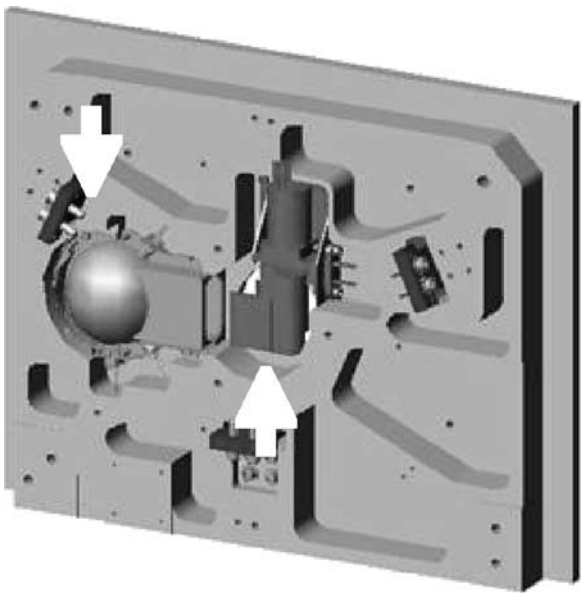

**Figure 17.** CAD rendering of the optical bench from the spectrometer side, showing the shutter mechanism (center) and internal integrating sphere (left).

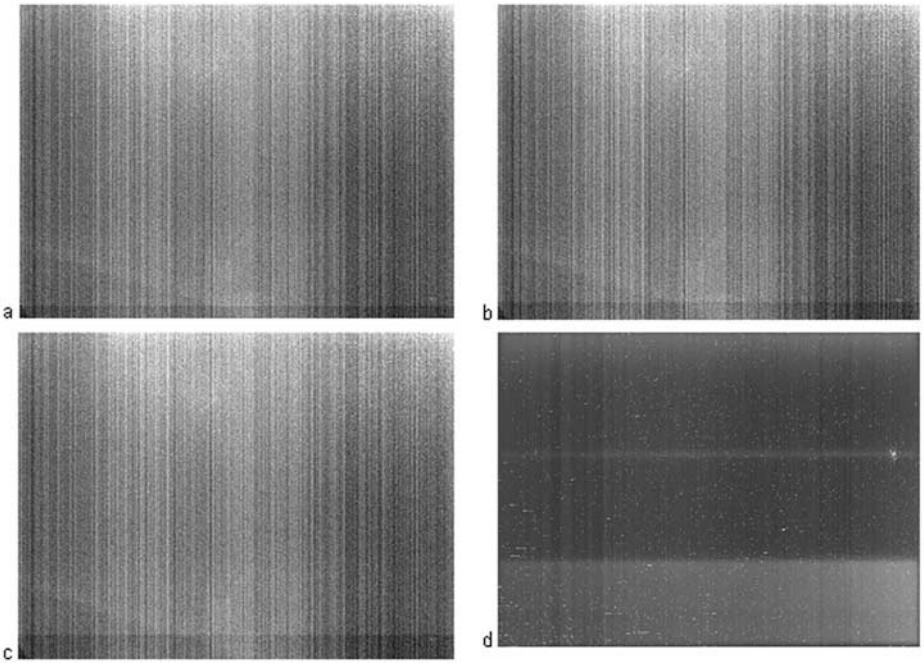


**Figure 18.** Highly stretched full-frame (a–c) VNIR and (d) IR frames taken with the shutter closed, showing bias, dark current, and background. (a–c) VNIR images with frame rate 1 Hz and integration time 81, 96, and 115 ms, respectively. Row 0 is the top row. Note the column dependence of the bias, and a step function in the overall level, near the bottom. The location of the step function moves with exposure time. The scale of the stretch is approximately 100 14-bit DNs. (d) Note the scattering of relatively bright pixels with elevated dark current, and the greater thermal background in zone 1 (at bottom). The thermal background scales with exposure time and temperature of the spectrometer housing, but for targeted observations during the primary science phase the maximum values are expected to be about 500 14-bit DNs.

stepper motor with 3° steps. In its closed position (position 32), the shutter enables measurement of bias, dark current, and (for the IR detector) thermal background. At position 17 it provides a view of the internal integrating sphere. The nominal open position is 0 but as discussed in section 5.3.2, the open position was redefined in software to position 3 to eliminate an unanticipated reflection from the base of the shutter. The stepper motor has no absolute position knowledge, and instead moves between reference positions of open (position 3), sphere (position 17), and closed (position 32) by counting steps. A photodiode can view a fiducial LED when the shutter is located at positions 0, 17, or 32. Normally the fiducial is left unpowered to eliminate stray light, but it will be powered periodically in flight to check that the shutter has not skipped positions. Figures 18a–18c show VNIR frames acquired during ground testing with the shutter closed, and Figure 18d shows a shutter-closed IR frame.

[81] The internal integrating sphere provides a smooth, near-flat field of dispersed light as viewed though either spectrometer (Figures 19a and 19d). It samples all of the optics except the telescope, and is intended as the primary in-flight reference for radiometric calibration. The sphere is lined with sandblasted aluminum and has a slightly vignetted rectangular aperture. Illumination is provided by either of two small incandescent lamps, one controlled by the VNIR focal plane electronics that is located in the plane of the slit off to one side, and one that is controlled by the IR focal plane electronics that is located orthogonal to the slit off to one side. The VNIR-controlled bulb is the primary bulb for in-flight calibration because its orientation generates less cross-slit brightness gradient, minimizing effects of small irreproducibilities in the shutter's position viewing the sphere (section 5.3.2). The lamps' peak current is 115 mA, and current level can be commanded either directly (open loop) or under closed loop control (section 4.8.2). For closed loop control, a Si photodiode inside the sphere measures the brightness of the lamp and adjusts current to match a brightness goal. There is one photodiode per lamp, controlled by the same focal plane electronics that control the lamp. A single closed-loop setpoint (~90% of maximum) is used in flight, and each lamp runs at ~2000°K at its setpoint. Convolved with the efficiency of the optics and detectors, signal in DN/second as viewed at the detector peaks near 2200 nm. Under closed loop control, either of the sphere lamps' brightness stabilizes in 3–4 seconds after it is turned on, and for the same sphere temperature, it repeatedly achieves the same current to within one part in a thousand. The brightness of the sphere exhibits slight, systematic variation dependent on its temperature, as described in section 5.3.3.

[82] Each detector can also be illuminated by either of two redundant focal plane lamps, which are mounted in the spectrometer housing and bathe the detector with undispersed "white" light. The purpose of the lamps is to measure pixel-to-pixel nonuniformities in detector response,

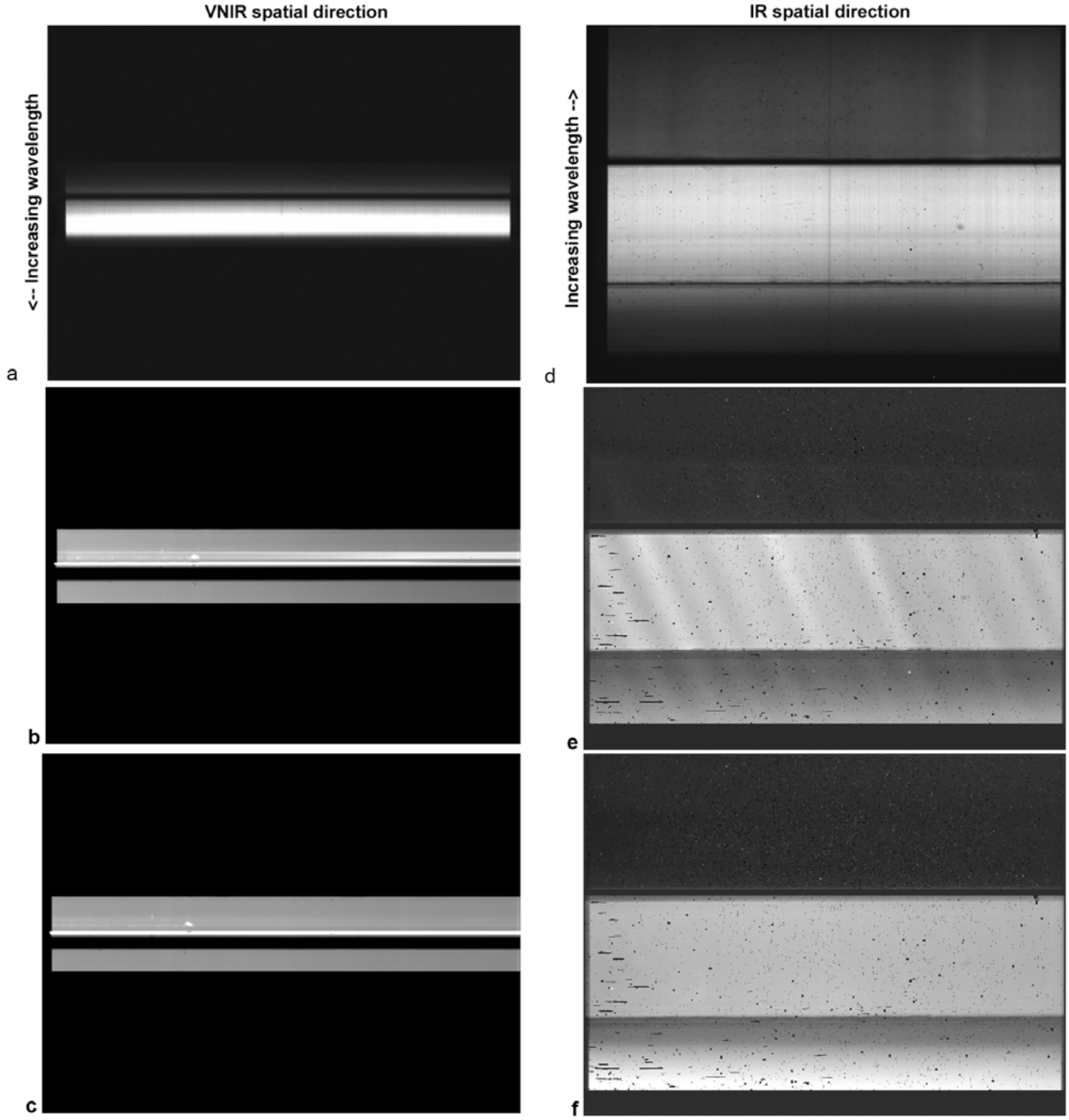


**Figure 19.** Background-removed frames taken using lamps in the calibration subsystem. Frames were taken using onboard wavelength filters that return 107 rows in the VNIR and 438 rows in the IR, then reconstructed to full frames and stretched to enhance detail. (a) VNIR frame taken looking into the integrating sphere. The narrow dark band is the zone 1–zone 2 boundary. Shorter wavelengths are at the top. (b) VNIR frame illuminated by VNIR focal plane lamp 1. (c) VNIR frame illuminated by VNIR focal plane lamp 2. (d) IR frame taken looking into the integrating sphere. The narrow dark bands are the zone 1–zone 2 and zone 2–zone 3 boundaries. The black specks are bad pixels; note their greater abundance in Figures 19e and 19f, obtained at a 125°K detector temperature, compared with Figure 19d, which was obtained at a 102°K detector temperature. Shorter wavelengths are at the bottom. (e) IR frame illuminated by IR focal plane lamp 1. (f) IR frame illuminated by IR focal plane lamp 2.

at brightness levels that are unattainable using dispersed light from the sphere bulbs. This is particularly important for the VNIR detector, where <500-nm radiance from the sphere is low. All four of the bulbs are identical to the sphere bulbs except for their mounting. The VNIR bulbs are mounted in the spectrometer housing to directly illuminate the focal plane. For the IR detector the cold shield prevents a direct view, so the lamps illuminate the detector by

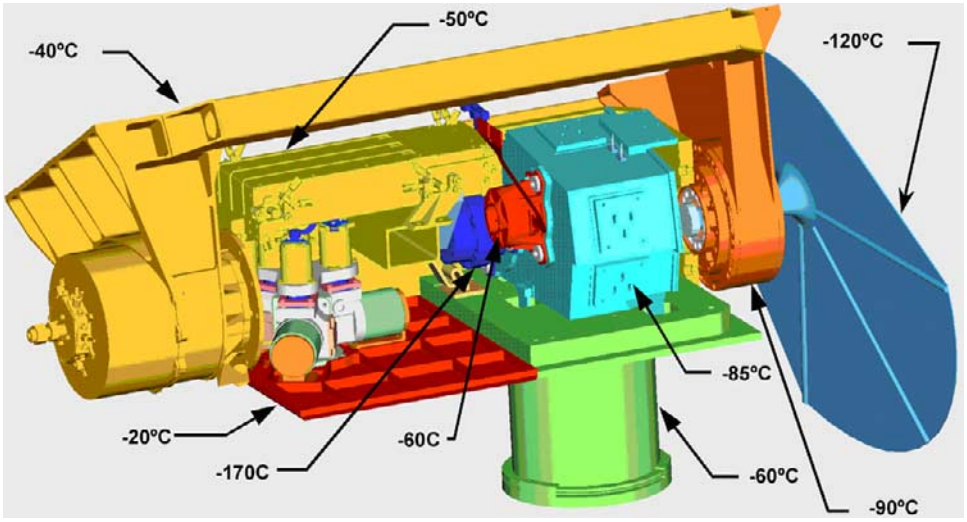


**Figure 20.** CAD rendering of a cutaway view of the OSU, color-coded to show thermal zones of the instrument. Expected temperatures during the Primary Science Phase are indicated.

flooding the spectrometer housing to create indirect illumination. The lamps' currents are only commandable directly, open loop. Example image frames illuminated by VNIR lamps 1 and 2 are shown in Figures 19b and 19c, and example IR image frames illuminated by IR lamps 1 and 2 are shown in Figures 19e and 19f. Unfortunately the spatial non-uniformity of the lamps' illumination of the detectors is so non-uniform, with glint and shadows, that reduction of focal plane lamp data has proven extremely complicated and a different approach has been adopted to measure non-uniformity as described in section 5.4.2. Focal plane lamp measurements will still be taken monthly as a contingency.

[83] Each of the calibration lamps has an expected lifetime much longer than MRO's Primary Science Phase. The expected number of cycles on the primary (VNIR-controlled) sphere lamp is 3000–15,000, depending on how frequently it is used in flight. In contrast the expected number of cycles on the backup (IR-controlled) sphere lamp and the focal plane lamps is $\ll$1000. A flight spare lamp of the same design was tested to >20,000 cycles with no change in performance.

### 4.5. Thermal Control

[84] CRISM's thermal design is driven by several sometimes conflicting requirements:

[85] 1. Maintaining the spectrometer housing at or below −75°C to minimize IR thermal background radiation.

[86] 2. Maintaining the VNIR detector at −60°C to retain quantum efficiency at >900 nm.

[87] 3. Maintaining the IR detector at <120°K to minimize dark current.

[88] 4. Maintaining the optics near −60°C to control their thermal emission at the longest IR wavelengths.

[89] 5. Maintaining the mechanical coolers above −40°C for cooling efficiency and to prevent leakage of their He refrigerant.

[90] These goals are met through a combination of passive and active cooling that create the required thermal zones (Figure 20). Components to the thermal control subsystem are shown in Figure 21.

[91] There are three radiators that provide passive cooling, plus heaters on those components where a minimum temperature must be maintained. The largest of the three radiators, the anti-sunward radiator or cryoradiator (at right in Figures 20 and 21), faces toward the terminator from MRO's 3 PM local solar time sun-synchronous orbit. Its purpose is to cool the spectrometer housing. The anti-sunward radiator is constructed from an oriented-strand composite that provides more thermal conductivity than alternative metallic choices for radiator construction. The "duck-foot" shape increases radiator area while not interfering with the spacecraft deck when the OSU gimbals. Ribs provide mechanical rigidity. The anti-sunward radiator is connected to the spectrometer housing by a flexible link. Where the radiator stem passes through the gimbal base, a polymer spacer provides thermal isolation. A trim heater on the spectrometer housing prevents temperature from falling low enough to cause icing of the optics or to overwhelm the heater on the VNIR detector.

[92] The optical bench is exposed on the exterior of the instrument and is one half of the planet-facing radiator that is oriented toward Mars during the Primary Science Phase. It cools the telescope optics to minimize thermal emission at the longest IR wavelengths.

[93] The other half of the planet-facing radiator is the plate to which the bodies of the three mechanical coolers are thermally sunk. Its function is to dissipate heat from the coolers. A trim heater plus a spacecraft survival heater keep the cooler bodies above −25°C during cold excursions such as during cruise to Mars. A narrow gap between the two segments of the planet-facing radiator maintains their distinct temperatures.

[94] The IR detector is maintained below 120°K by an active cooling system that utilizes three He-charged mechanical coolers, each linked to the IR detector by a $CH_4$-charged cryogenic diode heat pipe (CDHP). The CDHPs

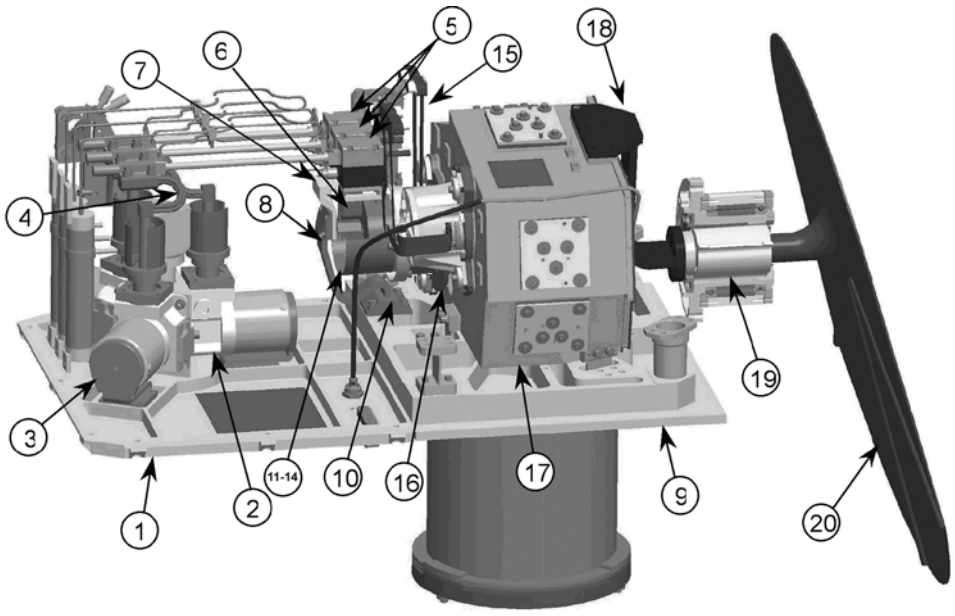


**Figure 21.** Key CRISM thermal control components. (1) Planet Facing Radiator, built by APL. (2) Cryocooler, built by Ricor, Israel. (3) Cooler-radiator flex link, built by Space Dynamics Laboratory (SDL), Utah. (4) Cooler cold tip-diode heat pipe condenser, SDL. (5) Diode heat pipe assembly, Swales Aerospace, MD. (6) Heat pipe evaporator-IR FPA flex link, SDL. (7) Heat pipe shroud bracket, APL. (8) Diode heat pipe-optical bench flex link, SDL. (9) Optical bench, SSG Precision Optics, MA. (10) IR FPA isolation assembly, APL. (11) IR FPA mount and packaging, Judson, PA. (12) IR detector and ROIC, Rockwell Science Company, CA. (13) Order sorting filter, Rockwell Science Company, CA. (14) Circuit board assembly, APL. (15) Manganin wire cable assembly, Tayco, CA. (16) IR FPA alignment shim, APL. (17) Spectrometer housing, SSG. (18) Spectrometer-Anti-sunward radiator flex link, SDL. (19) Radiator isolator, APL. (20) Anti-sunward radiator, XC Associates, NY.

provide thermal conductivity to a cooler that is on, and thermal isolation from a cooler that is off.

[95] The coolers are the Ricor K508 model charged with 30 bars of He, and were specially selected from the top 2% of the product line on the basis of high heat lift capacity and a high ratio of heat lift to current drawn. With the cooler body near $-20°C$ approximately 700 mW of heat lift is available. The cooler cold tip is connected to a heat pipe with a copper braid. Each cooler draws 450–550 mA of current at 15 V to cool the detector to $\sim 104°K$.

[96] The heat pipe is a sealed tube containing a condenser on the cooler end, a wick that connects the condenser with an evaporator on the detector end, and a liquid trap on the detector end. When the cooler is off and the detector is cold, the liquefied methane is in the liquid trap and does not circulate; the tortuosity of the wick provides low thermal conductivity. When the cooler is powered on and the condenser end reaches approximately $138°K$, the methane begins to liquefy there and is wicked to the evaporator where it removes heat, and vapor returns to the condenser end to continue the cycle. After cooler turn-on, the system reaches temperature in approximately 12 hours.

[97] The heat pipes are enclosed in a shoebox-shaped cold shroud that envelops the assembly and minimizes radiative coupling to the rest of the instrument. The shroud is thermally coupled by a flexible link to the optical bench, and suspended from the warm side of the instrument housing by Kevlar cables. The heat pipes are supported inside the shroud by a second set of small-diameter Kevlar cables, creating a dual-nested Kevlar cable thermal isolation/structural support system. The shroud is gold-plated for low emissivity to minimize radiative coupling.

[98] The OSU has been baked out in vacuum during cruise for $\sim$60 days to dissipate water adsorbed during prelaunch conditions. Water adsorbed on surfaces inside the cold shroud would raise emissivity, increase radiative coupling of the heat pipes to their surroundings, and increase the amount of heat that each cooler has to remove. Ultimately some of the water desorbed from other parts of the instrument interior would condense on the $\sim 105°K$ surfaces of the IR detector and the active heat pipe, increasing heat load on the cooler and perturbing radiometric calibration especially near 3000 nm. Apparently the bake-outs have been successful: approximately 10% less current is drawn by each cooler to maintain the IR detector at cryogenic temperature than was required during ground testing in vacuum after four days of bakeout.

[99] The design of the active cooling system is discussed in more detail by *Bugby et al.* [2005].

### 4.6. Scanning System

[100] The scanning subsystem consists of the Gimbal Motor Electronics (GME), a high-resolution angular encoder, the gimbal drive motor, and the OSU base. The GME contains the motor driver circuitry, and responds to a commanded profile from the DPU. Software in the DPU implements a control algorithm, utilizing feedback information from the 20-bit, 6-$\mu$rad precision angular position

encoder to maintain closed-looped control. The system accurately follows a programmed scan pattern that is carefully designed to compensate for orbital motion and to accomplish the desired scan pattern across the Martian surface, with a precision of ±25 $\mu$rad. The control algorithm is described in greater detail in section 4.8.3.

[101] Electrical connection of the OSU to the DPU and GME is provided by a twist capsule that passes wires through the hole in the center of the motor-encoder system.

### 4.7. Data Processing Unit

[102] The DPU (Figures 7 and 8) receives unregulated 28–32 volt power from MRO and provides regulated secondary power to CRISM, receives and processes commands from MRO, controls the CRISM subsystems, and acquires and formats CRISM science and housekeeping data that is then sent to the spacecraft solid-state recorder (SSR) for downlink to earth.

[103] The DPU is based upon the modular stacking electronics system developed for CONTOUR/CRISP and several of the instruments on MESSENGER. The CRISM design consists of eight electronics boards, although there are only 4 unique board designs. Two of the board designs are closely based on existing MESSENGER board designs.

[104] The DPU consists of a Processor System and a Power System. The Power System consists of DC/DC converter boards with additional circuitry, one each for the coolers, IR focal plane, VNIR focal plane, and the remaining DPU boards. The DPU Power Board receives primary power from the spacecraft and distributes it through an internal stacking connector to all boards in the Power System. An $I^2C$ serial data bus from the Processor Board controls all functions on the Power System boards. The $I^2C$ serial data bus and primary power distribution allow for "daisy chaining" of additional Power System boards as required. Each of the power boards also telemeters its own temperature and the currents and voltages being supplied by it.

[105] The Processor System consists of Processor Board, a Spacecraft Interface Board, and two Focal Plane Interface Boards (one per focal plane). The Processor System boards use Actel field-programmable-gate-array (FPGA) signals routed to an internal stacking connector for interfaces between boards. The Actels are programmed to implement a data bus between boards, allowing for "daisy chaining" of additional Processor System boards as required. The Processor Board controls IR and VNIR focal plane power and cooler power via its $I^2C$ bus, and gimbal position using a serial RS422 interface to the GME. The Spacecraft Interface board communicates with the spacecraft via serial low-voltage differential signal (LVDS) command and telemetry interfaces, receives spacecraft time synchronization and side A/B selection via a hardware signal, and transmits science data to the SSR via serial LVDS interfaces for the IR and VNIR focal planes. The Focal Plane Interface Boards provide clock, frame, and command data signals to the IR and VNIR focal plane electronics under control of the Processor Board. They receive focal plane data and perform data editing compression as described in section 4.8.1. The Processor Board generates telemetry headers for image data and passes them to the Focal Plane Interface Boards for incorporation onto image frames before transmission to the SSR.

### 4.8. Software

[106] The core software on CRISM is inherited from recent planetary instruments built at APL. Core functions include autonomy, spacecraft interface, basic thermal control, and the macro system described below. Data compression is partially derived from that in the MESSENGER/MDIS camera, whereas cooler and gimbal control and focal plane lamp control are derived from the CONTOUR/CRISP instrument. Features specific to CRISM include wavelength-dependent compression, observation control, and closed loop control of the internal integrating sphere.

#### 4.8.1. VNIR and IR Detector Control

[107] Key variables ("configurations") in constructing observing scenarios include the following. All are independently selectable separately for the VNIR and IR detectors.

##### 4.8.1.1. Image Source

[108] Image data may be generated using digitized output from the detector, or using one of up to seven test patterns stored in the focal plane electronics.

##### 4.8.1.2. Frame Rate

[109] Frame rates of 1, 3.75, 5, 15, and 30 Hz are supported. The 1 Hz frame rate is used for hyperspectral measurements of the onboard integrating sphere, because the long exposures possible at 1 Hz are needed for appreciable SNR at the shortest VNIR wavelengths. 3.75 Hz is used for hyperspectral measurements of Mars; this is the highest frame rate at which the DPU electronics support onboard compression options over the range of wavelengths imaged onto the detectors with useful SNR. 15 and 30 Hz frame rates are used for nadir-pointed multispectral measurements that return only selected wavelengths. The 5 Hz frame rate is not planned for use in flight, because at that rate the electronics do not support compression of a hyperspectral wavelength selection, and it would produce excessive along-track smear in a nadir-pointed observation.

##### 4.8.1.3. Integration Time

[110] Integration times are in increments of 1/480th of the inverse of the frame rate. At 1 Hz, for example, available integration times are 1/480th sec, 2/480th sec..480/480th sec, and at 15 Hz, 1/7200th sec, 2/7200th sec..480/7200th sec.

##### 4.8.1.4. Compression

[111] All CRISM data are read off the detector in 14-bit format and are compressed real-time in hardware. Compression options, in succession (Figure 22), are as follows:

[112] 1. Subtraction of an offset, on a line by line basis: Offsets are set by uploading a data structure to the DPU.

[113] 2. Multiplication by a gain, on a line by line basis, with the output in 12-bit format: Gains are set by uploading a data structure to the DPU.

[114] 3. Row selection: All detector rows having useful signal can be saved, or alternatively an arbitrary, commandable subset of rows (a "wavelength filter") can be saved. The number of rows with useful signal is 544, 107 in the VNIR and 437 in the IR. One extra row is returned from the IR detector to measure electronics background. The nominal number of rows for multispectral mode is 73, 18 in the VNIR and 55 in the IR. For each detector, there are four wavelength filters from which to choose rapidly by command: hyperspectral (545 total channels, in three contiguous blocks), multispectral (73 total channels), and two sets of

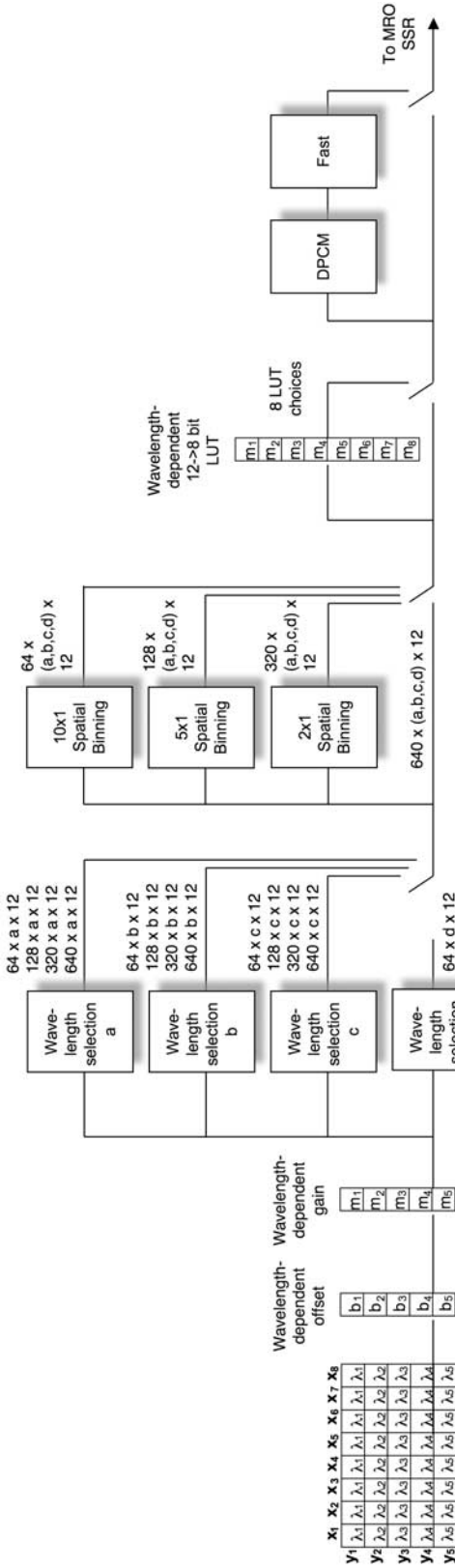


**Figure 22.** Schematic representation of the CRISM data compression pipeline. Data are read off the detectors as 14-bit values. A wavelength-dependent, commandable offset is subtracted, and the difference is scaled by a wavelength-dependent, commandable gain to yield 12-bit values. One of four commandable wavelength filters is then used to save only selected rows (wavelengths) of the frame of 12-bit data. The selected wavelengths are binned spatially to any one of four selected options. Optionally, the resulting spatially binned selected wavelengths can be converted from 12 to 8 bits using any of 8 LUTs; the choice of LUTs is commandable on a wavelength-by-wavelength basis. Finally, the output data can be losslessly compressed.

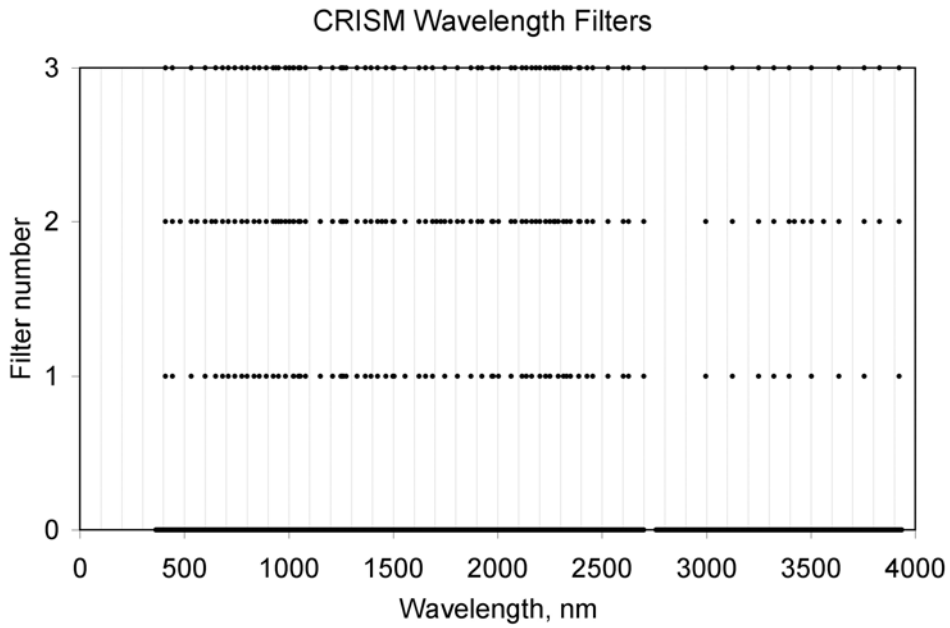


**Figure 23.** Wavelength filters at the beginning of the primary science phase. Filter 0 is for targeted, hyperspectral observations, and filter 1 is the nominal selection of wavelengths for the multispectral survey. Filters 2 and 3 provide additional coverage of key absorption bands.

expanded multispectral (82 and 94 channels). New options are set by uploading a data structure to the DPU.

[115] 4. Pixel binning: Pixels can be saved unbinned or binned 2x, 5x, or 10x in the spatial direction. No pixel binning in the spectral direction is supported.

[116] 5. Optionally, conversion from 12 to 8 bits using one of eight look-up tables (LUTs) specified on a line by line basis: The line-by-line choices are set by uploading a data structure to the DPU. The LUTs are stored in non-volatile memory and are not uploadable.

[117] 6. Optionally, lossless Fast + differential pulse-code modulation (DPCM) compression.

[118] The offsets, gains, and row-dependent LUT choices were set following instrument calibration. Offsets were derived from measurements of bias at different frame rates and detector temperatures (section 5.3.3), so that the minimum 14-bit DN at any frame rate over the range of expected operating temperatures translates to a positive, non-zero value. A single, wavelength-independent value is used for each detector.

[119] Gain and LUT choices were set following determination of instrument responsivity and estimation of signal levels and SNRs for Mars (section 5.2). The gain settings were driven by four requirements: (1) 12-bit sampling near the level of read noise so that SNR would be effectively improved by spatial pixel binning, (2) avoiding saturation, (3) maintaining appreciable SNR at photon-starved wavelengths, and (4) operation considerations, i.e., avoiding repeatedly changing settings. The driving cases are VNIR observations of the internal integrating sphere and VNIR and IR observations of icy regions Mars. The wavelength-dependent LUT choices were made to avoid 8-bit saturation while also minimizing quantization errors at expected signal levels in multispectral mode observing Mars.

[120] Selection of the multispectral wavelength filters (Figure 23) was a research project [*Pelkey et al.*, 2007]. OMEGA data were used to generate a core set of wavelengths needed to accurately capture the centers and shapes of absorption bands and key spectral ratios due to minerals known to be present (olivine, pyroxene, ferric oxides, sulfates, and clays) or sought after (carbonates), or due to known atmospheric constituents. These were augmented with companion wavelengths needed to subtract a leak of the 2nd order from the grating through the IR order sorting filter at nominal wavelengths >2800 nm (section 5.3.2). The extended sets contain additional wavelengths that serve two functions: (1) to better characterize absorptions due to bound water in sulfate phases inferred from OMEGA data or (2) to measure the centers and shapes of absorptions possibly present on Mars at low abundances, but not detected by OMEGA (e.g., nitrates, phosphates).

#### 4.8.2. Calibration Subsystem Control

##### 4.8.2.1. Calibration Lamps

[121] 4095 levels are commandable in each of two lamps at each focal plane, and in two lamps in the integrating sphere. All settings are open-loop, meaning that current is commanded directly. For the integrating sphere only, closed loop control is available at 4095 settings. For closed loop control, the setting refers to output from a photodiode viewing the interior of the integrating sphere; current is adjusted dynamically to attain the commanded photodiode output.

##### 4.8.2.2. Shutter Position

[122] The stepper motor running the shutter has 33 positions, and can be commanded in two modes. It may be commanded to move a discrete number of steps, or it may be commanded to a predefined position (open, closed, or viewing the integrating sphere). In software, open = 3, sphere = 17, and closed = 32.

**Table 4.** Observation Control Table

| Column 1 | Column 2 | Column 3 | Column 4 | Columns 5–22 | Column 23 | Column 24 | Column 25–42 |
|---|---|---|---|---|---|---|---|
| Target id: | profile id | $m_0$ | $m_1$ | ... | $dmt_0$ | $dmt_1$ | ... |
| Target id: | profile id | $m_0$ | $m_1$ | ... | $dmt_0$ | $dmt_1$ | ... |
| Target id: | profile id | $m_0$ | $m_1$ | ... | $dmt_0$ | $dmt_1$ | ... |
| ... | ... | ... | ... | ... | ... | ... | ... |

#### 4.8.3. Scan System Control

[123] A torque motor under software control moves the gimbal. Pointing toward nadir is defined as 0°. The gimbal can move back and forth between hard stops at −60° and +60°. The software also limits the gimbal to stay within a minimum and maximum position. These "soft" stop angles are uploadable. The motor includes a relative position encoder and an index pulse at a known position. Until the software is commanded to find the index, the software does not have absolute knowledge of the gimbal's position. The software searches for the index by moving the gimbal back and forth between the hard stops. A hard stop is recognized via a limit switch or a motor stall condition.

[124] Once per second the software computes one second's worth of angular positions and velocities to follow over the next second. The software tries to remove differences between the computed values and the platform's actual position and velocity using a Proportional Integral Derivative (PID) algorithm. The PID control parameters are uploadable.

[125] The gimbal control software can be commanded into several different modes where the tables of positions and velocities are computed in different ways. When the mode is off, the motor is not driven. In hold mode, the platform is held at the current position. In slew mode, the platform is moved to a commanded angle. In profile mode the platform's desired angle and velocity are computed such that the spectrometer points to a fixed target on the Martian surface as the spacecraft passes over the target. The platform's angle versus time is an S-shaped curve. CRISM software stores ~1800 S-curve profiles. New or replacement profiles can be uploaded. The upload is not the angle versus time curve itself, but the coefficients of a polynomial approximation of the ratio of downtrack target distance to spacecraft altitude. Offsets or constant-rate scans can be superimposed on top of the commanded angle.

[126] Using these capabilities, typical observations include either of two basic gimbal pointing configurations and two basic superimposed scan patterns. Pointing can be (1) fixed (nadir-pointed in the Primary Science Phase, a.k.a. pushbroom) or (2) dynamic targeting, tracking a target point on the surface of Mars and taking out ground track motion. Two types of superimposed scans are supported: (1) a short, 4-second duration fixed-rate ("EPF-type") scan which superimposes a constant angular velocity scan on either of the basic pointing profiles or (2) a long, minutes-duration fixed-rate ("target swath-type") scan. For dynamic targeting, the motion of the slit projected onto the surface is primarily a combination of gimbal movement and spacecraft velocity with slight variations due to continuous spacecraft yawing, and rolling in the case of off-nadir targeting. Ground and flight testing show that the gimbal tracks its commanded profile with a precision of ±25 $\mu$rad (Table 3a).

[127] The scan platform control software can be placed in a diagnostic mode by command. In this mode, high rate scan data replaces image data.

#### 4.8.4. Instrument Macros

[128] A macro is a sequence of commands that can be stored and then executed later. A macro can be any length as long as the total length of all the macros fit into available memory. Up to 256 macros may be defined; each macro is identified by a small integer, 0–255. A macro is loaded to the instrument by placing CRISM in a "learning" mode to define a macro. If a command arrives with its macro field indicating "learn", the command is added to the macro currently being constructed. Any command that arrives without the "learn" field is executed immediately. There are commands for running and stopping a macro. There are also special commands for adding delays to a macro; these can be used only within a macro. One macro can call another or can execute loops. Both calls and loops can be nested. Up to 64 macros can be running concurrently.

[129] Several default macros are available as soon as CRISM is started, and are used to control instrument autonomy.

#### 4.8.5. Observation Control

[130] An observation is defined as the execution of a stored sequence of macros while the scan platform follows a desired profile. For the observation to be useful the spacecraft must be oriented properly and the command sequence and scan profile started at the correct time. Consequently, the spacecraft computer is intimately involved in observation control.

[131] Two blocks of observation data are uploaded for each target, one to the spacecraft computer and one to CRISM. Both blocks include a unique target identifier (target ID). The spacecraft observation data also includes the target's latitude and longitude, an estimate of closest approach time tCA, and an offset dt1 from tCA indicating how long before closest approach to start observing. Using orbit and target data, the spacecraft computes the actual tCA. As the spacecraft nears the target, it rolls to allow CRISM to view the target and notifies CRISM.

[132] The data uploaded to CRISM (Table 4) contains the target ID, a scan profile ID, and a list of macros ($m_0$, $m_1$, $m_2$, ...) and time offsets between their execution ($dtm_0$, $dtm_1$, $dtm_2$, ...). The relative timing of the macros will vary with the target.

[133] The spacecraft starts a CRISM observation by sending CRISM a command ("CRM_OBS_START") some time before tCA−dt1. The command has the target ID, tCA, and dt1. When CRISM receives the command, it uses the target ID to find the corresponding stored target data. The scan profile identifier is extracted and, using tCA, the scan profile computation begins. The first macro of the target is run (m0) at tCA – dt1. After the first offset time elapses (dmt0), the second macro is run (m1). This process repeats until all of the macros are run or an offset time of 65535 seconds is encountered. When the spacecraft sends the CRM_OBS_START command, it also prepares the SSR for receiving CRISM images. After the last macro of the

**Table 5.** Calibration Strategy for the CRISM Instrument

| Variable | Ground Measurement | In-Flight Measurement |
|---|---|---|
| Wavelength in spectral direction on detector | Monochromator scans, >5 positions along slit | Center wavelengths of Mars atmospheric gas bands |
| | Extended sources with known spectral lines (lasers and line lamps illuminating a Spectralon-lined integrating sphere) | |
| Bias | Regression using different exposures with shutter closed | Regression using different exposures with shutter closed |
| Linearity | Calibrated source at different signal levels | Calibration lamp at different exposure times |
| Background (sum of dark current and IR thermal background) | Shutter-closed measurements at different spectrometer housing, detector temperatures | Shutter-closed observations interleaved with Mars observations |
| Spectral responsivity | Reference radiance sources (halogen lamp-illuminated Spectralon plane, blackbody source) in conjunction with internal sphere for cross-calibration. | Internal integrating sphere |
| Spatial flat field | Ratio of internal sphere images to images of Spectralon plate | IR: Internal sphere images. VNIR: average of large number of images of bland region of Mars |
| MTF (spatial direction) | Resolution target and point sources at focus of collimator | – |
| Wavelength in spectral direction on detector | Extended sources with known spectral lines | Mars atmospheric gas bands |
| PSF (spectral direction) | Monochromator scans, >5 positions along-slit | – |
| PSF (spatial direction) | Inner zone from point source scanned across slit. Distal from small extended source | mag <1 star (for sufficient SNR at all wavelengths) |
| Detector alignment | Point source scanned across slit | mag <1 star (for sufficient SNR at all wavelengths) |
| Pivot plane orientation | Optical cube alignment | mag <1 star at 2nd position in pivot plane |
| Position within plane | Rate table and theodolite | Star measurements as used for pointing calibrations |
| IFOV | Point source at known angles | Star measurements as used for pointing calibrations |

observation is run, CRISM notifies the spacecraft so that the SSR can be closed.

#### 4.8.6. Thermal Control

##### 4.8.6.1. Cooler Control

[134] The CRISM coolers are operated with a modified Proportional Integral (PI) control loop. The CRISM software calculates the error (difference between the goal and actual cooler cold tip temperature), and applies the control algorithm to compute a digital value commanding the cooler level and sends the result to a digital to analog converter. The digital value ranges from 0 to 4095 and controls how fast the cooler motor runs. The control algorithm runs at 5 Hz.

[135] The algorithm operates in two modes. If the error is above a threshold, only the proportional (P) part of the algorithm is applied. The error is multiplied by a gain and an offset is added. Once the error drops below the threshold, both the proportional and integral (PI) terms are applied. The error is added to the integrated error. Limits are placed on both the error to add and the total integrated error.

##### 4.8.6.2. Heater Control

[136] The CRISM DPU controls the temperature of five zones of the instrument: two that encompass the focal plane electronics boards in the base of the instrument, plus the cooler bodies, the spectrometer housing, and the VNIR detector. The heater in each zone may be commanded off, on, or controlled by software. If a heater is being controlled by software, it uses a goal and hysteresis commanded for that zone. Every second the zone's temperature is compared against its limits. If the temperature is too low, the heater will be turned on. If the temperature is too high, the heater will be turned off.

#### 4.8.7. Status Reporting and Autonomy

[137] A collection of environmental data is monitored by CRISM including voltages, currents, and temperatures. These analog values are read every second or more frequently. Each monitored item has a lower and upper limit. If an item is out of limit for one cycle, but back within limits on the subsequent cycle, a transient alarm is reported. An alarm ID indicates the item being monitored and whether the value was too low or too high. The values accompanying the alarm are the out of limit data and the corresponding limit. If an item is either too high or two low for two consecutive monitoring cycles, a persistent alarm is reported. For some out of limit conditions, the software will execute a macro in response to power off the subsystem that generated the alarm.

#### 4.8.8. Data Transmission

[138] CRISM data are sent via three dedicated links to the spacecraft SSR for downlink to the ground. A low-speed link is used for once-per-second or less frequent reports of voltages, currents, and temperatures via the spacecraft interface board in the DPU. These "status packets" also contain the commanded software and power configuration of the instrument. The low-speed link also transmits alarms, and can be commanded to transmit dumps of memory contents, the onboard macro library, or a memory "checksum" (the last bits of the sum of memory contents) as health and status checks.

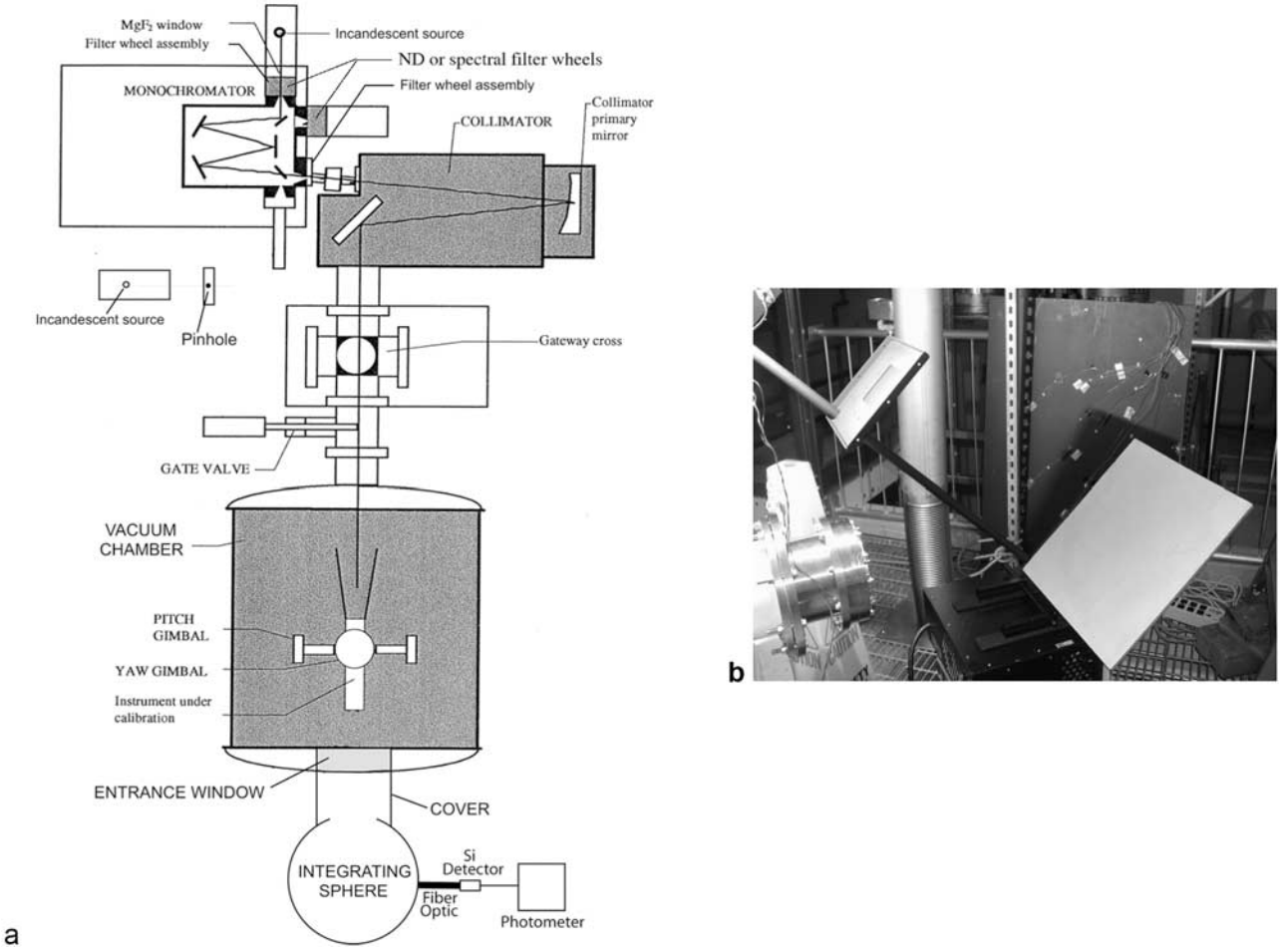


**Figure 24.** (a) Optical Calibration Facility (OCF) hardware configuration used for CRISM calibration. (b) Spectralon plate used for radiometric calibration, illuminated by a NIST-traceable halogen lamp at the upper left. The plate was mounted in place of the integrating sphere in Figure 24a. The small panel at the upper left, below the lamp, contains a shutter used to block direct illumination of the plate in order to take measurements for subtraction of the ambient background light.

[139] The VNIR and IR detector each have a dedicated high-speed link to the SSR via its interface board in the DPU. Each row of an image frame is prefaced with a line number to track its wavelength, and each image frame is prefaced with a header containing the spacecraft time, target ID, and gimbal position at the beginning, middle, and end of frame integration, as well as a snapshot of the contents of the status packet at the time of frame measurement.

## 5. Testing, Calibration, and Performance

### 5.1. Calibration and Testing Strategy

[140] Calibration occurred on ground and continues in flight, the latter using recurring measurements that accompany measurements of Mars (e.g., shutter-closed measurements and measurements of the internal integrating sphere and focal plane lamps) as well as special observations including star measurements. Ground calibration characterized those attributes that are difficult to measure in flight, such as spectral response functions and linearity. Calibration also establishes the baseline performance of the onboard calibration subsystem (such as the radiance field of internal sources) that is needed to process in-flight calibrations. Overall calibration strategy for CRISM is summarized in Table 5.

[141] Ground calibration occurred in six stages:

[142] 1. The VNIR and IR detectors were characterized individually at temperature for detector-specific attributes such as bias, dark current, and linearity.

[143] 2. The detectors were aligned in the optical assembly for best focus and to minimize optical distortions including spectral smile, keystone, and rotation of the detector relative to the beam. At the same time, data were collected to characterize the calibration subsystem and optical performance.

[144] 3. The integrated system was tested at temperature.

[145] 4. Following environmental testing, calibrations not requiring collimated light were repeated during thermal balance measurement of the instrument.

[146] 5. Measurements requiring collimated light were repeated.

[147] 6. After initial delivery and integration onto the MRO spacecraft, CRISM and the other instruments were refitted with a newer design of FPGAs to eliminate a failure mode that occurred in a number of parts, whereby a bit in

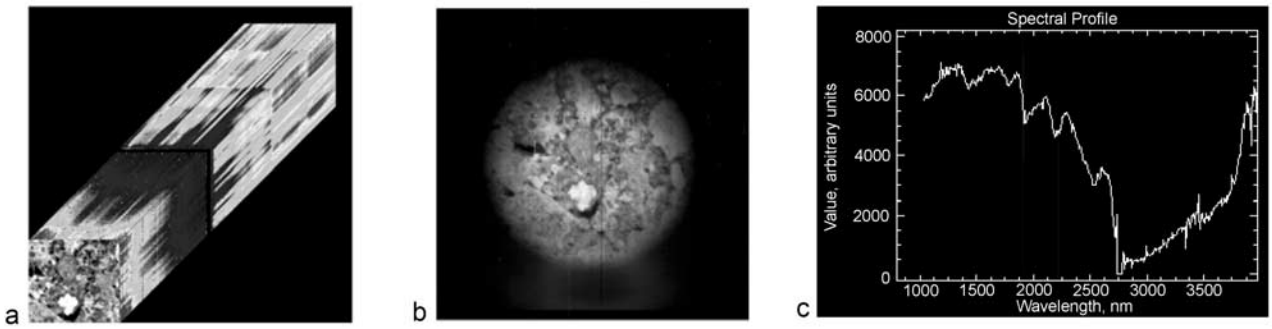


**Figure 25.** Schematic representation of CRISM data. (a) Hyperspectral image "cube" whose flat upper surface is a single frame such as in Figures 18 and 19. The whole cube is built from a stack of such frames. (b) Spatial image of a breccia taken at a single wavelength; each horizontal line is taken from the same row (wavelength) of a succession of data frames. (c) IR spectrum of a single pixel in the middle panel, corresponding to a column from single frame.

coded logic flipped. Following the FPGA replacement, key calibrations were repeated.

[148] Stage 1 was completed at the Optical Development Laboratory at APL. Stages 2, 3, 5, and 6 were completed at the Optical Calibration Facility (OCF) at APL (Figure 24). Observations were acquired either looking out a sapphire window at one of several calibrated field-filling radiance sources (a blackbody, a gold-lined integrating sphere, a Spectralon-lined integrating sphere, and Spectralon and rare earth oxide-doped Spectralon plates illuminated by a halogen lamp), or through a collimator looking at sub-pixel or extended white light or monochromatic sources, a military resolution target, or various geologic hand samples to validate calibration. Stage 4 was completed at APL's Space Simulation Laboratory in a thermal vacuum chamber outfitted with a sapphire window, viewing a blackbody or the halogen lamp-illuminated Spectralon plates. In all cases, observations of external sources were accompanied by measurements of the internal calibration subsystems. During stages 1 and 2 over 168,000 frames of VNIR or IR data were acquired, and during stages 3 through 6 over 946,000 frames were acquired, typically in bursts of 12 to improve photon counting statistics. Measurements were purposely taken at a variety of frame rates and exposure times. Data were uploaded to the CRISM Science Operations Center (or SOC) which provides a graphical user interface to the data that supported basic analyses in real time including background subtraction, collection of image statistics, and data profiling. Those capabilities were most critical during detector alignment to support rapid turnaround (typically 24 hrs) of test results to support determinations of the shim thickness and detector translation required for optical focus and alignment.

[149] End-to-end system performance is shown schematically in Figure 25, which shows a single observation sequence of a geologic hand sample (a breccia), viewed through the OCF collimator window. This observation was made using a commanded series of frames identical to that constituting a targeted observation in flight. One frame of data (such as in Figures 18 and 19) represents a one-line spatial image, with each element of the line having a corresponding spectrum in the column direction of the frame. A two-dimensional spatial image of a target is built

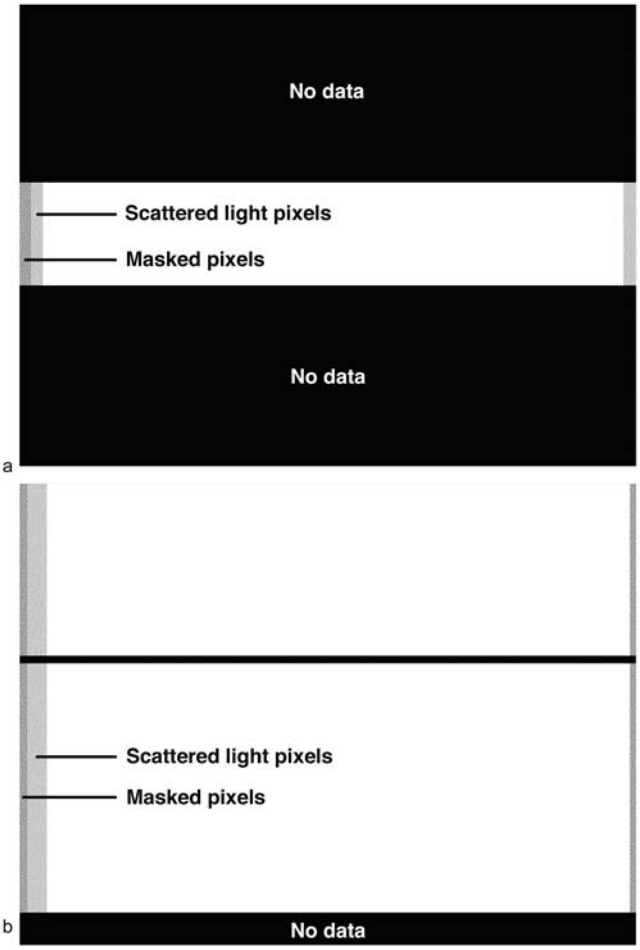


**Figure 26.** Maps of the (a) VNIR and (b) IR detectors. Areas in black do not measure useful signal and are not downlinked using the wavelength filter for hyperspectral mapping. White, pixels illuminated through slit. Light gray, exposed pixels not directly illuminated through slit that measure scattered light. Gray, physically masked pixels that measure only bias and dark current.

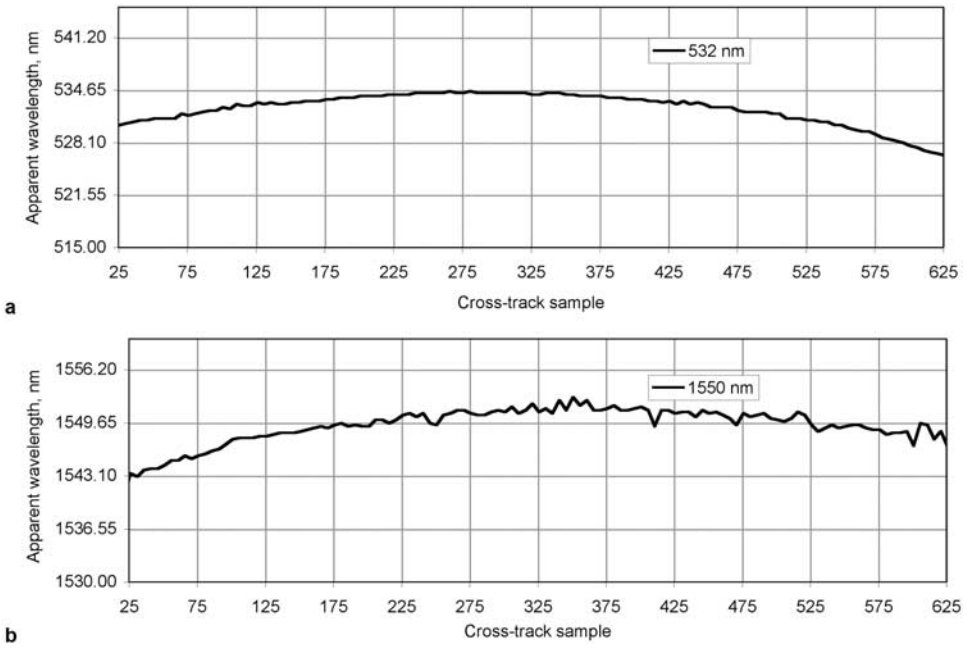


**Figure 27.** Spectral smile illustrated by along-slit variation in the apparent wavelengths of monochromatic laser line sources. The grid on the vertical axis shows 1-pixel increments, whereas the grid on the horizontal axis shows 50-pixel increments.

up by acquisition of successive data frames as the spectrometer slit's FOV is translated across a target, either by scanning CRISM's gimbal across a target (as in a targeted observation) or by motion of the FOV across the target (as in a multispectral mapping observation). The stack of resulting data frames is a multiband image, or ''image cube.'' The left panel of Figure 25 shows a multiband image, and the middle panel shows a single-wavelength slice through it. The right panel shows the spectrum for a single spatial pixel from the center panel. The absorption bands present in the spectrum are due to $H_2O$ and OH in the minerals present in the breccia.

### 5.2. Selected System-Level Performance Results

[150] Table 3a compares preliminary estimates of overall instrument performance as derived from these tests against the design requirements. All of the high-level requirements (driven at the MRO project level) on spectral range and sampling and spatial coverage and resolution are met. Most secondary requirements (internal to CRISM) are also met, though in some cases there is a small but acceptable deviation in actual performance.

#### 5.2.1. Detector Alignment

[151] The final ground calibration yields wavelength limits of 362–1053 nm in the VNIR and 1002–3920 nm in the IR, over the range of detector rows that are included in the wavelength filters used for hyperspectral observations. Measured dispersion is 6.55 nm/channel. Figure 26 shows the rows downlinked by the hyperspectral filter (wavelength filter 0) and their locations in different parts of the detector. Columns 0–11 of the VNIR detector and 0–7 and 634–639 of the IR detector are physically masked and serve as an unilluminated reference for integrity of radiometric calibration. Specifically, near-zero values in calibrated data indicate correct removal of bias, thermal background, and electronics ghosts. Columns 12–23 and 627–639 of the VNIR detector and 8–27 of the IR detector are exposed but not directly illuminated through the slit and measured glare from the gratings. Columns 25–625 of the VNIR detector and 29–632 of the IR detector measure the scene or the internal integrating sphere. Other columns are transitional.

[152] Keystone (spatial drift along a detector column) is ±0.4 pixels at the edges of the detectors, with near-zero values near column 250 on each detector.

[153] Figure 27 shows spectral smile (wavelength drift along a detector row). The total magnitude exceeds 1 pixel, with the least variation along-slit near column 275 of the VNIR detector and column 350 of the IR detector. Thus, for extraction of data from overlapping EPF measurements, columns 275–350 form the ''sweet spot'' on the detectors where optical distortions are minimal.

#### 5.2.2. Modulation Transfer Function and Scattered Light

[154] Resolving small-scale deposits (<0.01 $km^2$) on the surface of Mars is a key CRISM requirement. Figure 28 shows the instrument modulation transfer function, or MTF, a key metric of expected spatial resolution, near the edge of the FOV. The requirement of 0.2 at 9.25 cycles/mm at the detector, required to resolve a 75-m spot on the surface from MRO's nominal 300-km altitude, is exceeded at all wavelengths. By this criterion, the smallest spot resolvable all wavelengths (anywhere within the central 1.8° of the FOV) is 38 meters.

[155] Figure 29 shows the falloff in measured VNIR signal with distance from a small source, or the point-spread function. Brightness is down by a factor of $\sim 10^2$ within 3 spatial pixels and $\sim 10^3$ within 10 spatial pixels. Integrating from 0.01°–3° outside the instrument aperture defined by the slit, approximately 1.3% of the measured light in a given

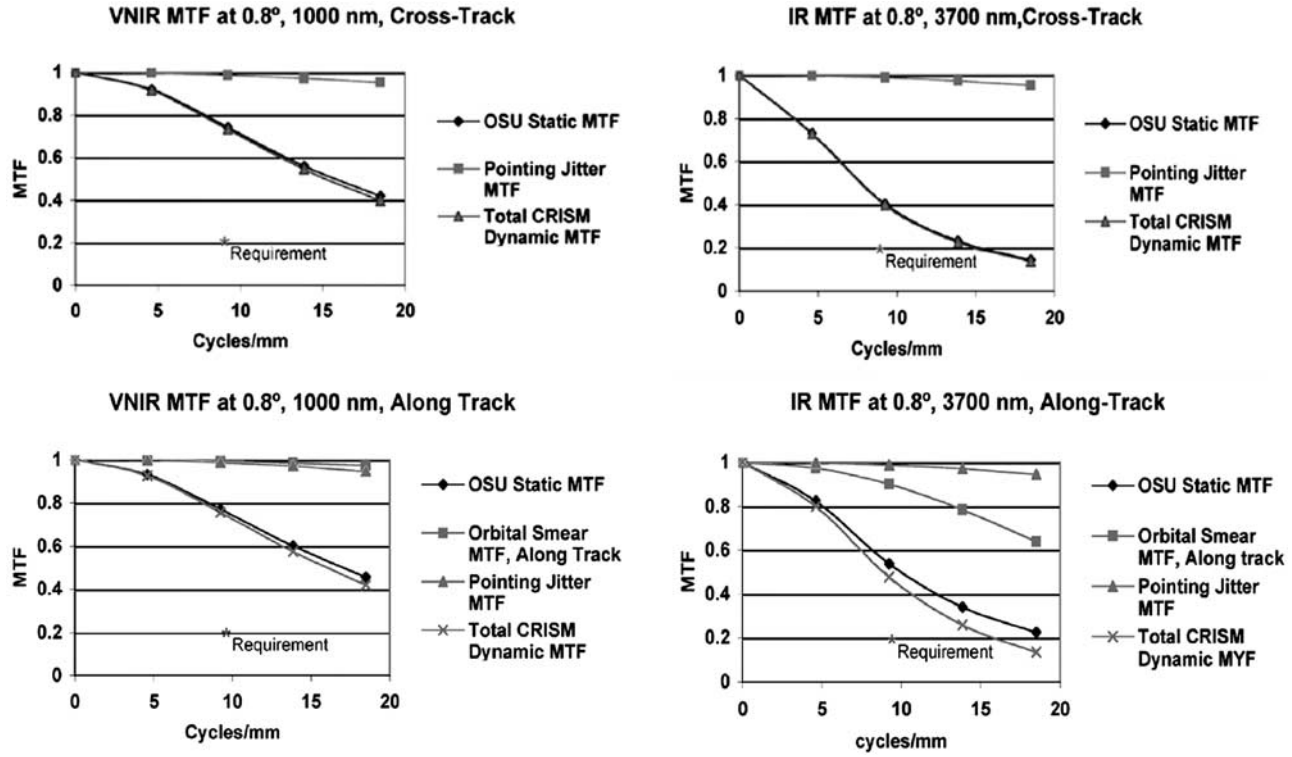


**Figure 28.** MTF predictions for flight data based on ground measurements of point sources, based on point-source measurements in the APL Optical Calibration Facility. Note that the MTF at 9.25 cycles/mm is well above the derived requirement of 0.2.

spatial pixel comes from more than 3 spatial pixels distance and 0.1% from outside 3°.

### 5.2.3. Spectral Sampling

[156] In order to distinguish spectrally similar minerals that have different geological implications for their environments of formation, adequate spectral resolution is necessary. This requires sufficiently high density spectral sampling, as well as a sufficiently narrow full width half maximum (FWHM) of the instrument response in the spectral direction. This "slit function," the effective band pass for a single detector element, represents the convolution of spectral sampling and the point-spread function in the spectral direction. CRISM's benchmark is distinguishing the minerals montmorillonite and kaolinite, which form in hydrothermal environments under different temperature regimes [*Swayze et al.*, 2003]. The requirements for this are (1) <20 nm FWHM and (2) sampling of the spectrum at this or smaller increments. CRISM's spectral sampling requirement is <10 nm/channel to provide oversampling, and the actual performance is 6.55 nm/channel. FWHM is 8 nm in the VNIR across the FOV (Figure 30). In the IR it increases from 10 nm at short wavelengths to 15 nm at the longest wavelengths at the center of the FOV, and broadens by ~2 nm to ±0.8° from the center of the FOV (Figure 31). Outside ±0.9° from the center of the FOV the telescope is slightly vignetted, so further degradation is expected at extreme field angles. (As summarized in Table 3a, the FOV is ~45% wider than the minimum requirement for swath size. The oversized FOV provides margin for covering a region of interest in a targeted measurement.)

### 5.2.4. Signal-to-Noise Ratio

[157] Extraction of mineralogically useful spectral data at high spatial and spectral resolution requires high SNR. CRISM's internal requirement of SNR 400 at 2300 nm for typical Martian materials represents 3-$\sigma$ detection of a 1% absorption band in a typical Martian material, using 3 wavelength channels. 2300 nm was chosen because it

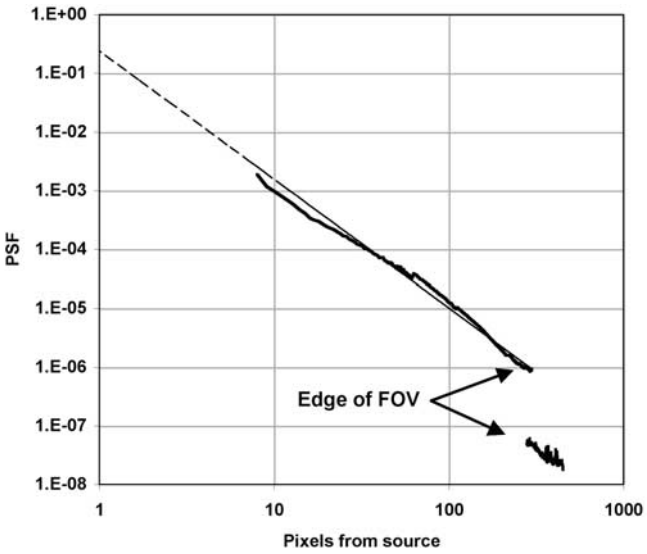


**Figure 29.** Relative response as a function of distance in spatial pixels to a 10-pixel wide source at 790 nm.

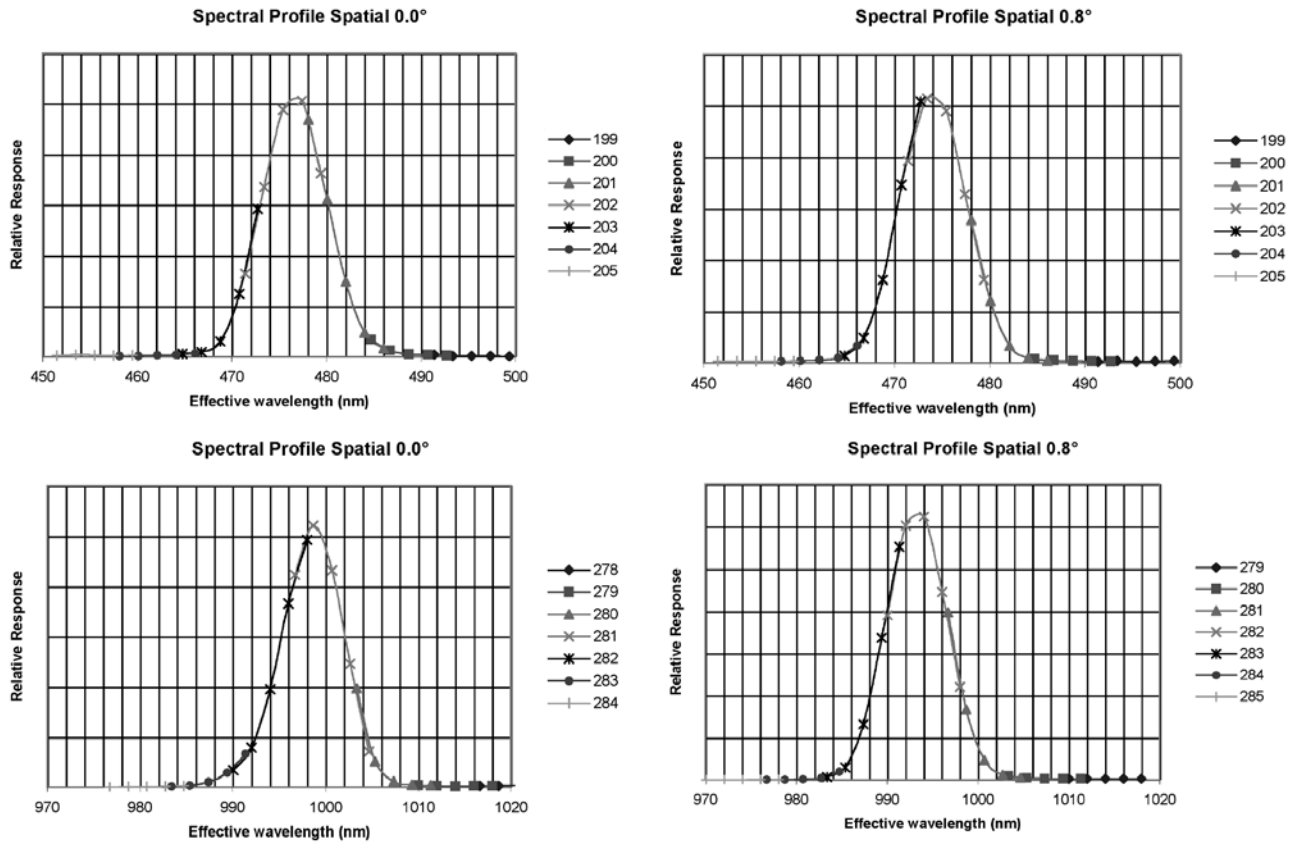


**Figure 30.** Spectral profiles at the short- and long-wavelength ends of the VNIR spectral range. Profiles were constructed by scanning a 2-nm-wide monochromatic source across the wavelength range of the detector. Symbols indicate relative response to different wavelengths of monochromatic light in contiguous rows of the detector.

approximates the wavelength of key absorption bands due to $H_2O$ and OH in minerals, where a 1% depth absorption band is at the low end of mineralogic significance. The ''typical Martian material'' assumed is the reflectance spectrum of *Erard and Calvin* [1997] which is a medium-albedo material. For estimating SNR that material is assumed to be illuminated at 1.54 AU, observed at 30° phase angle (using the phase function from *Murchie et al.* [2000]), with a Martian surface temperature of 250 K (as per MRO Science Definition Team guidelines). For CRISM, these conditions represent an average target but an optimal viewing geometry. Lower albedo or unfavorable phase angle may lower measured radiance by 50–75%.

[158] SNR for the reference Martian scene was estimated using system responsivity (Figure 32) derived from observations of the Spectralon plate at <2500 nm and the large-aperture blackbody at >2000 nm. Both derivations agree closely in the wavelength range where they overlap. The noise includes effects of thermal background from a spectrometer housing at 191 K.

[159] Figure 33 shows the SNR expected for a full resolution targeted observation, given the observing conditions described above. SNR is >100 at nearly all wavelengths and >300 at 500–2500 nm, just exceeding the requirement of 400 at 2300 nm. Lower SNR at <450 nm and >2500 nm is a consequence of Mars's inherently low reflectance at those wavelengths. The lower SNR at ~650 nm that at surrounding wavelengths is due to a scattered light mask discussed in section 5.3.

[160] At most wavelengths SNR is shot-noise-limited. Thus, for lower-albedo targets or those observed at unfavorable lighting, the loss in SNR due to 50% lower radiance can be recovered (at the expense of spatial resolution) using onboard 2x spatial pixel binning.

### 5.3. Instrument Artifacts

[161] Like any spacecraft instrument, CRISM exhibits artifacts that require corrections beyond the basic radiance calibration. The seven most significant artifacts were found early enough during calibration either to be corrected or to be characterized sufficiently to be removed during post-processing.

[162] First, the boundary of zones 1 and 2 of the VNIR order sorting filter is a joint between two distinct glasses with different indices of refraction. When illuminated during stage 1 testing for linearity, it was found to cause significant ($\gg$10%) scattered light at shorter wavelengths (<670 nm). This was correcting by replacing the VNIR focal plane assembly with the flight spare, onto which a narrow black stripe was painted to shadow the joint. The black stripe attenuates the light from 610–710 nm and

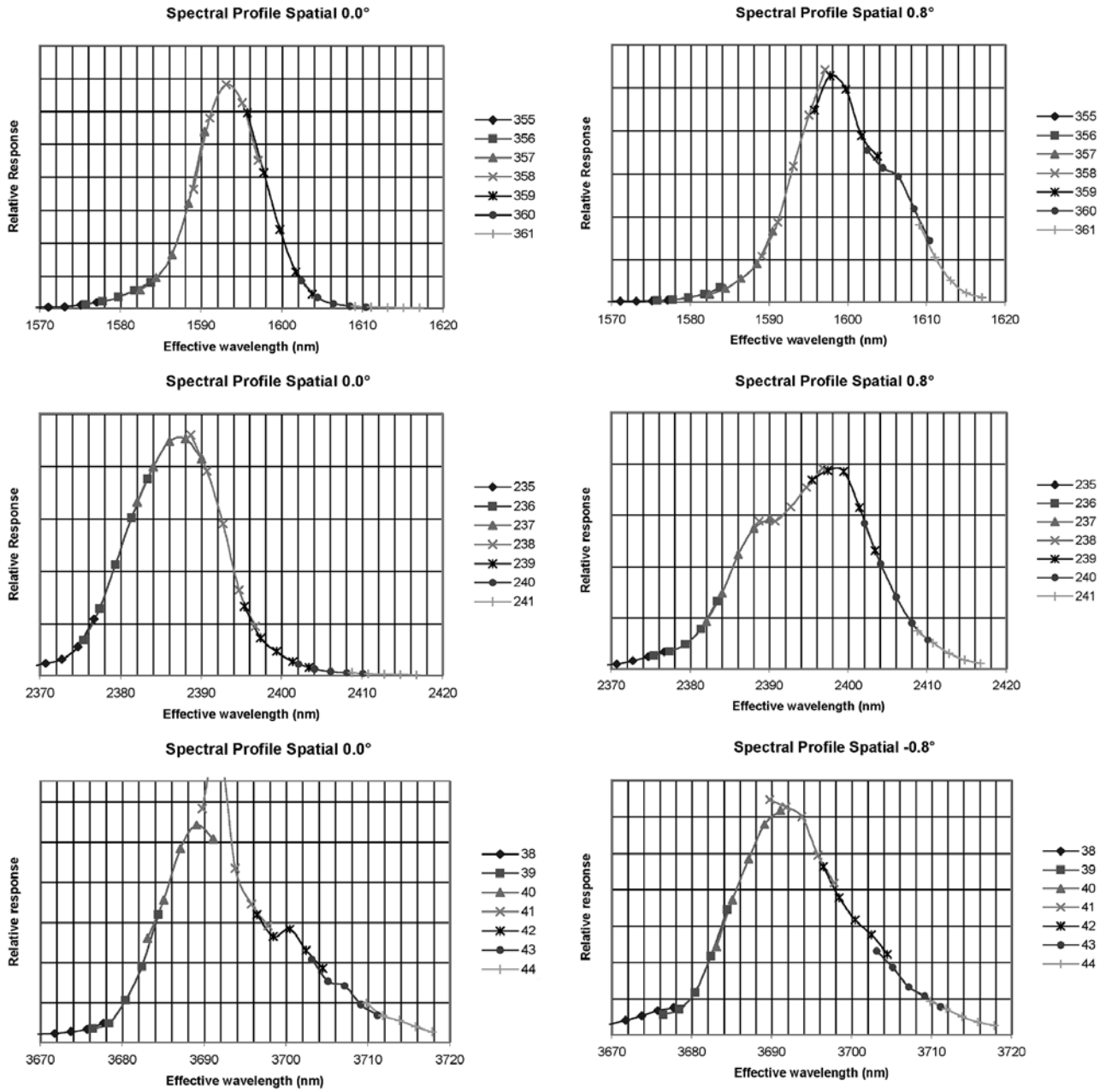


**Figure 31.** Spectral profiles at the center and short- and long-wavelength ends of the IR spectral range. Scale is the same as for comparable plots for the VNIR detector in Figure 30.

explains the dip in response at those wavelengths in Figures 32 and 33.

[163] Second, the linearity of both detectors was found to be extraordinarily sensitive to the bias voltage applied. Upon discovery of this during stage 1 testing, the voltage was modified from 5 to 4.8 V to lessen the effect. In hindsight, and if time had allowed, there should have been a study of several bias voltages near 4.8 V to identify the one producing the least nonlinearity.

[164] Third, CRISM's gimbal housing has a gap between two segments of its planet facing radiator, in order to simultaneously maintain the cooler bodies at >248°K and the optics at ~213°K. During ad hoc testing for scattered light during stage 2 (performed by walking a flashlight around the gimbal housing with a mounted but unaligned VNIR detector), a sneak path for undispersed light to the VNIR detector was discovered. This was easily fixed by covering the VNIR FPA with thermal blanketing, but the result was a heat leak from the FPA to the spectrometer housing, raising spectrometer housing temperature to near its maximum desired value of −75°C. To remediate the heat leak, VNIR operating temperature was modified from −20°C, intended originally, to −60°C.

[165] Fourth, the original "open" position for the shutter at step 0 of 33 was found to create a ghost image of the scene approximately 1° out of the FOV in the cross-slit

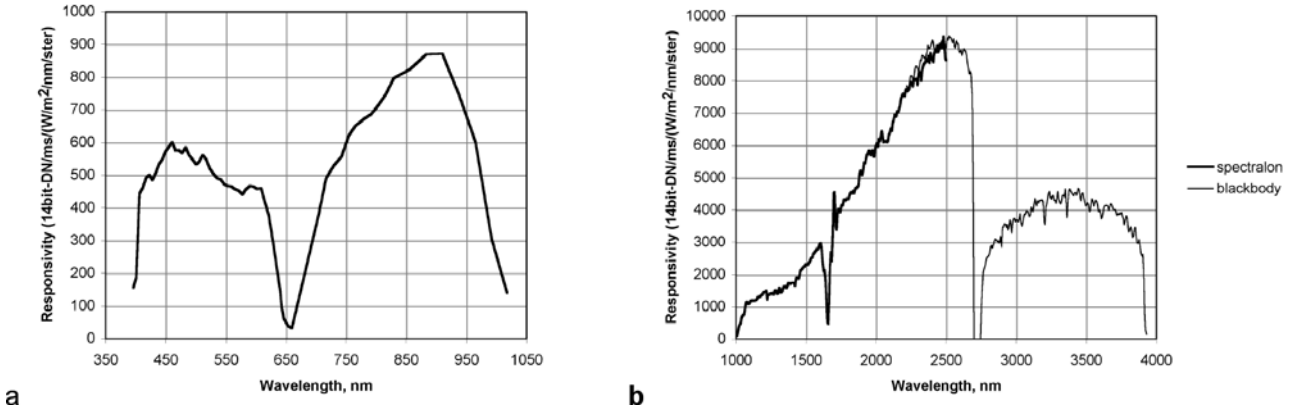


**Figure 32.** Preliminary estimates of system responsivity without spatial binning. (a) VNIR, derived using measurements of the spectralon plate. (b) IR, derived using the spectralon plate at shorter wavelengths, and a field-filling blackbody at longer wavelengths.

direction, with a magnitude ~10–30% of the primary scene. This was remediated by a software fix, in which "open" was redefined to position 3, which moves the origin of the ghost image to an angle further from the FOV at which it is baffled by the telescope. Secondary artifacts created by this fix are discussed in more detail in section 5.3.2.

[166] Fifth, zone 1 of the IR order sorting filter was found to have a red leak at >4200 nm, beyond CRISM's nominal wavelength range but within the spectral range at which the detector responds. Hence thermal background is unexpectedly large at 1000–1700 nm in the IR (Figure 18d, bottom). This was discovered too late for redesign of the filter; the main effect is decreased (but still high) SNR at the affected wavelengths (Figure 33b).

[167] Sixth, it was intended originally that the maximum wavelength would be 4050 nm (compared to MRO's requirement of ≥3600 nm) in order to cover the center of the strong carbonate band at 3980 nm. Due to tolerances in the manufacturing process, the peak response of the zone 3 linearly variable filter was mismatched from the peak required for 4050 nm light to fall on the detector. The mismatch was greater than the 80-nm band pass of the filter. To maintain responsivity at >2700 nm, a long-wavelength cutoff of 3920 nm was accepted to properly align the filter with light dispersed from the gratings.

[168] Finally, the spectrometer slit, which defines the mapping of wavelengths to detector rows as well as the spatial FOV, is mounted on a curved surface whose axis of curvature is parallel to the wavelength direction. The slit assembly is fixed with pins through holes whose diameters are oversized to provide margin for fastening the assembly. During instrument-level vibration testing between calibration stages 3 and 4, the slit assembly shifted in the wavelength direction by the tolerance in the hole diameters, shifting wavelength calibration by ~15 nm in both the VNIR and IR. Although vibration testing exceeded expected launch vibrations by ~50%, additional shifting of the slit assembly during launch cannot be ruled out. If it

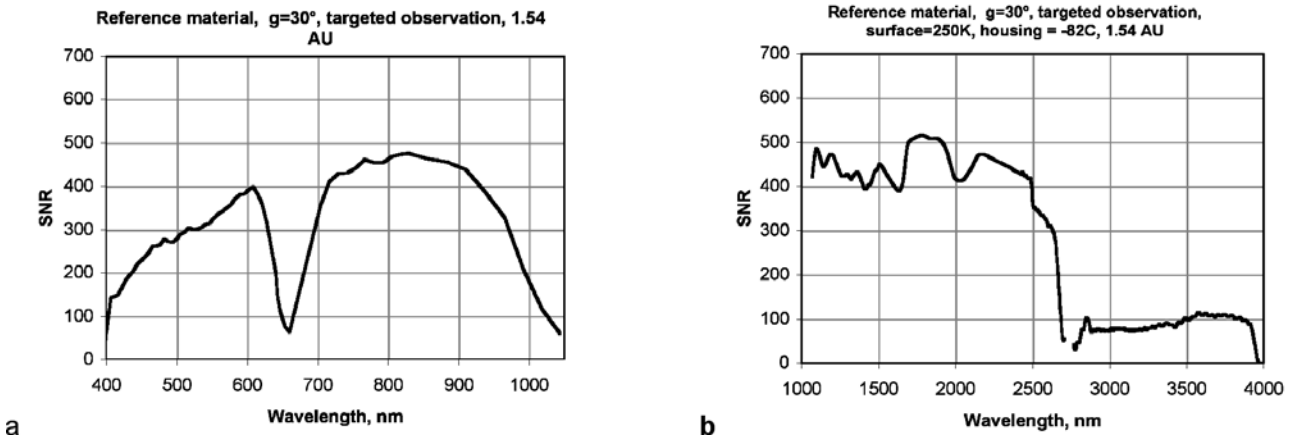


**Figure 33.** VNIR and IR SNR expected for a reference surface material expected during targeted observations without spatial binning. Frame rate is 3.75 Hz, with gimbal scanning to compensate for MRO motion, permitting up to 266 ms integration time. Actual integration times are 102 ms for the VNIR and 167 ms for the IR, to allow sufficient overhead to accommodate clouds without saturating.

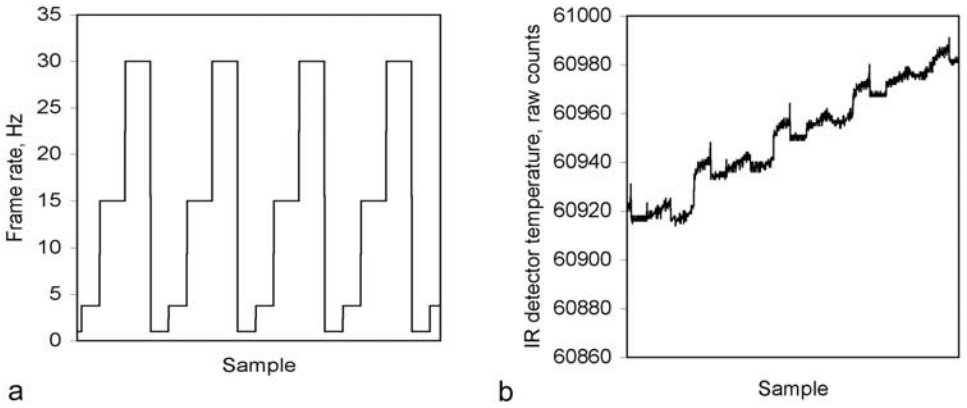


**Figure 34.** Effects of changing frame rate on uncalibrated, telemetered IR detector temperature 2. (a) Frame rate changes while bias was being measured as detector temperature slowly changed. (b) Uncalibrated IR detector temperature, which changed by 6°K during this portion of the test. There are ~10 counts per degree. Note the abrupt jumps of up to 1.5°K in apparent temperature when the frame rate changes.

occurred, it can easily be calibrated out using the measured positions of Martian atmospheric gas absorptions.

[169] All except one of remaining artifacts are relatively minor and/or have straightforward (though sometimes tedious) corrections, discussed below. The leak of second order light into the >2800 nm wavelength range of the IR detector is a major correction still under development.

#### 5.3.1. Electronics Effects

[170] Both responsivity and bias of the VNIR and IR detectors have to be corrected for small differences in detector temperature between measurements of scenes and measurements of internal calibration sources. The required detector temperature measurement precision is approximately 0.3°K (section 5.3.3). Relatively late during calibration, it was found that raw values of temperatures telemetered by the IR focal plane electronics (including both redundant detector temperatures) were being perturbed by up to 2°K by changes in current loads on the board. These variations in current result from normal operations like changing frame rate, running lamps, or running a cooler (e.g., Figure 34). The large number of ground calibration frames afforded many cases in which loads changed while temperature remained constant, and these cases occurred over temperatures that span the operating range, allowing derivation of the correction of telemetry values at each frame rate to their corresponding values at 1 Hz.

[171] Both detectors, but especially the VNIR detector, is subject to a weak ghost image of any illuminated spot into its corresponding location in every other quadrant of the detector (Figure 35). The cause is suspected to be that all four quadrants share a common ground through which electrical cross-talk occurs. This is a small effect at the <1% level, and in practice is removed by scaling the image of each quadrant by an empirically determined value that is nonlinearly related to signal level, and then subtracting the scaled quadrant image from that of every other quadrant. To the uncertainties in measurement, each of the four quadrants in a detector behaves only slightly differently. There is a minimal effect of frame rate, but ghost magnitude is apparently unaffected by detector temperature.

[172] As mentioned previously, both detectors exhibit slightly nonlinear response to input signal. This was characterized during stage 1 testing by a matrix of measurements at each frame rate, in which both the level of a well-calibrated light source and exposure time were varied. Both types of modulation of total signal produce indistinguishable results (Figure 36). This testing has been repeated in flight by imaging a focal plane lamp at multiple exposure times at each frame rate. Nonlinearity is well described by a logarithmic function of bias- and ghost-corrected DN; corrections for flight data scale DN level by the ratio of relative responsivity at that DN to the responsivity at a reference DN level. It is critical that bias and ghost corrections be performed prior to this correction, to eliminate negative values due to interquadrant ghosting.

[173] At higher frame rates (15 and 30 Hz), the detector-averaged behavior described above appears inadequate to fully characterize nonlinearity, and individual pixels exhibit slight variations. To test for pixel dependence of nonlinearity, uniformly illuminated frames at different DN levels were obtained and bias-corrected. Then frames with lower DN levels were ratioed to those with a high DN level of

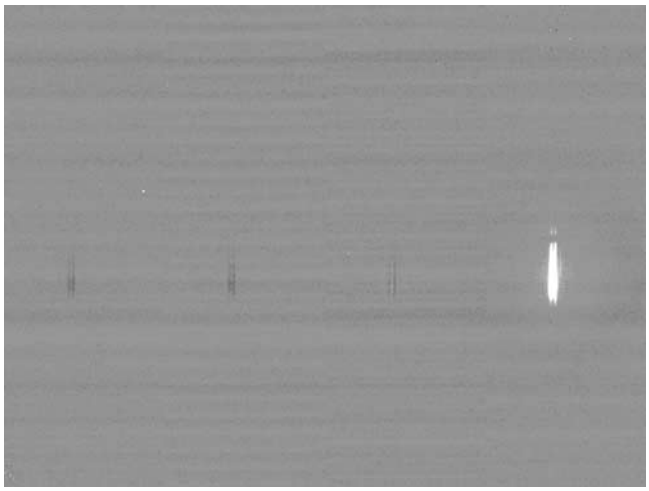

**Figure 35.** Raw, contrast-enhanced VNIR frame showing a dispersed image of a lamp filament in quadrant 4. There are weak, negative images of the filament at the corresponding locations in quadrants 1–3.

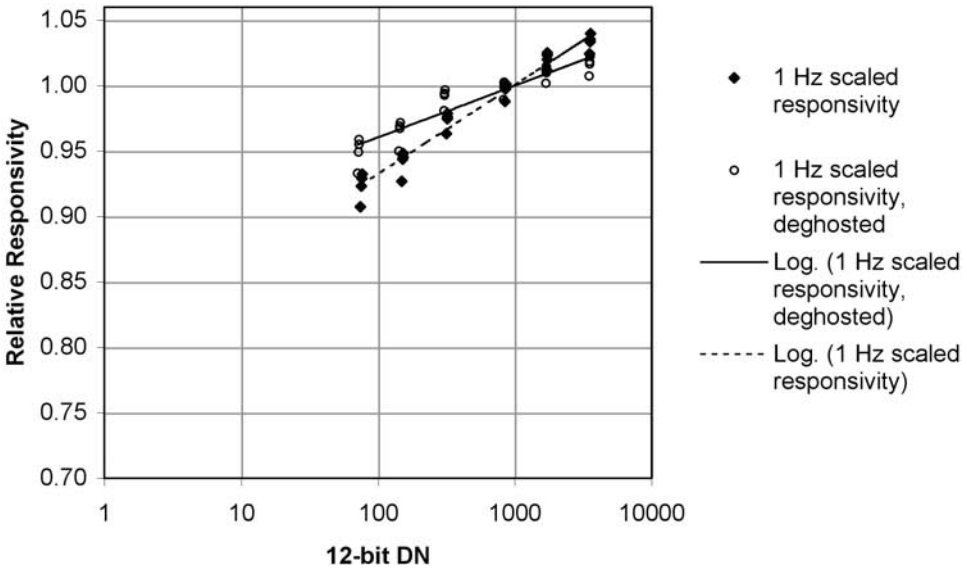


**Figure 36.** Response of the VNIR detector to a calibrated light source relative to its response at a reference DN level. Detector nonlinearity is fit to acceptable accuracy as a function of the log of bias- and ghost-corrected DN level.

approximately 8000 14-bit DNs (80% of full well); this procedure was repeated for each frame rate. Figure 37a shows a low- to high-DN ratio image obtained at 1 Hz. The spatial standard deviation in the ratio image is consistent with the level expected purely from noise in the data due to photon-counting statistics. The same is true at 3.75 Hz. Figure 37b shows a comparable ratio image obtained at 30 Hz, using the same stretch. The spatial standard deviation is higher than can be explained by noise alone, and in ratios with different brightnesses in the numerator, specific pixels are consistently dark or bright. Similar but lesser pixel-to-pixel nonuniformity is also observed at 15 Hz. This excessive pixel-to-pixel variation is being attributed by our team to pixel-dependent nonlinearity.

[174] This feature of the detectors will be corrected in flight as described in section 5.4.2.

### 5.3.2. Optical Effects

#### 5.3.2.1. Shutter Reproducibility

[175] In order to illuminate the spectrometer slit's full 2.12° FOV, CRISM's telescope illuminates a circular region of slightly larger diameter surrounding the slit. The base of the shutter, on the hinge end, just protrudes into the illuminated area. At position 0, originally intended as the "open" position, the reflective rear surface of the shutter provides the detectors an unbaffled view of the scene approximately 1° from the center of the FOV in a cross-slit direction, creating an out-of-focus "ghost" image of that location (Figure 38a, left). Moving the shutter through successive steps redirects the angle from which the ghost image originates to further from the center of the FOV (Figure 38a, center). At position 3, the angle from which the ghost image originates is baffled by the telescope, and the

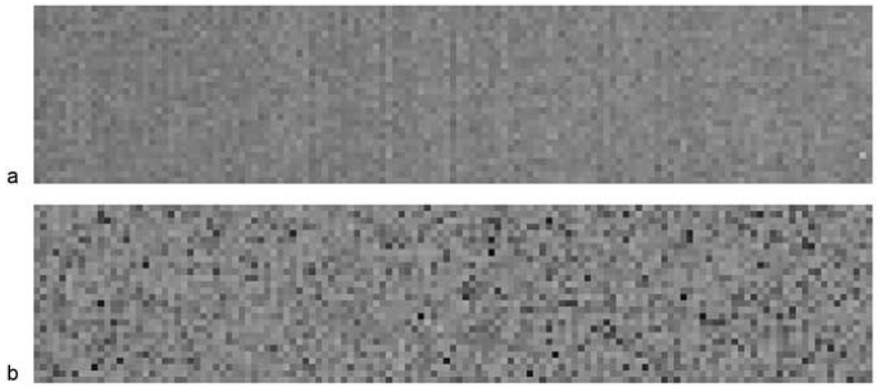


**Figure 37.** (a) Ratio of bias-subtracted VNIR images acquired during detector-level testing at different levels of nearly uniform illumination at a 1 Hz frame rate. The brighter image is in the denominator. Both the numerator and denominator images were divided by their mean values. Contrast stretch is 0.95–1.05. The graininess of the image can be attributed to noise in the data. (b) Same for 30 Hz; there is more graininess than can be attributed to noise.

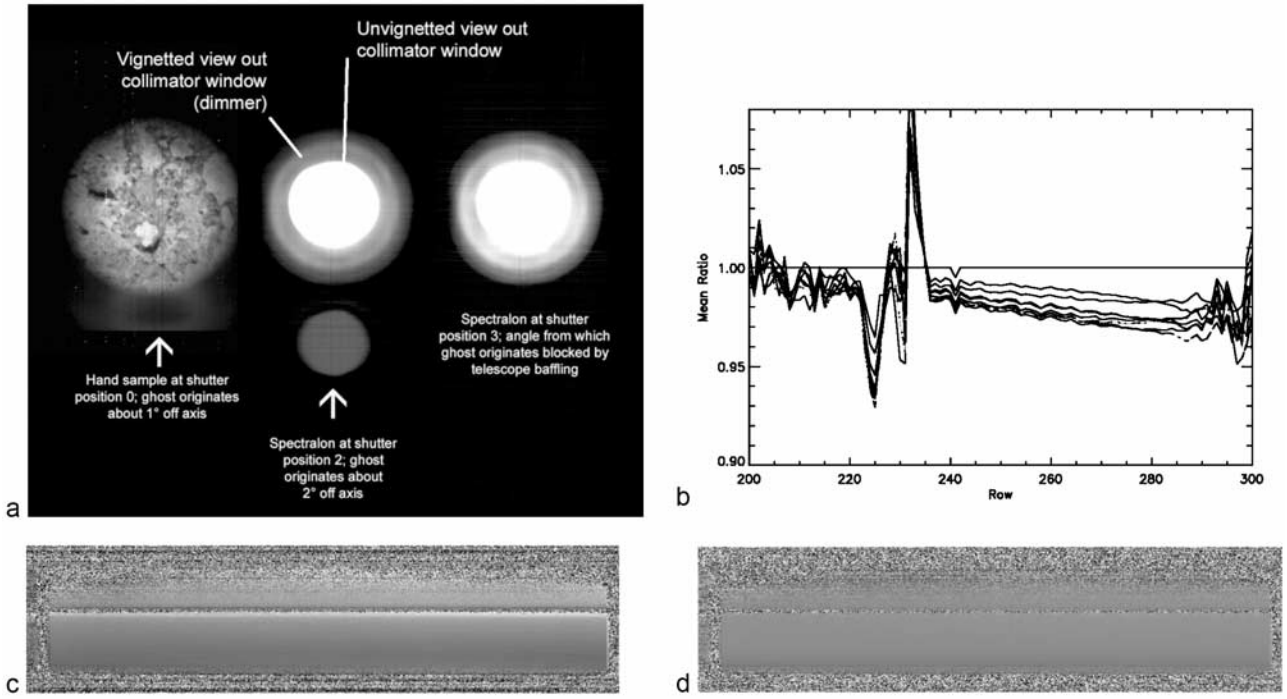


**Figure 38.** (a) Composite of three targets imaged at the focus of the OCF collimator, with the shutter in positions 0, 2, and 3. The left panel, a geologic hand sample imaged at the beginning of stage 3 testing, is the observation in which the shutter ghost image was discovered. (b) Plot of the row-averaged ratios of nine successive VNIR sphere observations to an initial observation. The shutter was moved between the observations. (c) Ratio of uncorrected VNIR sphere observations, showing only the detector rows returned by the wavelength filter. Scale of the stretch is 0.9–1.1. (d) Identically contrast-enhanced ratio of the same observations after a preliminary correction for shutter position irreproducibility. The slightly dark band at the bottom is due to variation in detector temperature, which affects photosensitivity at >900 nm.

ghost disappears (Figure 38a, right). To remediate the ghost image, the open position of the shutter was redefined in software to position 3.

[176] At position 3 the shutter attenuates up to 10% of the light coming from an external scene, depending on the wavelength. The short-wavelength zone of the VNIR grating and the long-wavelength zone of the IR grating are blocked preferentially.

[177] In frames that view the integrating sphere, ratioing successive views of the sphere (between which the shutter is moved) creates a distinctive wavelength-dependent pattern in which brightness of the sphere is non-repeatable by up to a few percent (Figure 38b). This is explained by a small ($\sim$0.1°) non-reproducibility in the angle at which the sphere is viewed and the fact that, unlike the external scene, the spectrometer's view of the sphere is vignetted by the sphere's aperture. With a slight shift in shutter position, the cone of sphere light entering spectrometer optics shifts. The filling of dual zone gratings changes slightly, decreasing responsivity at long VNIR wavelengths and short IR wavelengths. Also, the shadow of the black strip on the VNIR order-sorting filter zone boundary shifts, creating a distinctive trough and peak pattern at detector rows 222–235 (approximately 605–690 nm).

[178] Because this effect is so characteristic as a function of wavelength, it is easily correctable. Ratios of different sphere observations during ground calibration are used to create a multiplicative correction to a sphere image as a function of wavelength. For in flight data to be corrected, the magnitude of the peak near VNIR row 235 is measured. The correction is scaled by the magnitude of the peak, and it is multiplied by the data. The VNIR row 235 peak is used to scale the corrections for both the VNIR and IR. Figure 38c shows the ratio of two uncorrected frames viewing the sphere; note the bright stripe (near row 235) and the darkening at lower rows (long wavelengths). Figure 38d shows the same ratio after the frames after a preliminary version of the correction was applied; the effect of change in shutter position is essentially gone.

[179] To the limits of measurement error, the small irreproducibility of shutter position at the "open" position has no measurable effect on external scene data.

#### 5.3.2.2. IR Second Order Leakage

[180] During stage 3 calibration in the OCF, monochromatic light was scanned in a grid of wavelength and along-slit spatial position to search for out-of-band light. Out of band leakage was found in zone 3 of the IR order sorting filter. The filter admits up to 3% of the 2nd order light from the grating, at wavelengths 1400–1950 nm, that falls at detector rows whose nominal wavelengths are 2800–3900 nm (Figure 39a). The leakage peaks at a nominal wavelength of 3400 nm. Due to the falloff of both the solar spectrum and the Martian reflectance spectrum with increasing wavelength, the relative magnitude of the leakage to the signal in zone 3 is enhanced so that it becomes tens of

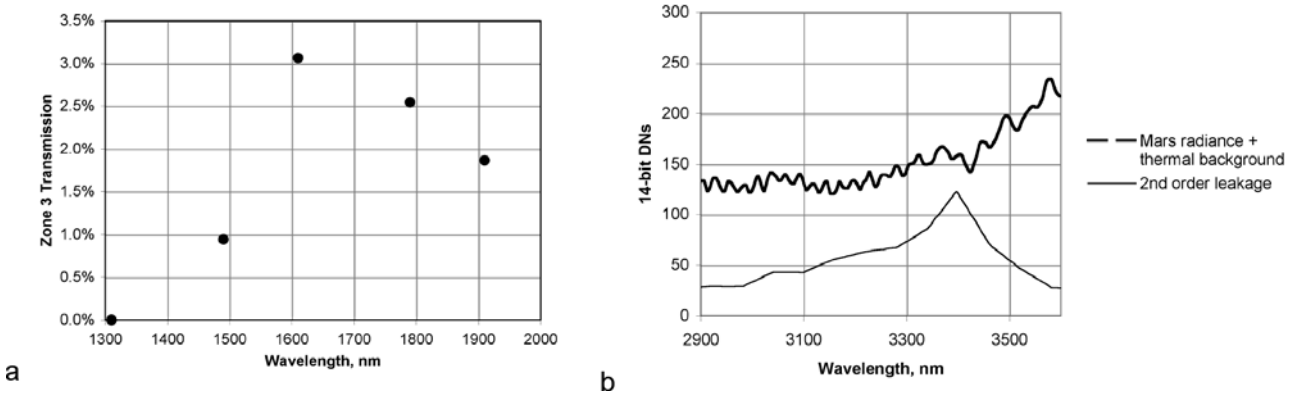


**Figure 39.** (a) Percent of second order light admitted through zone 3 of the IR order sorting filter. (b) Estimated magnitude of the leakage relative to nominal signal, including effects of the solar spectrum and Martian reflectance spectrum.

percent of the total signal in that wavelength range (Figure 39b).

[181] The OCF testing provided sufficient data for an empirical correction for this effect, in which scaled values of signal at second-order wavelengths are subtracted from first-order (nominal) wavelengths. The correction is still under development so its accuracy and the magnitude of the expected residuals are unknown. This correction is discussed in more detail in section 5.4.2.

### 5.3.3. Temperature Effects

#### 5.3.3.1. Bad Pixels

[182] The IR detector is operated at cryogenic temperature to minimize dark current and bias level of the detector. With increasing detector temperature, not all pixels accrue an elevated bias level or dark current (the latter of which adds noise due to its electron counting statistics) at the same rate. The most susceptible pixels, within which effective SNR or available dynamic range are adversely impacted, are "bad pixels." Figure 40 shows the relationship between detector temperature and the fraction of pixels whose elevated bias or dark current significantly limits dynamic range (Figure 40a), or whose dark current introduces noise that is unremovable even after subtraction of the measured background (Figure 40b).

[183] The algorithm for flagging bad pixels and their treatment in the calibration pipeline is discussed in detail in section 5.4.2.

#### 5.3.3.2. Bias Levels

[184] Bias is the response of the detector to zero input signal from light or thermal background, and includes two components. At operating temperatures of −60°C, VNIR dark frames (Figures 18a–18c) measure only bias and are highly illustrative. One component is a fixed pattern that varies pixel-to-pixel ±25 14-bit DNs, and has a weak columnar organization. The second component is a step function of about 20 14-bit-DNs that occurs at some row of the detector. The row at which this occurs moves systematically with frame integration time.

[185] The fixed-pattern component of bias depends on frame rate, differing by ~100 14-bit DNs between frame rates. It also varies with detector temperature (Figure 41a), and temperature of the focal plane electronics (Figure 41b). To the limits of measurement uncertainty, the temperature dependence itself is independent of quadrant or frame rate.

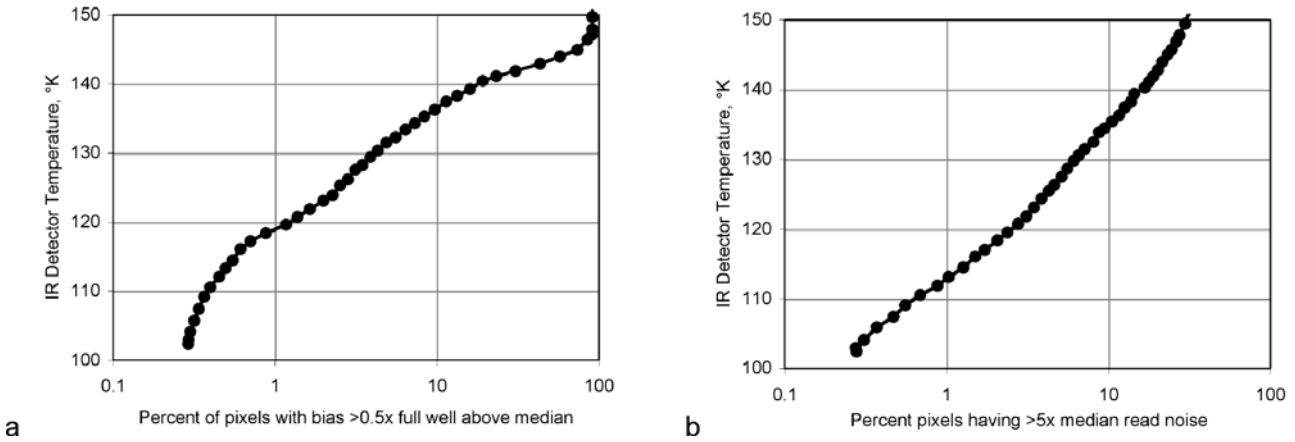


**Figure 40.** Percentage of IR pixels with characteristics qualifying them as "bad," as a function of IR detector temperature. (a) Pixels with bias sufficiently elevated to significantly erode available dynamic range. (b) Pixels with sufficient dark current noise to significantly erode effective SNR.

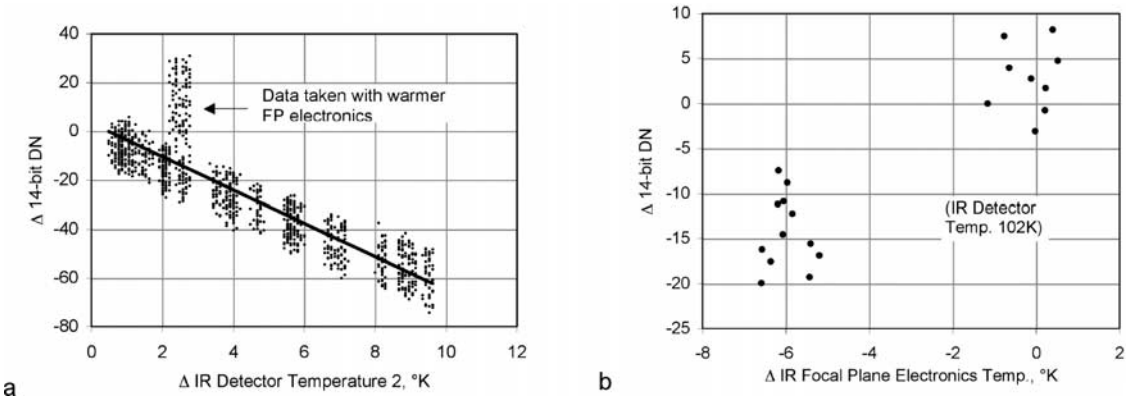


**Figure 41.** (a) Change in IR detector-averaged bias as a function of detector temperature. (b) Change in IR detector-averaged bias as a function of focal plane electronics temperature.

[186] In flight, the fixed pattern to the bias will be measured via dedicated calibrations discussed in section 5.4.1, and will be adjusted for changes in detector or focal plane electronics temperature based on telemetered temperatures. The step function will be modeled.

#### 5.3.3.3. Sphere Radiance

[187] Under closed-loop control, the brightness of either of the integrating sphere's lamps is measured by a Si photodiode that adjusts current up or down to reach a commandable brightness goal. The responsivity of the Si in the photodiode is affected by temperature at >900 nm, becoming more sensitive to light at warmer temperatures. So, as sphere temperature increases and the Si becomes more photosensitive, the same commanded goal requires less lamp current. The decrease in lamp current (and brightness) with increasing sphere temperature is shown in Figure 42. In flight, sphere radiance is modeled on the basis of ground calibration at different operating temperatures, which were measured by comparing against stable external sources (the Spectralon plate and blackbody). Output radiance at the commanded brightness goal is calculated at every pixel of each detector as a function of telemetered sphere temperature; there is a separate model for each sphere bulb.

#### 5.3.3.4. Detector Responsivity

[188] Both the VNIR and IR detectors exhibit dependence of their spectral responsivities on detector temperature. In the VNIR detector, the ±1°K thermostatic cycling of the detector heater on the timescale of minutes affects responsivity at >900 nm by up to a few percent, due to the temperature dependence of Si photosensitivity at those wavelengths. This is evident in the upward and downward curvature of the relative response to the internal sphere measured at different points during the temperature cycle (Figure 38b, at detector rows >275; Figure 39d, dark band at bottom). In flight, differences in responsivity on such very short timescales will be corrected using a function of telemetered detector temperature, derived from VNIR ground measurements of a stable reference (the Spectralon plate) taken as detector temperature cycled.

[189] In the IR detector, the longest wavelengths (especially zone 3) exhibit a cyclical pattern of responsivity variation as a function of wavelength. The pattern is interpreted as Fabry-Perot fringes due to interference by long-wavelength light that penetrates the HgCdTe detector material which, at those wavelengths, is only a few wavelengths thick. The pattern shifts systematically as a function of detector temperature (Figure 43a) due to thermal expansion of the detector material. If otherwise identical image frames taken at different detector temperatures are ratioed, shifting of the fringes creates artifacts at the ~5% level (Figures 43b and 43c). The change in temperature required to introduce these artifacts at the level of anticipated noise in the data is near 0.25°K, and IR detector temperature is predicted to vary by ~1°K in the course of one Mars orbit. To correct for this, the sphere will be measured repeatedly as detector temperature changes, and the sphere used as a relatively stable reference against which to calibrate out these effects.

### 5.4. Data Calibration Pipeline

#### 5.4.1. Flight and Ground Calibration Data

[190] All calibration matrices are stored in "calibration data records" or CDRs, separate from the main algorithm coded in software. There are two general classes of calibration matrices, those derived from ground data and updated infrequently if at all, and those that represent highly time-variable properties of the instrument. Examples of the

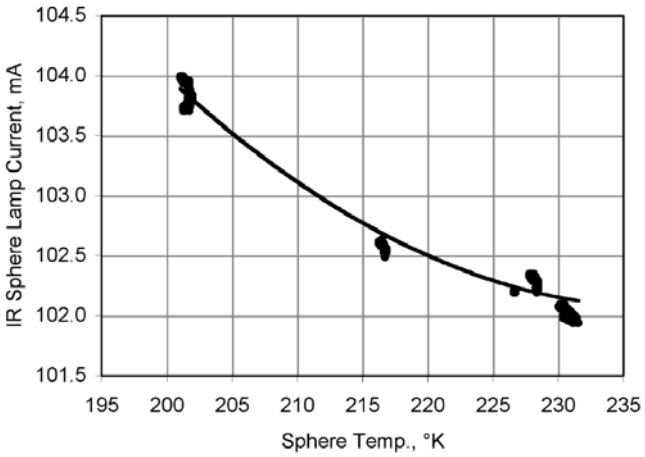


**Figure 42.** Relationship of current of the IR-controlled sphere lamp to sphere temperature, for a commanded closed-loop brightness goal of 1400 (corresponding to ~90% of full power to the sphere).

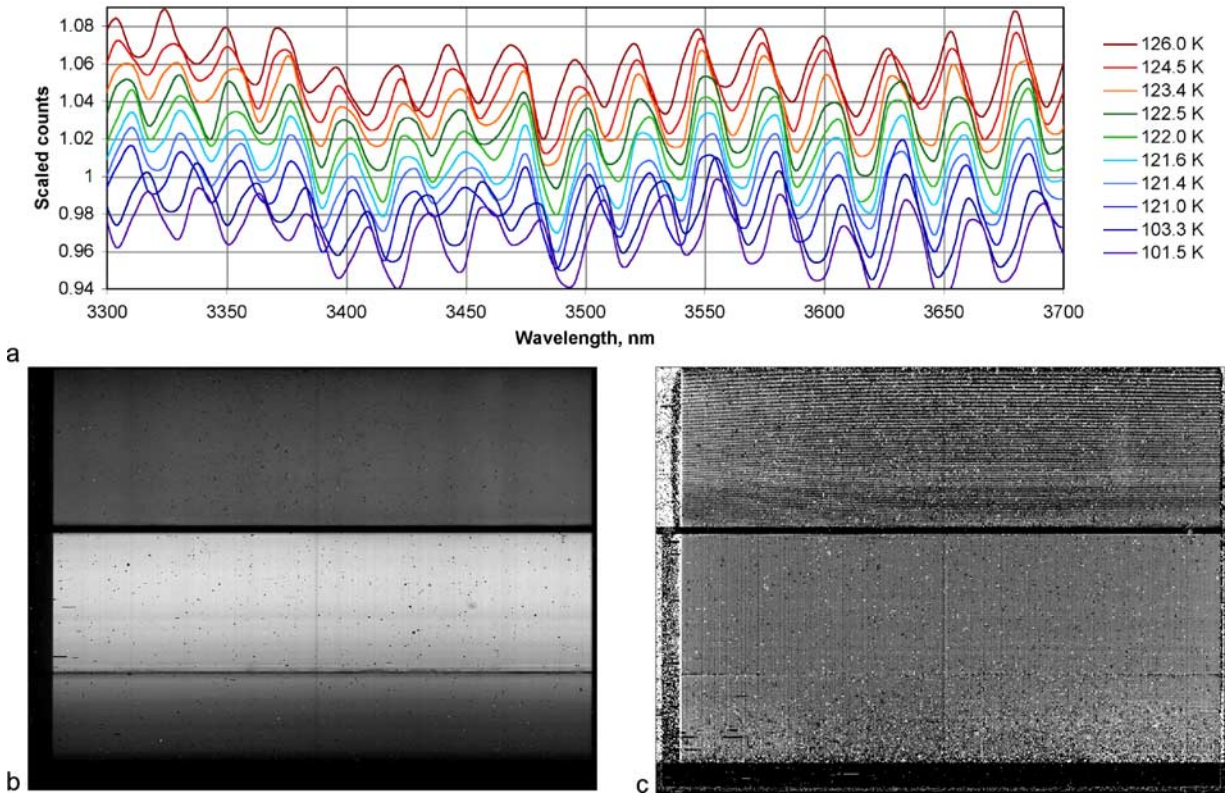


**Figure 43.** (a) Plot of scaled signal level in part of zone 3 of the IR detector, viewing the internal integrating sphere while detector temperature changes. The plot for each detector temperature is offset for clarity. (b) Background-subtracted IR image from viewing the internal integrating sphere. (c) Ratio of two such image frames taken at different IR detector temperatures, with contrast enhanced 20x. One can see curved bright and dark bands in Zone 3 (at top).

former include the constants needed to uncompress data, correct non-linearity, or correct bias for effects of detector or focal plane electronics temperature. Examples of the latter include bias and IR thermal background, which depend on detector and spectrometer housing temperature, respectively.

[191] There are two formats for storing the values in the matrices, distinguished by the levels of processing from the original data that follow standards of the Committee On Data Management And Computation [*Hall et al.*, 2005]. Level 6 CDRs, or CDR6s (Table 6), are tabulated numbers

**Table 6.** Description of CRISM Level 6 Calibration Data Records, CDR6s

| Products | Acronym |
|---|---|
| *Ground Calibration Products* | |
| Coefficients for correcting raw housekeeping for effects of lamps, coolers, frame rate | HD |
| Coefficients for calibrating housekeeping from digital to physical units | HK |
| Gain and offset to use for each row for 12 to 14 bit conversion; 12 to 8 bit lookup tables used for each row | PP |
| Wavelength tables | WV |
| 12 to 8 bit lookup tables | LK |
| 8 to 12 bit lookup tables (inverse of 12 to 8) | LI |
| Linearity correction | LC |
| Additive correction of bias to nominal detector operating temperature | DB |
| Additive correction of bias to nominal focal plane electronics operating temperature | EB |
| Interquadrant ghost removal scaling factors | GH |
| Bias step function | BS |
| Average Mars spectrum | AS |
| *Flight Calibration Products* | |
| Housekeeping status packets, one day per file | ST |
| *Engineering, Planning, and Data Validation Products* | |
| Uploaded values of alarm limits and instrument control parameters, raw and calibrated forms | DR, DC |
| Engineering-related software settings, raw and calibrated forms | SR, SC |
| Model of data compressibility in different instrument configurations | CP |
| Event log of key spacecraft and instrument activities | EL |

**Table 7.** Description of CRISM Level 4 CDRs

| Products | Acronym |
|---|---|
| *Ground Calibration Products* | |
| Wavelength image (each pixel) determined on ground | WA |
| Spectral band pass, or full width half maximum (each pixel) determined on ground | SB |
| Solar flux at 1 AU (for each pixel to take into account spectral smile effects) | SF |
| Focal plane lamp to external flat ratio images: VNIR and IR ratio images of each lamp to external flat reference | RA |
| Masks of detector dark columns, scattered light columns, scene columns | DM |
| Matrices to remove estimated leaked higher order light | LL |
| Sphere spectral radiance at set point (pixel by pixel coefficients to a polynomial function of optical bench temperature) | SS |
| Shutter position reproducibility correction to sphere radiance (pixel by pixel coefficients to a linear function of the ratio of corrected sphere image to sphere spectral radiance model) | SH |
| Temperature dependence of detector responsivity (pixel by pixel coefficients to a polynomial function of detector temperature) | TD |
| Along-slit angle measured from slit center at 2300 nm | CM |
| *Flight Calibration Products* | |
| Bad pixel mask: time-tagged map of bad pixels | BP |
| Bias file: time-tagged, fitted VNIR and IR images | BI |
| Background file: time-tagged, bias- and ghost-subtracted, linearized, averaged IR background frames | BK |
| Noise file: time-tagged, image of pixel-by-pixel uncertainties in short-exposure images used to calculate bias | UB |
| Nonuniformity file: time-tagged flat-field correction | NU |
| Processed sphere image in units of DN/ms | SP |

in ASCII format, and level 4 CDRs, or CDR4s (Table 7), are images each derived from a collection of flight or ground calibration measurements.

[192] Calibration matrices that are highly time variable will be measured in flight and include the following:

[193] 1. For the VNIR detector bias is measured directly, with the shutter closed and at the same integration time as accompanying measurements of Mars. For the IR, shutter-closed measurements also include thermal background. The bias is therefore measured for the IR detector by taking data at several integration times and extrapolating to zero exposure. The step function is modeled deterministically using integration time. Currently, the default is to take a VNIR bias measurement with every observation and IR bias observations several times daily.

[194] Masks of bad pixels, whose occurrence depends on detector temperature, will be created in concert with bias images. The derivation of bad pixel masks is described in section 5.4.2.

[195] 2. IR thermal background is the response of the IR detector to "glow" of the inside of the instrument predominantly at >2300 nm. The change in spectrometer housing temperature that perturbs thermal background by the equivalent to read noise is $\sim$0.02°K, whereas the spectrometer housing is predicted to change by several degrees over the course of an orbit. Therefore shutter-closed IR measurements will be taken interspersed within all observations, at an interval of approximately once per 3 minutes. To correct any given frame of scene data, bracketing shutter-closed measurements are interpolated in time.

[196] 3. The onboard integrating sphere serves as the radiance reference against which CRISM's radiometric responsivity as a system is pegged. The frequency of its measurement is driven by the timescales of change of instrument characteristics which must be calibrated out using the sphere. The most rapidly varying radiometric characteristic is responsivity of the VNIR detector at its longer wavelengths, which changes by the equivalent of noise in the data in tens of seconds due to the thermostatic cycling of VNIR detector temperature. Measuring the sphere this frequently is impractical, so this effect is corrected instead using telemetered temperature of the VNIR detector and ground calibration results. The next most rapidly changing characteristic is IR detector responsivity at its longest wavelengths, which is also a function of temperature (Figure 43). Currently, the default to calibrate this effect is to take sphere observations on day- and night-side segments of several orbits per day, each observation consisting of illuminated images with the sphere lamp under closed-loop control, and unilluminated images to measure the sphere's blackbody background (which must be subtracted out).

[197] 4. Pixel-to-pixel variations in VNIR detector responsivity are measured monthly using bland regions of Mars, as described in section 5.4.2.

### 5.4.2. Radiometric Calibration

[198] Radiometric calibration to units of radiance involves uncompressing data, correcting instrument artifacts, subtracting bias and background, dividing by exposure time, and converting of the result of these steps to units of radiance by comparing against a radiometric reference. This approach explicitly uses measurements of the internal integrating sphere. The general equation to reduce measurements of Mars to units of radiance, using ground and flight calibration measurements, is

$$\mathrm{RD}_{x,\lambda} = \mathrm{M}_{x,\lambda,\mathrm{Hz}}\big((\mathrm{K}_{x,\lambda,\mathrm{Hz}}\big(\mathrm{D14}_{\lambda}\big(\mathrm{DN}_{x,\lambda,\mathrm{TV,TW,TI,TJ,T2,Hz,t}}\big) - \mathrm{BiaT}_{x,\lambda,\mathrm{TV,TW,TI,TJ,Hz,t}}\big)/\mathrm{t} - \mathrm{Bkgd}_{x,\lambda,\mathrm{TI,T2,Hz}} - \mathrm{Scat}_{x,\lambda,\mathrm{TV,TI,T2,Hz}}\big)/\mathrm{RST}_{x,\lambda,\mathrm{TV,TI,T2,T3,S}}\big)$$

[199] Subscripts define the variables on which calibration coefficients depend and include the following:

- x spatial position in a row on the focal plane, in detector elements;
- $\lambda$ position in the spectral direction on the focal plane, in detector elements;

Hz frame rate; implicitly includes with it compression configuration including wavelength table and binning mode;
$T_I$ IR detector temperature in °K;
$T_V$ VNIR detector temperature in °K;
$T_2$ spectrometer housing temperature in °K;
$T_3$ temperature of the integrating sphere in °K;
$T_J$ IR focal plane board temperature in °K;
$T_W$ VNIR focal plane board temperature in °K;
t integration time in seconds;
s choice of sphere bulb, side 1 (controlled by IR focal plane electronics) or side 2 (controlled by VNIR focal plane electronics).

[200] All of the input temperatures come from instrument housekeeping, and are monitored by the focal plane electronics. Temperatures are corrected for electronics noise (e.g., Figure 34) by substituting for temperatures, currents, and voltages in the image headers the corresponding values at the same spacecraft time from the low-speed telemetry stored in "ST" CDR6s. This step is performed because the low-speed telemetry maintains a fixed timing relative to instrument current variations on 1-second cycles, whereas the image headers do not; this makes the electronics noise more easily calibrated in the low-speed telemetry. The raw digital values are corrected for effects of frame rate and variable current loads, including lamps and coolers, using additive and multiplicative coefficients maintained in the "HD" CDR6, and then scaled to physical units using other coefficients maintained in the "HK" CDR6.

[201] The terms in the equation and their sequential application are as follows.

#### 5.4.2.1. Data Decompression

[202] D14$\lambda$ converts from raw 8- or 12-bit DNs to 14-bit DNs. This is accomplished by inverting the 12-to-8-bit LUT using the "LI" CDR6, then dividing by the gain and adding the offset used on board, whose values are contained in the "PP" CDR6.

#### 5.4.2.2. Bias Subtraction

[203] $BiaT_{x,\lambda,TV,TW,TI,TJ,Hz,t}$ is detector bias derived as described above from flight measurements, and stored as a "BI" CDR4. For the VNIR, it is just a decompressed shutter-closed measurement. For the IR, it is the zero-exposure intercept of the pixel-by-pixel fit of 14-bit DN to exposure time in the bias measurements, added to the bias step function stored in the "BS" CDR6.

[204] Bias is corrected for changes in focal plane electronics and detector temperature since the time of bias measurement, using telemetered detector and electronics temperature and the "DB" and "EB" CDR6s, respectively.

#### 5.4.2.3. Electronics Artifacts Correction

[205] $K_{x,\lambda,Hz}$ applies the bad pixel, detector ghost, and detector nonlinearity corrections. This is actually a composite of four distinct steps.

[206] The bad pixel mask, stored as a "BP" CDR4, is constructed from a bias measurement. Two distinct types of pixels are flagged, noisy pixels and pixels with elevated bias; once data are units of radiance bad pixels are interpolated across bilinearly. Noisy pixels are defined as those whose noise level significantly degrades the effective SNR of the calibrated data. Thresholds for flagging detector elements as "noisy" are stored in the "AS" CDR6. The noise is calculated from the standard deviation of pixel DN levels between different frames in the short-exposure bias measurement, and stored in a "UB" CDR4. The noise for each pixel is compared to the threshold in the "AS" product and if the value is larger, the pixel is declared bad.

[207] Pixels with elevated bias are treated in a wavelength-dependent fashion, such that they are flagged if their bias is sufficiently high that a bright scene would cause them to saturate. (This is done instead of just examining scene data and looking for saturation, because when pixels are binned spatially, saturation of one of the component pixels is not obvious.) The "AS" CDR6 also contains 14-bit saturation limits, and limiting 14-bit scene DNs for different combinations of frame rates and exposure times corresponding to sphere observations and targeted and multispectral observations of Mars. For each pixel, bias from the "BI" product is added to the expected 14-bit DN from the "AS" product, and if the saturation limit is crossed, the pixel is declared bad.

[208] The correction for detector ghosts subtracts the scaled, bias-removed DN from each quadrant from every other quadrant of the detector. Scaling coefficients are stored in the "GH" CDR6.

[209] The nonlinearity correction scales bias- and ghost-removed DN to account for nonlinearity in detector response. Detector-averaged scaling coefficients are stored in the "LI" CDR6.

[210] Pixel-dependent nonlinearity at higher frame rates can be corrected using one of two methods. The primary method is to use the onboard integrating sphere for IR data, and bland regions of Mars for VNIR data. (The sphere is comparable in brightness to Mars in the IR, but much dimmer in the VNIR.) For IR data, pixel-to-pixel effects are fully corrected by imaging the sphere at the same frame rate. For the VNIR a non-uniformity matrix, or flat-field, the ("NU") CDR4, is constructed from images of bland regions of Mars having average albedo and illumination. The general procedure, which was also used to construct flat-fields for the Clementine HIRES camera, was described by *Robinson et al.* [2003]. Several thousand frames of different scenes along-track are averaged to remove effects of non-uniform illumination of the surface due to topography, and the spatial image at each wavelength is normalized by its mean value. The non-uniformity correction is used with VNIR sphere or scene images processed to this point.

[211] A backup approach is to use the focal plane lamps, along with a ratio image of lamp illumination to an external flat field (stored in the "RA" CDR4). This approach is less desirable due to the spatial non-uniformity of focal plane lamp illumination of the detector (Figure 19).

#### 5.4.2.4. Background Subtraction

[212] $Bkgd_{x,\lambda,TI,T2,Hz}$ is a "BK" CDR4 constructed by applying the D14, BiaT, and K corrections to a shutter-closed IR measurement interspersed with Mars measurements. The actual background subtracted from a scene measurement is a time-weighted average of preceding and subsequent "BK" shutter-closed measurements, to allow for the continuous variation of IR thermal background as spectrometer housing temperature changes.

#### 5.4.2.5. Scattered Light Subtraction

[213] $Scat_{x,\lambda,TV,TI,T2,Hz}$ is the stray light subtraction, and includes two components. The first component is glare from

the gratings, which produces a low level of light at a distance of tens or more of pixels from a source (e.g., Figure 29). This component of scattered light is measured directly at each row of the detector as the mean level in the scattered light columns at a given row (Figure 26). The locations of the scattered light and scene pixels are stored in the ''DM'' CDR4.

[214] The second component of scattered light is the second-order light leaked through zone 3 of the IR order sorting filter (Figure 39). This is removed by scaling and subtracting the measured signal at second order wavelengths from the measured first-order signal in zone 3. For each detector row (wavelength), which second-order rows to use and their weightings are stored in the ''LL'' CDR4.

#### 5.4.2.6. Responsivity Correction Using Sphere Data

[215] $RST_{x,\lambda,TV,TI,T2,T3,S}$ is spectral responsivity derived from onboard sphere calibration images. It is calculated by processing a sphere measurement through the aforementioned steps with one exception, and dividing by exposure time to create an ''SP'' CDR4. The exception is that the background image is taken looking into the unilluminated sphere instead of with the shutter closed, in order to subtract out the blackbody radiation of the sphere's structure. The ''SP'' product is corrected for non-reproducibility in shutter position by measuring the ''peak'' in sphere DN/ms near detector row 232, and scaling a multiplicative correction stored in the ''SH'' CDR4 by the magnitude of that peak.

[216] The SP CDR4 is divided by the sphere spectral radiance model stored in the ''SS'' CDR4 to derive a snapshot of instrument responsivity. The model uses as an input the choice of sphere bulb, and the telemetered sphere temperature to account for temperature dependence of the photodiode that drives the sphere's closed loop control. The actual responsivity applied to any scene measurement is a time-weighted average of responsivities derived from preceding and subsequent sphere measurements, to allow for continuous variation in temperatures of the sphere and IR detector. In the case of the VNIR detector, interpolated responsivity is further corrected for differences detector temperature from the times of sphere measurement, using telemetered detector temperatures and the ''TD'' CDR4.

[217] $M_{x,\lambda,Hz}$ applies the detector mask in the ''DM'' CDR4, flagging non-scene data (e.g., scattered light and masked pixels) with a value of 65535. This is a standard value for missing or ''bad'' (saturated) data.

#### 5.4.2.7. Converting Radiance to I/F

[218] $RD_{x,\lambda}$ is the observed spectral radiance in $W/m^2/steradian/\mu m$ at the instrument aperture, and is the output of the preceding steps for a scene measurement. That radiance may be converted to I/F by dividing by squared solar distance (stored in EDR and TRDR labels; see section 7.2) and the solar irradiance model stored in the ''SF'' CDR4. That model is itself derived convolving a predicted solar spectrum with the measured center wavelength (stored in the ''WA'' CDR4) and spectral band pass (stored in the ''SB'' CDR4) of every detector element.

### 5.4.3. Pointing Calibration

[219] CRISM generates four data products needed to map-project its multiband images using the Spacecraft, Planets, Instrument, Pointing, and Events software package, or SPICE (C. Acton, The Navigation and Ancillary Information Facility, http://naif.jpl.nasa.gov/naif/, 2005). The first is known as a ''frames kernel,'' and defines CRISM's orientation in an MRO-centered reference frame. This includes the orientation of the center of the VNIR and IR FOVs on the CRISM gimbal, and the orientation of the gimbal on the MRO spacecraft. Preliminary alignment information is discussed by *Troll et al.* [2005]. The second is the ''instrument kernel,'' a text representation of the ''CM'' CDR4 in Table 7, which gives the angular position of every VNIR or IR detector element relative to the optic axis. The third is a ''gimbal C-kernel,'' a time-ordered binary table of every gimbal orientation returned in image frame headers, assembled into two-week segments. The fourth is a set of ''metakernels,'' ordered lists of all the SPICE kernels needed to map-project images acquired during each two-week time span covered by a gimbal C kernel.

## 6. Instrument Operations

[220] Uplink planning and data processing are performed at the CRISM Science Operations Center (SOC), located at APL. Instrument commands are planned at the SOC and transferred to JPL for uplink. Downlinked CRISM data are forwarded with spacecraft housekeeping and pointing information to the SOC for processing and calibration. The SOC houses the facilities used for observation planning and command sequence generation, and hardware and software required to process, calibrate, and archive data. The SOC manages predicted SPICE kernels for data acquisition planning, and generates CRISM-specific kernels for data analysis and archival. The SOC maintains a time-ordered record of instrument commands and the resulting data. Downlinked spectra are processed to PDS-format files in near-real time. The SOC performs data validation and automatically processes routine radiometric calibrations, and it maintains an archive of raw, calibrated, and derived data products. The SOC also maintains online browse products for all observations, to provide a quick look at progress of the investigation and to select raw and/or calibrated data for more detailed analysis.

### 6.1. Observation Types and Campaigns

#### 6.1.1. Summary of Orbital Observing Modes

[221] During the Primary Science Phase, CRISM uses several basic observing scenarios as described in Table 8. In targeted mode (Figure 44), as a target on the Martian surface is overflown, the gimbal performs a continuous S-curve scan (a roughly S-shaped profile of gimbal angle versus time) to track the center of the target and take out along-track smear. Eleven slow, superimposed scans are also performed, barely altering the profile of gimbal angle with time. However, the superimposed scans have the effect of sweeping the slit FOV back-and-forth across the target point by several kilometers on the Martian surface, to build up spatial coverage. Hyperspectral image data (545 wavelengths) are taken during each of the 11 superimposed scans. The sixth image is at full resolution or uses 2x spatial pixel binning, resulting in a spatial sampling of 15–38 m/pixel depending on spacecraft altitude and which binning mode is used. The remaining images use 10x spatial pixel binning and obtain data at 150–200 m/pixel. The high-resolution image is the main objective of the observation, but taking all 11 scans results in a spatially resolved,

**Table 8.** CRISM Observing Modes During MRO Primary Science Phase

| Mode | Pointing | Description | Desired Coverage | |
|---|---|---|---|---|
| Targeted | tracking as shown, once per target | full resolution; spatial pixels unbinned for target: 18 m/pixel @300 km, 10x binned for EPF half resolution short; spatial pixels 2x binned for target: 36 m/pixel @300 km, 10x binned for EPF; same swath length as above half resolution long; spatial pixels 2x binned for target: 36 m/pixel @300 km, 10x binned for EPF; twice swath length as above | thousands of targets | |
| Atmospheric (EPFs) | tracking as shown but only center of target measured | spatial pixels 10x binned (~100 m/pixel @300 km) | 9° long. × 22° lat. grid every ~36° of Ls (3 non-contiguous days of EPFs) | atmospheric (EPFs) |
| Multispectral | nadir-pointed | multispectral survey; selected channels, spatial pixels 10x binned (~200 m/pixel @300 km) | ≥80% of Mars | |
| | | multispectral windows; selected channels, spatial pixels 5x binned (~100 m/pixel @300 km) | select areas plus sampling of seasonal variation at polar cap | |
| Calibration | Mars night or deep space | full resolution observations of onboard integrating sphere | daily | |

11-angle emission phase function (EPF) that provides the data needed for photometric and atmospheric correction of the central scan. The goal is to cover ~5000 targets in this manner.

[222] In atmospheric mode, the gimbal is also used to track a point on the surface, but there is no requirement to obtain high spatial resolution. Instead, all 11 scans use 10x spatial pixel binning to return reduced spatial resolution hyperspectral data.

[223] In multispectral mode, the instrument is fixed pointing at nadir, and a wavelength filter is used to return only key wavelengths. Spatial resolution is reduced by spatial pixel binning, helping to manage data volume. This mode of operation is intended to search for new targets of interest and to provide moderate spatial and spectral resolution mapping of surface mineralogic composition. Two modes of multispectral operation are supported: ~200 m/pixel (10x binned) ''multispectral survey'' mode which is designed to accomplish coverage rapidly, and ~100 m/pixel (5x binned) ''multispectral window'' mode which is intended for higher spatial resolution in key areas.

[224] In addition, radiometric calibrations using the onboard integrating sphere and bias calibrations are taken every orbit. Background measurements are embedded in all observations.

[225] Around the time of each night side equator crossing, basic checks of the instrument are performed. A memory checksum is dumped to check memory integrity. The shutter fiducial is powered briefly and the shutter is moved stepwise from positions 0 through 32, to verify that the fiducial is detected at expected steps, indicating that no shutter steps have been missed.

[226] Once monthly, infrequent calibrations and more comprehensive engineering and status checkouts are performed. A VNIR flat field is measured using a bland region on the day side of Mars. Over the night side, the redundant lamps in the sphere are intercalibrated, the focal plane lamps are imaged, and test pattern images are taken at all frame rates and binning modes to assess electronics health. Gimbal scans are taken during which high-rate attitude information is returned over the image channels, to assess health of the gimbal motor and encoder.

### 6.1.2. Details of Observing Modes

[227] Commanding of CRISM uses onboard macros, sequences of commands that configure the instrument for a particular operation, acquire data, and then return the instrument to a reference configuration. The data acquired by part or all of one macro using a single configuration of lamps, shutter, data compression, frame rate and exposure time is the fundamental data unit, an Experiment Data Record (EDR), that is archived to the Planetary Data System (PDS). Each observation is assigned a unique target ID during the observation planning process. Since each observation consists of multiple macros, multiple EDRs are generated for each observation and the generated EDRs share the assigned target ID. A target ID is used only once, and becomes the tracking number for the associated observation.

[228] CRISM science observations use seven core sequences of macros that translate into different sequences of EDRs (Tables 8, 9a, and 9b). Six of the sequences are for acquisition of science data with interleaved background (shutter closed) calibrations. The seventh sequence is for collection of regular radiometric calibrations including measurements of the internal integrating sphere and tracking of detector bias. (Other macro sequences are used for routine engineering and status checks.) The interaction of the spacecraft and CRISM's DPU in triggering an observation is described in more detail in section 4.8.5.

#### 6.1.2.1. Gimbaled Measurements

[229] Four of the science observations are intended for execution while the gimbal is tracking a target, and superimposing 11 slow scans: full resolution targeted observations, half resolution (long or short) targeted observations, and atmospheric survey EPFs. All follow the same basic outline. The gimbal is first set to +60° to begin the scan, which then starts at the commanded time. During approach to the target, the gimbal slowly sweeps the optical line-of-

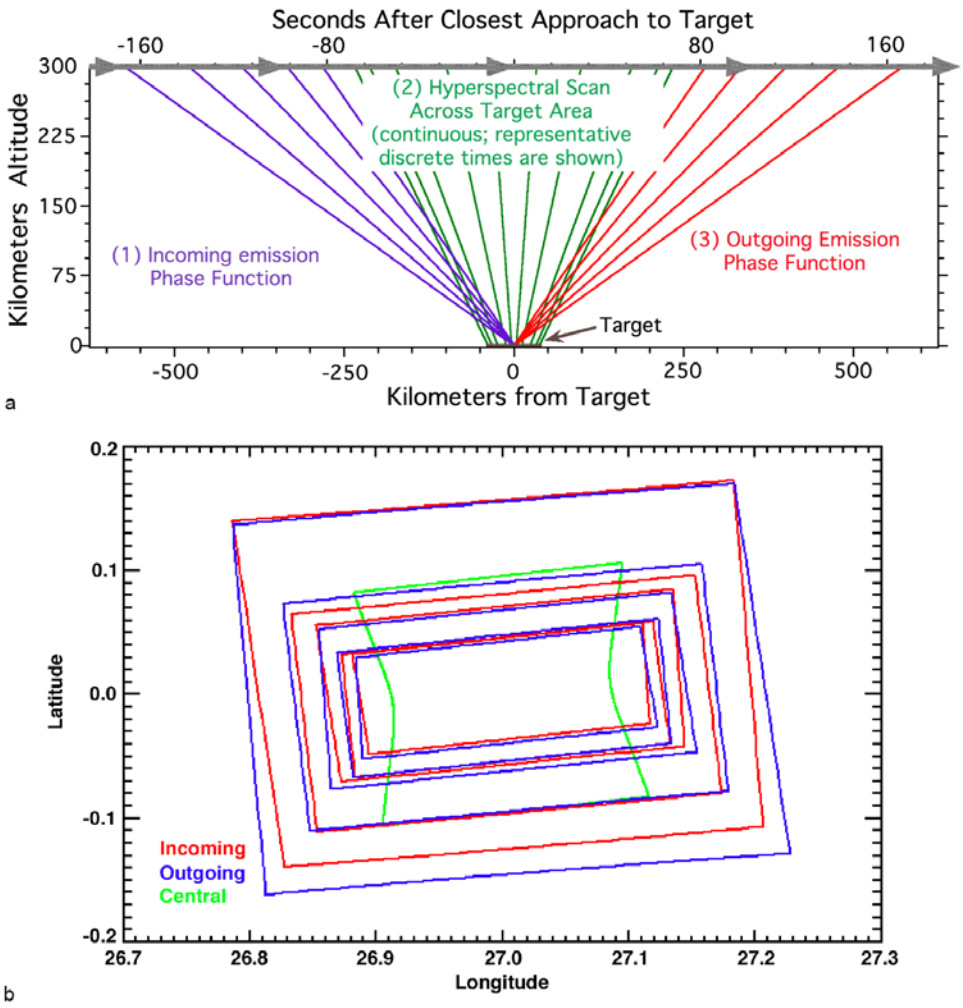


**Figure 44.** (a) During a targeted observation, as a target is approached, five short scans across it are performed during which hyperspectral data are taken spatially binned to conserve data volume (purple). Then, centered on the time of target overflight, a slow scan across the target is performed with minimal or no spatial binning (green). Finally, five additional short scans are performed as the target is departed (red). The result is 11 hyperspectral, multiband images, the 6th of which is at high spatial resolution. (b) Map-projected footprints of the 11 multiband images in a simulated targeted observation. The color scheme is the same as in Figure 44a. The hourglass shape of the central scan is due to the changing range to the target as the data are acquired.

sight (LOS) back and forth across the target five times. During target over-flight, the gimbal makes a slower, much longer sweep across the target. It is this long central scan that differentiates the classes of observations. The incoming EPF sequence is repeated outgoing, except in reverse order. Four background measurements are taken, marking the start and end of each group of EPF scans, effectively bracketing the incoming and outgoing EPF scans and the central scan. A 3.75 Hz frame rate is used for all of these data.

[230] A "full resolution targeted observation" (column 1 of Table 9a) utilizes CRISM's full resolution capabilities, at the expense of a relatively large data volume. The central scan is executed such that the LOS scans at a rate of 1 pixel (approximated as 60 $\mu$rad) per integration time, and crosses the target at mid-scan. The number of integrations is selected to occupy the range of gimbal angles between $\pm 35^{\circ}$. Depending on the altitude above a particular target, one of several choices of macros is used, and a corresponding gimbal setup macro is used for an initial angular offset to set up the image. The central scan and backgrounds are taken without spatial pixel binning, but the EPF scans are taken with 10x pixel binning and at a faster scan rate. The scan rates for both the central and EPF swaths yield approximately square pixels projected onto the surface.

[231] A "half resolution long targeted observation" (column 2 of Table 9a) covers a twice larger area, but at half the spatial resolution. It is intended for targets for which areal coverage is more important than the highest possible resolution. For the central scan, the initial angular offset is twice that for the full resolution targeted measurement. The LOS is scanned at a rate of 2 pixels (about 120 $\mu$rad) per integration time, and sufficient integrations are executed to

**Table 9a.** Translation of Gimbaled Observations Into EDRs

| Full Resolution Targeted Observation (3.75 Hz) | Half Resolution (Long or Short) Targeted Observation (3.75 Hz) | Atmospheric Survey EPF (3.75 Hz) |
|---|---|---|
| full spatial resolution background measurement with shutter closed | half spatial resolution background measurement with shutter closed | reduced spatial resolution (10x-pixel-binned) background measurement with shutter closed |
| reduced spatial resolution (10x-pixel-binned) measurement of Mars for EPF (*5 times*) | reduced spatial resolution (10x-pixel-binned) measurement of Mars for EPF (*5 times*) | reduced spatial resolution (10x-pixel-binned) measurement of Mars for EPF (*5 times*) |
| full spatial resolution background measurement with shutter closed | half spatial resolution background measurement with shutter closed | reduced spatial resolution (10x-pixel-binned) background measurement with shutter closed |
| full spatial resolution measurement of Mars | half spatial resolution measurement of Mars | reduced spatial resolution (10x-pixel-binned) measurement of Mars for EPF |
| full spatial resolution background measurement with shutter closed | half spatial resolution background measurement with shutter closed | reduced spatial resolution (10x-pixel-binned) background measurement with shutter closed |
| reduced spatial resolution (10x-pixel-binned) measurement of Mars for EPF (*5 times*) | reduced spatial resolution (10x-pixel-binned) measurement of Mars for EPF (*5 times*) | reduced spatial resolution (10x-pixel-binned) measurement of Mars for EPF (*5 times*) |
| full spatial resolution background measurement with shutter closed | half spatial resolution background measurement with shutter closed | reduced spatial resolution (10x-pixel-binned) background measurement with shutter closed |

occupy the range of gimbal angles between ±35° without overfilling. The duration of the scan is the same as for a full resolution targeted measurement taken from the same altitude. The central scan and backgrounds are taken with 2x pixel binning, but the EPF scans are taken with 10x pixel binning.

[232] A "half resolution short targeted observation" (column 2 of Table 9a) is a lower data volume alternative to the two types of targeted observations just described, intended to provide flexibility in covering more targets. It is otherwise identical to the half-resolution long version, except that the duration and initial offset of the gimbal for the central scan are halved, resulting in areal coverage approximately equal to that for the full resolution targeted measurement except with half the spatial resolution and one-quarter the data volume.

[233] In an "EPF measurement" (column 3 of Table 9a), the central scan is replaced with another EPF scan. The EPFs and background data are all taken with 10x pixel binning. An EPF measurement is intended to characterize the atmosphere or the average surface properties of a kilometers-sized area, as a part of tracking seasonal changes.

[234] In order to maximize the dynamic range available to the instrument, all of the gimbaled modes of observation are available at two integration times. A short exposure time will not saturate even on the brightest ices observed by OMEGA [*Langevin et al.*, 2005b], whereas a longer exposure time will provide higher SNR for non-ice materials (simulated in Figure 33) but saturates on the brightest ices.

#### 6.1.2.2. Nadir-Pointed Measurements

[235] The "multispectral survey" (column 1 of Table 9b) is intended to map large areas at the Mars Odyssey/THEMIS-IR scale of resolution, for two purposes: (1) to find

**Table 9b.** Translation of Nadir Observations Into EDRs

| Multispectral Survey (15 Hz) | Multispectral Window (30 Hz) | Radiometric Calibration (1 Hz) |
|---|---|---|
| reduced spatial resolution (10x-pixel-binned) background measurement with shutter closed | reduced spatial resolution (5x-pixel-binned) background measurement, shutter closed | full spatial resolution background measurement of the internal integrating sphere before it is powered on, 1 Hz |
| reduced spatial resolution (10x-pixel-binned) measurement of Mars | reduced spatial resolution (5x-pixel-binned) measurement of Mars | full spatial resolution measurement of the internal integrating sphere illuminated under closed-loop control using primary lamp, 1 Hz |
| *(repeat last 2 sequences n times)* | *(repeat last 2 sequences n times)* | full spatial resolution bias measurement with shutter closed at several exposure times at 1 Hz |
| | | full spatial resolution bias measurement with shutter closed at several exposure times at 3.75 Hz |
| | | 10x-pixel-binned bias measurement with shutter closed at several exposure times at 15 Hz |
| | | 5x-pixel-binned bias measurement with shutter closed at several exposure times at 30 Hz |

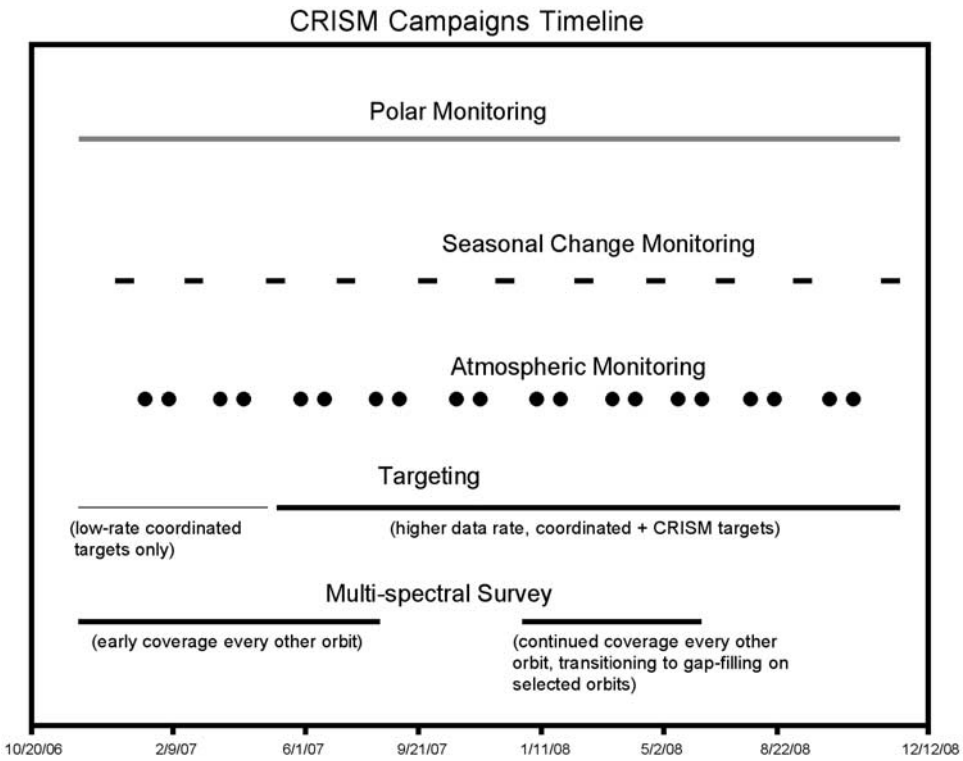


**Figure 45.** Schematic time phasing of CRISM's five observing campaigns over the course of MRO's Primary Science Phase.

sites for targeted measurements or (2) to characterize mineralogic composition over a large, contiguous area. The basic configuration is a repeating sequence of alternating Mars-viewing and background measurement macros. Multispectral survey data and accompanying background calibrations are taken in 10x pixel binning mode at 15 Hz, yielding 200-m effective pixels projected on Mars.

[236] Two parallel versions are available each with 73 total wavelengths, 18 from the VNIR detector and 55 from the IR detector. In one version, all data are compressed losslessly and remain in 12-bit format. In the second version, intended as a contingency if downlink is unexpectedly limited, the Mars measurements are converted on board to 8-bit format using LUTs that vary with wavelength to minimize quantization errors. Background calibrations remain in 12-bit format. Excluding ices, translating 12 to 8 bits entails quantization at up to 5 times the noise level, resulting in effective degradation of SNR. However, the dynamic range of surface materials *including* ices is so large that fitting all of the data into an 8-bit dynamic range would entail losses in effective SNR of up to >10. No matter the downlink, polar regions will be mapped losslessly to avoid this additional loss.

[237] ''Multispectral windows'' (column 2 of Table 9b) resemble the multispectral survey, except that they are taken at 30 Hz with 5x pixel binning, yielding 100-m effective pixels projected on Mars. These data are always taken losslessly compressed in 12-bit format. Multispectral windows have three basic uses:

[238] 1. Polar monitoring. Selected parts of the polar region are observed several times around specific periods of Ls to monitor seasonal changes in the polar cap.

[239] 2. Ride-alongs. If a HiRISE or CTX measurement is not coordinated with a CRISM targeted measurement (see section 6.2), then a 15-second duration multispectral window with a preceding dark measurement may be executed, with the window centered on the center of the HiRISE or CTX target. This insures that science observations by either of those instruments are always accompanied by some type of CRISM observation.

[240] 3. Depending on downlink availability, multispectral windows can be used in place of the multispectral survey for mapping selected regions of the planet. Because of lower SNR than in survey mode, this is only intended for increased spatial resolution of bright, heterogeneous deposits.

#### 6.1.2.3. Other Calibrations

[241] ''Radiometric calibrations'' (column 3 of Table 9b) are performed nominally several times daily. A calibration consists of a set of sphere measurements with the sphere operated in a closed loop, and a set of measurements of ambient background inside the sphere. These are accompanied by bias measurements at whatever frame rates are used in nearby parts of the orbit. These data are used to recover radiometric responsivity and to track instrument bias.

[242] A calibration source intercalibration is performed monthly to track long-term changes in system response. Normally, the VNIR-controlled sphere lamp is used for radiometric calibration, because its placement inside the sphere results in lesser effects of shutter position nonreproducibility than does the IR-controlled lamp (see section 5.3.2). The IR-controlled lamp is held as a reference. To track possible changes in radiance from the VNIR-controlled lamp, both sphere lamps are measured in se-

quence. At the same time, focal plane lamps are imaged at all frame rates (see section 5.3.1).

#### 6.1.3. Observing Campaigns

[243] CRISM's science objectives are addressed using the seven core types of observations in five distinct but temporally overlapping "campaigns" (Figure 45). The "multispectral survey campaign" is heavily concentrated during the first few months of the Primary Science Phase, when every other orbit is dedicated nadir-pointed in order to build up coverage. Additional coverage is also obtained by filling unused time between targeted observations.

[244] The "targeted observation campaign" is the core of CRISM's data acquisition, whose planning is discussed in detail in section 6.2. Due to changing Earth-Mars distance, MRO's downlink rate will increase by up to a factor of three during the first year of the Primary Science Phase. At the higher downlink rates the multispectral survey is suspended to provide maximum flexibility for spacecraft pointing for targeted observations.

[245] Two campaigns are intended to track seasonal changes in the surface and atmosphere, and together form the "atmospheric survey." The "atmospheric monitoring campaign" consists one Martian day of pole-to-pole EPFs every $\sim 9^\circ$ of solar longitude (Ls; a measure of Martian season, where $0^\circ$ is northern hemisphere vernal equinox) to acquire a low spatial density global grid of EPFs. There is sufficient time for 8 EPFs in an orbit, one approximately every $22^\circ$ of latitude. Alternate orbits (projected onto the planet) are offset in latitude by about $11^\circ$ north or south to increase latitudinal resolution. Longitude spacing between the orbits is about $27^\circ$.

[246] The "seasonal change campaign" occurs approximately every $\sim 36^\circ$ of Ls. A grid similar to that executed during the atmospheric monitoring campaign is taken on 3 non-contiguous days over about 2 weeks, to provide a higher spatial density grid (longitude spacing about $10^\circ$) to monitor seasonal changes in surface material spectral properties, especially adsorption and desorption of $H_2O$. The grids are overlain on a best-effort basis; repeat coverage to ±50 km can be accomplished from careful selection of the orbits. Every 3 orbits projected on the planet, the EPFs are offset by $0^\circ$, $+8^\circ$, and $-8^\circ$ north or south to increase latitudinal resolution.

[247] The final campaign is "polar monitoring," which continues throughout the Primary Science Phase, A variety of representative areas of the permanent and seasonal cap [*Kieffer et al.*, 2000; *Kieffer and Titus*, 2001; *Langevin et al.*, 2005b] are monitored at the Ls ranges during which transitions in thermal and spectral properties occur, to monitor the growth and ablation of the seasonal caps. This is accomplished primarily using long multispectral windows of 3-minute or greater duration, covering swaths 500 km or more in length at 100 m/pixel, augmented by targeted observations of key regions.

### 6.2. Uplink Planning

[248] The primary inputs for planning CRISM observations are as follows:

[249] 1. Map-projected multispectral survey data built up as they are returned.

[250] 2. A list of regions of interest for targeted observations, with constraints on Ls if applicable.

[251] 3. The predicted spacecraft trajectory.

[252] 4. A desired timeline for the nadir-pointed atmospheric monitoring and seasonal change campaigns.

[253] 5. A schedule for internal calibrations and health checks.

[254] 6. Allocations for SSR space and downlink.

[255] 7. A model of how CRISM's data compress in each operating mode.

[256] 8. A seasonal model for the margin of the polar cap.

[257] 9. Spacecraft roll, stability, and downlink limitations.

[258] 10. Regions of interest for other MRO instruments.

[259] The outputs are observation loads with a time series of macros and a gimbal profile for each target ID, and payload target files or PTFs which define the latitudes, longitudes, elevations, approximate times and other ancillary information for observations. The observation loads are the input to the CRISM DPU, and the PTFs are converted to inputs to the spacecraft (as well as serving as a planning tool). The software package that identifies CRISM's observation opportunities, selects between alternative times to view the same targets, and generates the files for uplink is called "JMRO." It is a built on core capabilities of the "SciBox" software shared with the MESSENGER mission [*Choo et al.*, 2001].

[260] MRO supports two types of observations. In an "interactive observation," or IO, the spacecraft points up to $30^\circ$ off-nadir to a particular latitude, longitude, and elevation and determines the time at which to execute an observation at those coordinates. The pointing and timing calculations are done using the onboard ephemeris. Because IOs are limited in number and can disrupt other instruments' desired pointing, they are scheduled using an inter-instrument coordination process on ground. A total of 15 minutes is allotted for an observation: 5 minutes for the spacecraft to slew to the off-nadir pointing required to cross over a target, up to 7 minutes for data acquisition to allow for the longest EPF, and 3 minutes for the spacecraft to return to nadir pointing. "Non-interactive observations" or NIOs are observed at spacecraft nadir, and are mostly an internal activity for each of MRO's investigations. An NIO is initiated on the basis of the expected time of crossing of the target's latitude. In NIOs the only inter-instrument coordination is adding ride-along observations. For both IOs and NIOs, the spacecraft adjusts its attitude relative to the ground track vector (yaw) to take out cross-track smear over CRISM's and HiRISE's finite integration times.

#### 6.2.1. Atmospheric Survey

[261] The atmospheric monitoring and seasonal change campaigns contain contiguous EPF measurements pole to pole, precluding off-nadir pointing during their acquisition. During the planning process as IOs are laid in, the continuous nadir pointing is preserved using an "exclusion zone" suspending off-nadir pointing for the duration of the observations. The exclusion zones are timed to maintain the desired observation frequency and times as described in section 6.1.3.

[262] For the component EPFs in the atmospheric survey, the macro sequence for each observation is standard. However, the gimbal profile is unique to each observation to maintain tracking accuracy on the target regardless of orbit altitude and target elevation. All of the targets are non-interactive, and their latitudes are computed to maintain

adequate spacing to allow for full EPF measurements using the gimbal's ±60° range, and to allow time for rewind of the gimbal between observations.

#### 6.2.2. Multispectral Survey

[263] At the beginning of the Primary Science Phase when multispectral survey coverage is low, terminator-to-terminator coverage will be obtained every second orbit. As with the atmospheric survey, an exclusion zone will be used during the planning cycle to suspend off-nadir pointing for the duration of the observation. Data are acquired in 3-minute segments separated by 5-second gaps during which background measurements are taken.

[264] As coverage builds to 50% or more, this strategy is modified. During processing of downlink the multispectral survey is projected into a global set of 1964 map tiles. For planning, a reduced-resolution 64 pixel/degree coverage map is generated by the SOC and ingested into JMRO. The predicted spacecraft ground track is overlain on the map, and times at which gaps are overflown are identified. Those times are treated as NIOs in the target selection process.

#### 6.2.3. Targeted Observations

[265] A major input to the process of identifying times and locations for targeted observations is a region of interest (ROI) list. The list contains polygons of latitude and latitude coordinates that outline polygons identified from TES, THEMIS, OMEGA or other data, on the basis of attributes suggestive of exposure of interesting mineralogy. These include high THEMIS nighttime temperature (indicating bedrock or highly indurated material), presence of clay, sulfate or other key mineralogic absorptions in OMEGA data, or low cover of dust in a region representative of a major geologic unit. Other ROIs will include circumpolar locations at which growth and ablation of the seasonal cap are monitored, and landing sites for past, ongoing, or potential future missions. Each ROI entry has a scaled priority from 1–5 plus constraints, if any, on the Ls or illumination geometry required for its observation. Once the Primary Science Phase is underway, new ROIs will be added from the multispectral survey.

[266] The are two general types of ROIs, one for which coverage of any portion is adequate (''any''), and one for which complete coverage is needed (''all''). An ''all'' ROI is broken into a grid of points whose spacing is the typical size of a targeted observation, and each point is treated in the sequencing process as an ''any'' ROI. Gaps in the multispectral survey are ''virtual'' ROIs identified by JMRO using, as an input, a 64 pixel/degree coverage map generated from mosaicked multispectral survey data (section 7.2).

[267] The observing history of targeted ROIs is documented using an ''observation tracking table.'' Essentially, this is a list of the ROIs for which observations have been scheduled, appended with uplink-planning and downlink-processing information. When an observation is commanded for an ROI, the commanded parameters for the observation are appended to the list, including the type of observation, the date and time when observation is planned, and the expected latitude and longitude boundaries of the observation. Once the data are downlinked and processed by the SOC, the list is further appended by information on the observation's validity (e.g., whether the correct instrument configuration occurred, and the extent of missing data) and data quality (e.g., whether the data are unsaturated, and the observation was executed at its planned location). The observation tracking table not only is part of the data validation process (section 7.3), but it also serves as the input back into the planning process as to which ROIs have been successfully measured, which need to be remeasured, and which are outstanding.

#### 6.2.4. Sequencing Process

[268] Figure 46 shows a simplified version of the sequence of activities by which observations are planned. The process is iterative and one 2-week block of observations is planned as a unit. To start the process, exclusion zones are identified for the multispectral and atmospheric surveys as well as for routine spacecraft maintenance operations. A relatively small number of ''must-have'' observations from each of the MRO investigations are collected, and any conflicts with the exclusion zones are negotiated; there is an allowance for a limited number of interruptions of CRISM's exclusion zones.

[269] In parallel, opportunities to image ROIs with interactive or non-interactive observations are identified. Each ROI and its Ls constraints are examined, and observing status is checked in the observation tracking table. If no observation has yet been commanded for the desired Ls range, or if one was commanded but was not successful, opportunities to observe it are identified on the basis of the predicted spacecraft trajectory. Targets are ranked by a ''weighted priority'' that includes the priority assigned in the target list and a comparison of the opportunity's illumination conditions with the best available for that target.

[270] The highest weighted-priority opportunities are proposed for interactive observations. This occurs early during the planning cycle at which time cross-track uncertainties in spacecraft position render all ROIs off-nadir at their time of measurement. There is only a limited number of off-nadir opportunities, and no more than four per orbit. The MRO investigation teams exchange lists of proposed IOs. Conflicts in scheduling are resolved, and as appropriate, teams may piggyback targeted observations on other teams' opportunities as ''coordinated observations.''

[271] Once IOs have been finalized, NIOs are added to fill the downlink allocation. Four classes of observations are added at this point:

[272] 1. ROIs that were not selected as off nadir IOs, and that are large enough for some coverage to be obtained as nadir-only observations,

[273] 2. Gap-filling swaths for the multispectral survey.

[274] 3. Sphere and bias calibrations scheduled around the targeted and survey observations, maintaining the calibration observation frequency needed for radiometric accuracy (see section 5.4.1).

[275] 4. Regular instrument health and status checks (see section 6.1.1).

[276] How many observations can be taken is determined by several factors: the fraction of total downlink allocated to CRISM, the volume of SSR space allotted to CRISM, whether spatial pixels are binned, how many wavelengths are returned, and the compressibility of different types of data. Lossless compression ratios are affected by the illumination level in the data, smoothing of fixed patterns in slit transmission (section 4.2) and detector bias (section 5.3.3) by spatial pixel binning, and spreading of bad pixels (section 5.3.3) by pixel binning, Typical ratios are 1.3–2.1.

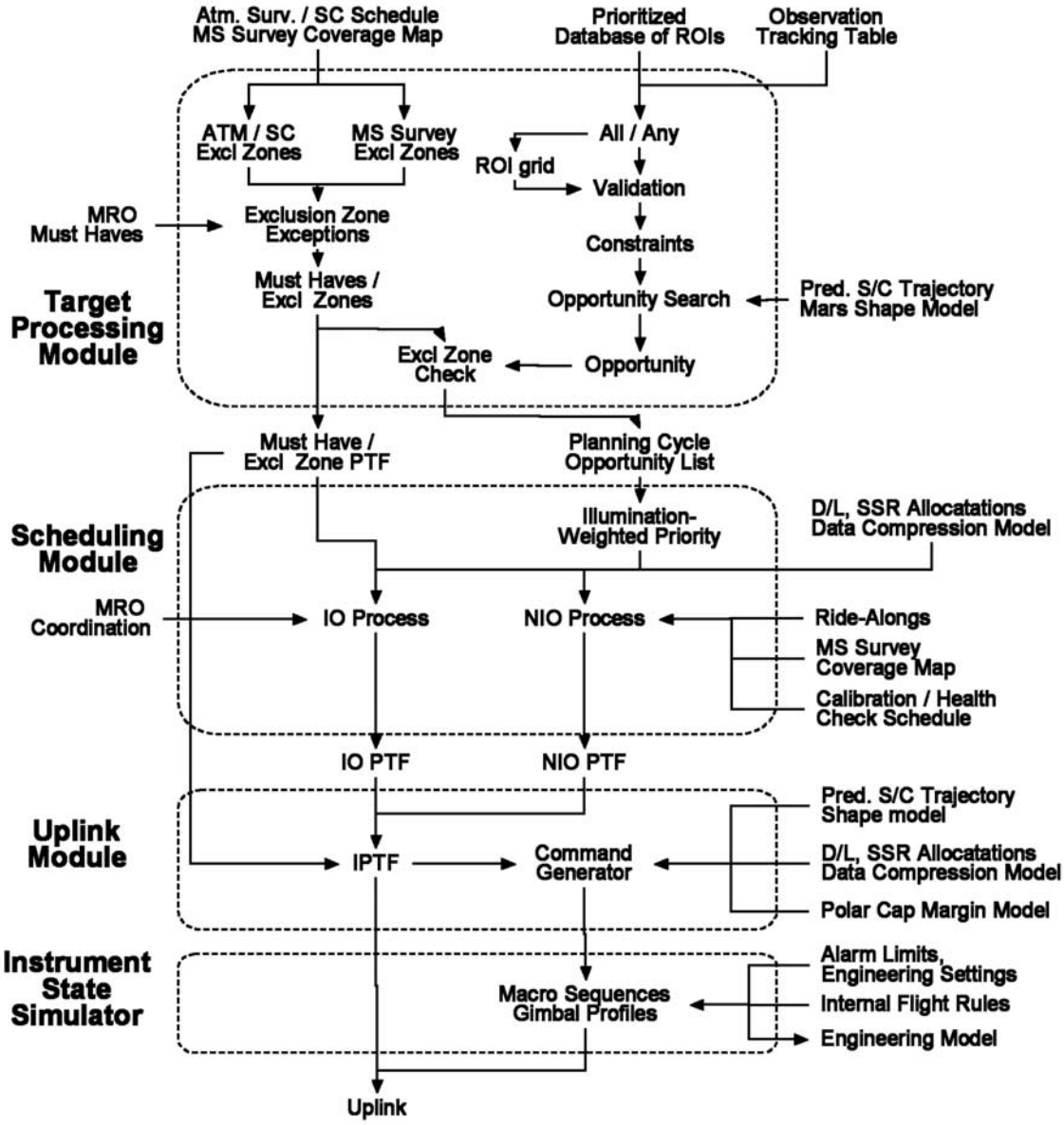


**Figure 46.** Schematic flow of the CRISM uplink planning and commanding process.

[277] Again, observation plans are exchanged between MRO teams, and CRISM ride-alongs (section 6.1.2.2) are inserted to accompany HiRISE and CTX observations. Once this is done the PTF is in its final form as an ''integrated payload target file'' or IPTF. The IPTF is a biweekly product.

[278] Finally, a command generator module generates the observation loads and gimbal profiles to accompany the IPTFs. This is done up to three times weekly, using the latest predicted spacecraft trajectory. For each gimbaled observation the appropriate gimbal profile coefficients are calculated using the trajectory and a shape model of Mars, so that the target point on the surface is accurately tracked. The model of the polar cap margin is used to select long- or short-exposure time macros for non-icy or icy regions, respectively, and the range to target is used to select the appropriate duration macro for the central swath of each targeted observation and to select the wait times between macros. A final check of data volume is performed and spatial pixel binning or wavelength selection is modified if needed to adjust predicted data volume.

### 6.2.5. Uplink Validation

[279] Commands are validated before uplink using an Instrument State Simulator which compares them against a set of internal flight rules for instrument timing and configuration, and compares engineering settings against values that could trigger alarms. For convenience, time histories of engineering settings of the instrument and the data compressibility model are maintained as CDR6s (Table 6). In the case of special, non-routine observation sequences, commands are test-run on a CRISM engineering model maintained at APL.

## 7. Downlink Processing and Data Products

[280] The software package in which downlink processing is implemented in the CRISM Science Operations Center is Planetary Image Processing Environment, or

PIPE, a commercial product with heritage from earlier planetary missions including Clementine, Stardust, and MESSENGER. PIPE processes data in a batch, pipeline mode. An interactive version for custom processing, the Rapid Environmental Assessment and Compositional Tool (REACT), provides standard capabilities to visualize CRISM data and to apply calibrations from raw units of DN to units of radiance or I/F (these transformations are discussed in section 5.3.2). REACT runs on Windows, Linux, and Macintosh OS10 platforms.

### 7.1. Health and Status Monitoring

[281] Instrument autonomy, as described in section 4.8.7, is CRISM's first line of defense against off-nominal conditions. The SOC supplements that function with long-term trending of instrument performance and with automated responses to instrument alarms.

[282] Telemetered status packets containing measurements of currents, voltages, and temperatures are converted to physical units using appropriate calibration files (section 5.4.2) and maintained as text files. Plots of each value versus time are automatically generated, covering the last day, last week, and last month. Data are plotted along with alarm limits to assess long-term changes in instrument behavior. Selected housekeeping items that relate to component health are plotted against each other for the same time spans (e.g., sphere current versus sphere temperature, Figure 42, where departure from the relationship measured on ground could indicate changes in bulb or photodiode behavior and hence drift in onboard radiometric calibration). These tools are all web-accessible to facilitate remote monitoring of instrument status.

[283] If an alarm packet is received, it is transmitted to appropriate personnel via e-mail and pager.

### 7.2. Data Product Generation

[284] The overall strategy in defining CRISM data products and the pipeline to produce them is a recognition of the following:

[285] 1. CRISM's expected downlink, at least 7.8 Tb and possibly up to 15 Tb, is a challenge to monitor.

[286] 2. Rapid turnaround of map-projected multispectral survey data is essential to targeting regions of interest, even if data calibrations are only preliminary.

[287] 3. Data calibration is sufficiently complex that it is a high priority to deliver to the community products at least in units of radiance, and preferably I/F, rather than raw form.

[288] At the same time, history shows that calibration of planetary optical instruments continues long after their operational lifetimes. Due to its complexity, CRISM is likely to be no exception. Every conceivable aspect of instrument calibration is being recorded in PDS-compliant CDRs (Tables 6 and 7), and the use of the calibration data is exhaustively documented in an accompanying Data Products Software Interface Specification (SIS) [*Murchie et al.*, 2006].

[289] The CRISM data stream downlinked by the MRO spacecraft unpacks into a succession of compressed image frames with headers. CRISM standard data products represent rearranged and/or calibrated values from the data stream, or corresponding derived products whose basic unit of organization is that portion of the output from one macro which has a consistent instrument configuration (shutter position, frame rate, pixel binning, compression, exposure time, on/off status and setting of different lamps). The flow of data processing and the relationship of different data products are shown in Figure 47. We define standard products to be those products generated using well-defined and validated procedures and destined for periodic delivery to the Planetary Data System. Special products are those that will be produced during analyses of the CRISM data, or that apply post-processing corrections requiring extensive validation during the Primary Science Phase. These products may be delivered to the PDS or not, depending on the quality of information content and the expected importance of the products for the science community. Tables 9a and 9b list both standard and special products.

[290] In the standard product Experiment Data Record (EDR), CRISM data values are unmodified but are rearranged. The headers are stripped off and placed into a text list file, and individual image frames are merged into a multiband image. There is one EDR per focal plane. The list file contains housekeeping items, gimbal position at the beginning, middle, and end of each exposure, and 10 additional ground-derived, frame-specific items that are useful in data validation, processing, and sorting (e.g., a data quality index, Ls, solar distance, local time of day, longitude and latitude, and incidence, emission, and phase angles at the center of the FOV).

[291] Subsequent processing of EDRs depends on their contents. Those containing bias measurements or measurements of background, focal plane lamps, or the internal integrating sphere are processed into level-4 CDRs as described in section 5.4.

[292] Scene data are processed into a second major standard product, the Targeted Reduced Data Records (TRDR). This product is comparable in structure to a EDR except that image data are converted to units of radiance using level-4 and level-6 CDRs, and currents, voltages, and temperatures in the list files are converted into physical units using level-6 CDRs. A TRDR may also contain one or more of three accompanying special products. The first special product is a multiband image of I/F, i.e., radiance divided by pi times the solar spectrum at the distance of Mars. The second special product is a multiband image of Lambert albedos of the surface, from which effects of atmospheric scattering and attenuation and surface thermal emission have been subtracted as described below. The third is a multiband image containing spectral indices or "summary products" derived from I/F or Lambert albedo. Summary products include key Lambert albedos, band depths and spectral reflectance ratios. The basis, formulation, and testing and validation for all of the summary products using OMEGA data are described in detail by *Pelkey et al.* [2007]. Examples of some are shown in Figures 4 and 5. EPF and targeted observations and multispectral windows are all processed into TRDRs. A multispectral survey observation is first processed into a temporary TRDR, and then map projected into a distinct data product discussed below. This temporary TRDR is not a PDS-deliverable.

[293] Each TRDR is accompanied by a set of backplanes useful for map projection and post-processing corrections, the Derived Data Record (DDR). A DDR is constructed in

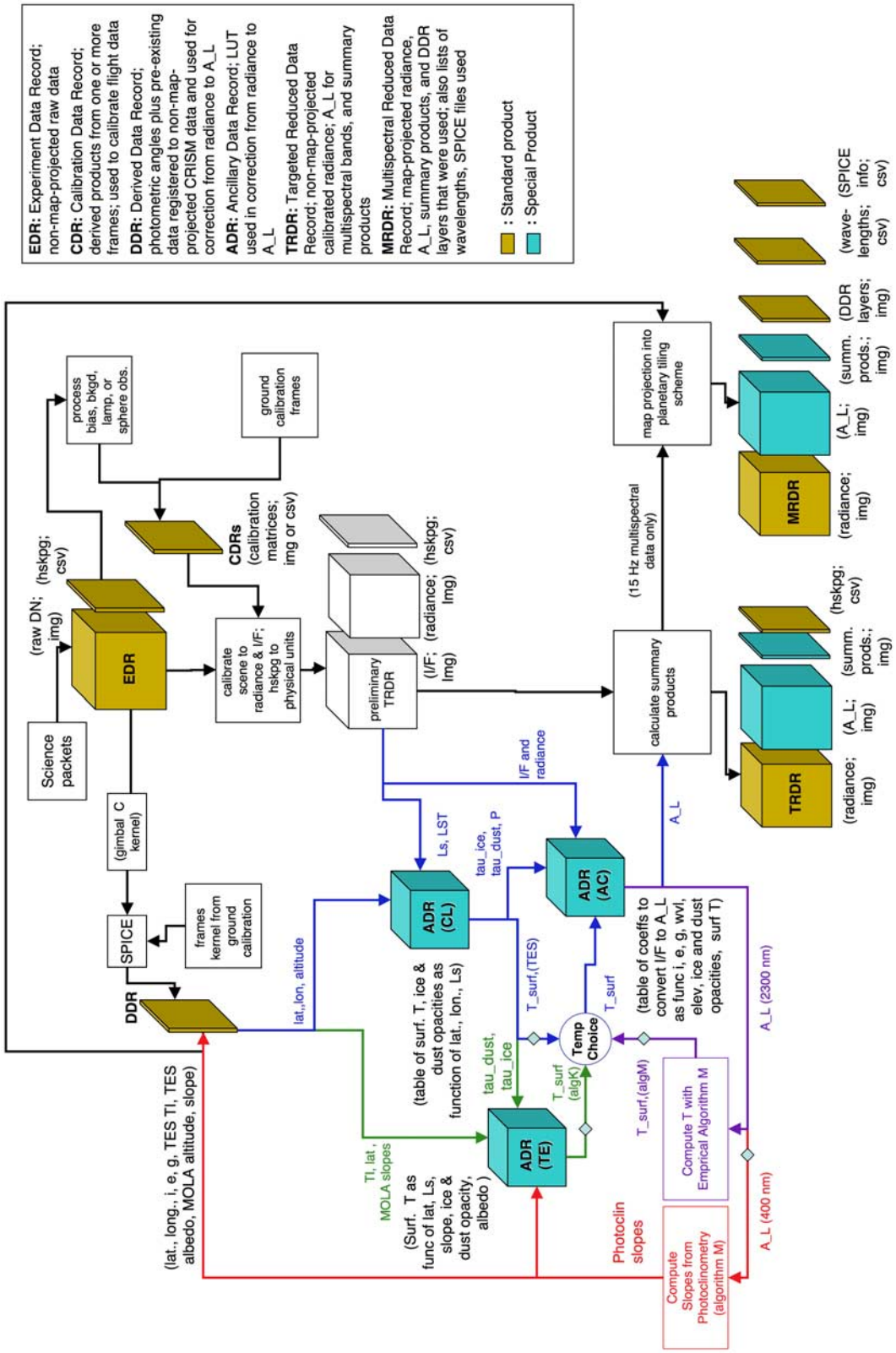


**Figure 47.** Sequential processing of EDRs to yield RDRs of Mars data, showing the roles of CDRs and ADRs.

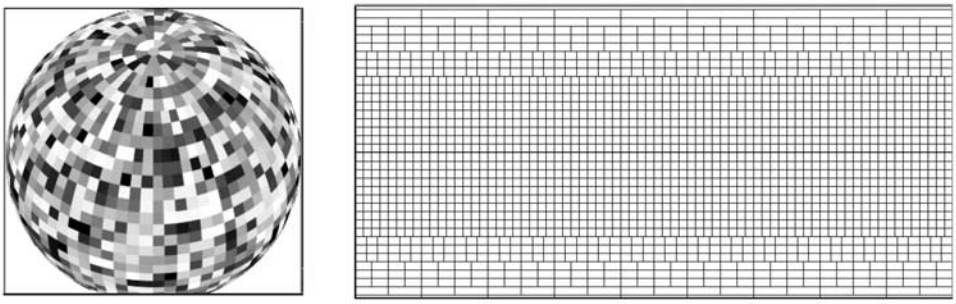

**Figure 48.** Tiling scheme for the map-projected multispectral survey, shown in orthographic view and as a global, simple cylindrical map form.

two stages. First, a TRDR is projected onto a Mars Orbiter Laser Altimeter (MOLA) shape model, to determine the latitude, longitude, and incidence, emission, and phase angle for every spatial pixel. This information is encoded in different layers of a multiband image, and is used for map projection and for photometric corrections. Second, the latitude and longitude of very spatial pixel are used to recover MOLA slope magnitude and azimuth, and TES thermal inertia and bolometric albedo from SOC-maintained basemaps. The relevant information for each spatial pixel is as additional layers, and used in post-processing to estimate a correction for thermal emission from the surface.

[294] Further processing of CRISM data is driven by three objectives: (1) accounting for effects of the atmosphere and thermal emission on surface spectra, (2) organizing the expected ~5000 swaths of multispectral data into a more useful map-projected format, and (3) providing quick looks at the contents of key data products.

[295] For a first assessment of atmospheric and thermal effects, to allow rapid identification of new ROIs and to quickly assess the information content of targeted observations, we leverage the fact that Martian weather tends to be highly repeatable year to year [e.g., *Smith*, 2002, 2004; *Smith et al.*, 2003]. That climatic record and its effects on surface spectra are recorded in a special data product called Ancillary Data Records, or ADRs. An ADR is a hyperdimensional binary table containing reference information used by algorithms that correct at-sensor radiance to Lambert albedo of the surface, with atmospheric and thermal effects "removed." The axes of an ADR are physical parameters that may describe some scene, such as latitude, longitude, solar longitude, incidence, emission, or phase angle, or surface properties extracted from TES or MOLA data including bolometric albedo, thermal inertia, elevation, slope magnitude, or slope azimuth. For any TRDR, these physical values are recorded in the accompanying DDR. To correct a given spatial pixel in a TRDR for its climatologically predicted atmospheric and thermal effects, that spatial pixel's physical values from the DDR are used as coordinates to locate within the ADR a multiplicative correction from I/F to Lambert albedo. The corrections are precomputed using DISORT modeling [*Stamnes et al.*, 1988] of the expected effects of the atmosphere and thermal emission under different illumination conditions, based on TES climatology as a function of latitude, longitude, and solar longitude. Four different algorithms of varying complexity and fidelity have been developed to apply the ADR corrections, shown as the four differently colored pathways through the ADR portion of the data processing pipeline in Figure 47. Once data have been acquired during the primary science phase and the algorithms' performance has been evaluated, one of the four algorithms may be adopted or modified for pipeline production of special products.

[296] A Multispectral RDR (MRDR) is a standard product that consists of multiple strips of multispectral survey data mosaicked into a map tile. The mosaic is uncontrolled (accepting existing pointing data, often resulting in image mismatch at seams within a mosaic). A global pattern of 1964 such tiles (Figure 48) has been developed, forming the major data product for multispectral survey observations. Each tile contains a multiband image of radiance extracted from a temporary TRDR, a multiband image of the DDRs used for map projection, plus text files having information on the wavelengths of the layers of the radiance and surface I/F multiband images and on the SPICE metakernels used for map projecting the component EDRs. The DDR multiband image contains additional layers that provide traceability back to the spatial pixel of the source EDR and its wavelength calibration, such as target ID, frame number within the EDR, and spatial column in that frame. Each MRDR may also contain either or both of two special products, a multiband image of Lambert surface albedo or a multiband image of summary products.

[297] Browse products are Portable Network Graphics (PNG) files that collapse each spatial pixel of a data product into a scaled value to create a synoptic spatial image with a data volume up to 500 times smaller than the full data. For example, the browse product for an EDR is median DN at all wavelengths in each spatial pixel. For a TRDR there are 5 browse products: a true-color image from VNIR data, a scaled image of 1330-nm I/F, and one VNIR and two IR red-green-blue false color images in which each color plane represents the scaled value of one summary product. The VNIR false color image is a representation of variations in ferric mineralogy; one IR false color image is a representation of spatial variations in olivine and pyroxene abundance and pyroxene composition; and the other IR image represents variations in hydroxyl and bound water in minerals.

[298] The TRDRs from targeted mode observations will be used, with the included EPF data, to model the surface and atmospheric contributions to radiance and to extract surface I/F values as special products. The procedure to conduct these extractions will use a combination of precomputed look-up tables (ADRs) and radiative modeling of

**Table 10.** Schedule for Delivery of Data to the PDS

| Product | Delivery Frequency[a] |
|---|---|
| *Standard Products* | |
| Data product SIS | Launch |
| Instrument description text and figures | Launch + 6 mo |
| Spectral library | MOI |
| Instrument calibration files | MOI + 6 mo |
| Record of observations | Once every 3 mo. after 6 mo. validation |
| EDRs: Raw spectral cubes | Once every 3 mo. after 6 mo. validation |
| DDRs and radiance part of TRDRs: Calibrated targeted and EPF cubes with pointing, geometric, physical data | Once every 3 mo. after 6 mo. validation, again at EOM + 6 mo |
| CDRs: Reduced flight calibration files | Once every 3 mo. after 6 mo. validation, again at EOM + 6 mo |
| Part of MRDRs: Map-projected multispectral calibrated radiance, tiled DDR components | Up to every 6 months, again at EOM + 6 months |
| *Special Products* | |
| ADRs: LUTs for performing atmospheric, photometric, and thermal corrections | Coincident with publications, and at EOM + 6 mo |
| Part of TRDRs: Summary products | Up to once every 3 mo. after 6 mo. validation, again at EOM + 6 mo |
| Part of MRDRs: Map-projected multispectral surface spectra, summary product s | Up to every 6 months, again at EOM + 6 months |
| MTRDRs: Selected map projected, targeted observations as I/F (approximately 50 sites) | Coincident with publications, and at EOM + 6 mo |

[a]MOI, Mars orbit insertion; EOM, end of mission.

the spectral radiances. Results will be map-projected and define the MTRDR special product, where M stands for "mapped." An algorithmic description of the surface I/F retrievals will be included with these special products.

### 7.3. Data Validation

[299] Data validation is an iterative process throughout the history of processing the CRISM data set. Several tools are used to assess and to record data validity:

[300] 1. Systematically invalid pixels are replaced with a bad data value. Missing frames or portions of frames are replaced with a value of 65535, a PDS standard value for missing data. Pixels that cannot have meaningful values at the TRDR level (i.e., masked and scattered light columns at the edge of each detector) are also set to 65535 in TRDRs.

[301] 2. Single pixels with unreliable values are flagged. Locations of bad pixels are flagged in the bad-pixel CDR4 (Table 7) and are interpolated over. Cosmic ray hits are easily detected in the raw data as spatial-temporal "spikes," and their locations are indicated in the label accompanying a TRDR.

[302] 3. A data quality index (DQI) is used to encode figures-of-merit into one parameter that is recorded for each frame of an EDR or TRDR in the corresponding line of the list file. At the EDR level, missing data, saturation, and basic hardware status are assessed. In the case of a hardware or configuration discrepancy (shutter position, lamp status or level, pixel binning, frame rate, channel selection, power status of detectors), processing of the image data to TRDR level does not occur in order to avoid introducing invalid results. At the TRDR level, coverage of the targeted region of interest is assessed, and underexposure is flagged if it occurred. Usage of temporally non-adjacent calibration files (due to loss of data from a background, lamp, or sphere macro) or high spectrometer housing temperature is flagged. Once the summary product is derived, an excessive 440-nm I/F is flagged as a possible indication of water ice clouds.

[303] 4. For each target ID, a summary of EDR or TRDR data validation results is written into a text file accompanying the data files.

[304] 5. For each EDR or TRDR, a summary DQI is entered into the observation tracking table to indicate if data corruption requires the observation to be retaken.

### 7.4. Data Delivery

[305] CRISM data products are delivered to the PDS Geosciences Node (Washington University, St. Louis, MO). CRISM archive volumes will be assembled and validated by the PDS Geosciences Node and made available to the public via the Geosciences Node web site. The Geosciences Node will also transfer CRISM archive volumes to the National Space Science Data Center (NSSDC) for long term storage, according to PDS policy, using a transfer medium agreed upon by PDS and NSSDC.

[306] Table 10 summarizes the delivery schedule for CRISM Data Products.

### 7.5. Spectral Library

[307] To help support interpretation and analysis of retrieved surface I/F values for both multispectral and targeted mode observations, we have also delivered to the PDS an extensive spectral library of minerals, soils, and rocks acquired over the spectral range in which CRISM operates. Many minerals of interest such as salts and phyllosilicates have absorptions due to bound water that are much stronger under ambient terrestrial conditions than under desiccating Martian surface condition. Therefore hygroscopic phases were measured at infrared wavelengths after purging with scrubbed (moisture-depleted) air or dry $N_2$, typically for 12 hours. The spectra oversample CRISM's spectral resolution, so that the instrument's spatially variable spectral resolution can be taken into account. "WA" and "SB" CDR4s described in section 5.4 and Table 7 can be used to convolve any library spectrum to its expected resolution at any spatial position in the CRISM FOV.

[308] The first delivery of the CRISM Spectral Library to the PDS Geosciences node was made at MRO Mars orbit insertion (10 March 2006), consisting of 1134 samples with 2260 spectral analyses. The contents of the library are classified in a hierarchical schema including material type (natural or synthetic), material origin (e.g., Earth, Mars, moon, meteorite, etc.), classification (e.g., rock, mineral, unconsolidated), mineral class (e.g., tectosilicate, phyllosilicate, etc.), mineral group (e.g., feldspar, zeolite, etc.), mineral species (e.g., prehnite, pumpellyite, etc.), data supplier, and measuring instrument. Measurement conditions, geometries, and sensors are all documented, as is information on sample texture and chemical makeup. Web interfaces to the library are available at http://wwwpds.wustl.edu/missions/mro/spectral_library.htm and http://pdswebapp.wustl.edu/MROCRISMSpectralLibrary/.

## References


Adams, J. (1974), Visible and near-infrared diffuse reflectance spectra of pyroxenes as applied to remote sensing of solid objects n the solar system, *J. Geophys. Res.*, *79*, 4829–4836.

Allen, C., and J. Conca (1991), Weathering of basaltic rocks under cold, arid conditions: Antarctica and Mars, *Proc. Lunar Planet. Sci. Conf.*, *21st*, 711–717.

Arvidson, R. E., F. P. Seelos IV, K. S. Deal, W. C. Koeppen, N. O. Snider, J. M. Kieniewicz, B. M. Hynek, M. T. Mellon, and J. B. Garvin (2003), Mantled and exhumed terrains in Terra Meridiani, Mars, *J. Geophys. Res.*, *108*(E12), 8073, doi:10.1029/2002JE001982.

Arvidson, R. E., et al. (2006), Overview of the Spirit Mars Exploration Rover Mission to Gusev Crater: Landing site to Backstay Rock in the Columbia Hills, *J. Geophys. Res.*, *111*, E02S01, doi:10.1029/2005JE002499.

Bandfield, J. L. (2002), Global mineral distributions on Mars, *J. Geophys. Res.*, *107*(E6), 5042, doi:10.1029/2001JE001510.

Bandfield, J. L., V. E. Hamilton, and P. R. Christensen (2000), A global view of Martian surface compositions from MGS-TES, *Science*, *287*, 1626–1630.

Bandfield, J. L., V. E. Hamilton, P. R. Christensen, and H. Y. McSween Jr. (2004), Identification of quartzofeldspathic materials on Mars, *J. Geophys. Res.*, *109*, E10009, doi:10.1029/2004JE002290.

Banfield, J., B. Jones, and D. Veblen (1991), An AEM-TEM study of weathering and diagenesis, Abert Lake, Oregon. I. Weathering reactions in the volcanics, *Geochim. Cosmochim. Acta*, *55*, 2781–2793.

Bell, J. F., III, T. McCord, and P. Owensby (1990), Observational evidence of crystalline iron oxides on Mars, *J. Geophys. Res.*, *95*, 14,447–14,461.

Bell, J. F., III, et al. (2004a), Pancam multispectral imaging results from the Opportunity rover at Meridiani Planum, *Science*, *306*, 1703–1709.

Bell, J. F., III, et al. (2004b), Pancam multispectral imaging results from the Spirit rover at Gusev Crater, *Science*, *305*, 800–806.

Berkgaut, V., A. Singer, and K. Stahr (1994), Palagonite reconsidered: Paracrystalline illite-smectites from regoliths on basic pyroclastics, *Clays Clay Miner.*, *42*, 582–592.

Berner, R. (1968), Calcium carbonate concretions formed by the decomposition of organic matter, *Science*, *159*, 195–197.

Bibring, J-.P., et al. (2005), Mars surface diversity as revealed by the OMEGA/Mars Express observations, *Science*, *307*, 1576–1581.

Bishop, J. L., S. L. Murchie, C. M. Pieters, and A. P. Zent (2002a), A model for formation of dust, soil, and rock coatings on Mars: Physical and chemical processes on the Martian surface, *J. Geophys. Res.*, *107*(E11), 5097, doi:10.1029/2001JE001581.

Bishop, J. L., et al. (2002b), Geochemical and mineralogical analyses of palagonitic tuffs and altered rinds of pillow lavas on Iceland and applications to Mars, in *Volcano-Ice Interactions on Earth and Mars*, edited by J. L. Smellie and M. G. Chapman, *Geol. Soc. Spec. Publ.*, *202*, 371–392.

Bishop, J. L., et al. (2003), The influence of glassy coatings on volcanic rocks from Mauna Iki, Hawaii and applications to rocks on Mars, *Lunar Planet. Sci.*, *XXXIV*, Abstract 1516.

Bishop, J. L., et al. (2004), Multiple techniques for mineral identification on Mars: A study of hydrothermal rocks as potential analogues for astrobiology sites on Mars, *Icarus*, *169*, 311–323.

Bock, G., and J. Good (1996), *Evolution of Hydrothermal Systems on Earth* (*and Mars?*), 334 pp., John Wiley, Hoboken, N. J.

Boynton, W. V., et al. (2002), Distribution of hydrogen in the near surface of Mars: Evidence for subsurface ice deposits, *Science*, *297*, 81–85.

Bugby, D., J. Garzon, M. Beres, C. Stouffer, D. Mehoke, and M. Wirzburger (2005), Cryogenic diode heat pipe system for cryocooler redundancy, in *Cryogenic Optical Systems and Instruments XI*, edited by J. B. Heaney and L. G. Burriesci, *Proc. SPIE Int. Soc. Opt. Eng.*, *5904*, 321–329.

Byrne, S., and A. P. Ingersoll (2003), A sublimation model for Martian south polar ice features, *Science*, *299*, 1051–1053.

Cabrol, N., and E. Grin (1999), Distribution, classification, and ages of Martian crater lakes, *Icarus*, *142*, 160–172.

Calvin, W. (1997), Variation of the 3-$\mu$m absorption feature on Mars: Observations over eastern Valles Marineris by the Mariner 6 infrared spectrometer, *J. Geophys. Res.*, *102*, 9085–9096.

Cantor, B., M. Malin, and K. S. Edgett (2002), Multiyear Mars Orbiter Camera (MOC) observations of repeated Martian weather phenomena during the northern summer season, *J. Geophys. Res.*, *107*(E3), 5014, doi:10.1029/2001JE001588.

Choo, T. H., S. L. Murchie, and J. S. Jen (2001), The MESSENGER Science Planning Tool, in *Workshop on Mercury: Space Environment, Surface, and Interior*, *LPI Contrib. 1097*, p. 11, Lunar and Planet. Inst., Houston, Tex.

Christensen, P., et al. (2000), Detection of crystalline hematite mineralization on Mars by the Thermal Emission Spectrometer: Evidence for near-surface water, *J. Geophys. Res.*, *105*, 9623–9642.

Christensen, P. R., and H. J. Moore (1992), The Martian surface layer, in *Mars*, edited by H. H. Kieffer et al., pp. 686–729, Univ. of Ariz. Press, Tucson.

Clancy, R. T. (1999), Orbital and interannual variability of the global Mars atmosphere, paper presented at Fifth International Conference on Mars, Lunar and Planet. Inst., Pasadena, Calif., 10–14 July.

Clancy, R. T., and S. Lee (1991), A new look at dust and clouds in the Mars atmosphere: Analysis of emission-phase-function sequences from global Viking IRTM observations, *Icarus*, *93*, 135–158.

Clancy, R. T., S. Lee, G. Gladstone, W. McMillan, and T. Roush (1995), A new model for Mars atmospheric dust based upon analysis of ultraviolet through infrared observations from Mariner 9, Viking, and Phobos, *J. Geophys. Res.*, *100*, 5251–5263.

Clancy, R. T., A. Grossman, M. Wolff, P. James, Y. Billawala, B. Sandor, S. Lee, and D. Rudy (1996), Water vapor saturation at low altitudes around Mars aphelion: A key to Mars climate?, *Icarus*, *122*, 36–62.

Clancy, R. T., B. J. Sandor, M. J. Wolff, P. R. Christensen, M. D. Smith, J. C. Pearl, B. J. Conrath, and R. J. Wilson (2000), An intercomparison of ground-based millimeter, MGS TES, and Viking atmospheric temperature measurements: Seasonal and interannual variability of temperature and dust loading in the global Mars atmosphere, *J. Geophys. Res.*, *105*, 9553–9572.

Clancy, R. T., M. J. Wolff, and P. R. Christensen (2003), Mars aerosol studies with the MGS TES emission phase function observations: Optical depths, particle sizes, and ice cloud types versus latitude and solar longitude, *J. Geophys. Res.*, *108*(E9), 5098, doi:10.1029/2003JE002058.

Cloutis, E., and M. Gaffey (1991), Pyroxene spectroscopy revisited: Spectral-compositional correlations and relationship to geothermometry, *J. Geophys. Res.*, *96*, 22,809–22,826.

Crown, D. A., and R. Greeley (1993), Volcanic geology of Hadriaca Patera and the eastern Hellas region of Mars, *J. Geophys. Res.*, *98*, 3431–3452.

Erard, S., and W. Calvin (1997), New composite spectra of Mars, 0.4–5.7 $\mu$m, *Icarus*, *130*, 449–460.

Erard, S., J.-P. Bibring, J. Mustard, O. Forni, J. Head, S. Hurtrez, Y. Langevin, C. Pieters, J. Rosenqvist, and C. Sotin (1991), Spatial variations in composition of the Valles Marineris and Isidis Planitia regions of Mars derived for ISM spectra, *Proc. Lunar Planet. Sci. Conf.*, *21st*, 437–455.

Erard, S., J. Mustard, S. Murchie, J.-P. Bibring, P. Cerroni, and A. Coradini (1994), Martian aerosols: Near-infrared spectral properties and effects on the observation of the surface, *Icarus*, *111*, 317–337.

Eugster, H., and L. Hardie (1978), Saline lakes, in *Lakes: Chemistry, Geology, Physics*, edited by A. Lerman, pp. 237–273, Springer, New York.

Farmer, J. (1998), Thermophiles, early biosphere evolution, and the origin of life on Earth, in *The Search for Life on Mars*, edited by J. Hiscox, pp. 58–65, Br. Interplanet. Soc., London.

Farmer, J., and D. Des Marais (1999), Exploring for a record of ancient Martian life, *J. Geophys. Res.*, *104*, 26,977–26,995.

Farrand, W., and R. Singer (1991), Spectral analysis and mapping of palagonite tuffs of Pavant Butte, Millard County, Utah, *Geophys. Res. Lett.*, *18*, 2237–2240.

Feldman, W. C., et al. (2002), Global distribution of neutrons from Mars: Results from Mars Odyssey, *Science*, *297*, 75–78.

Forsythe, R. (1990), A case for Martian salars and saline lakes during the Noachian, *Lunar Planet. Sci.*, *XXI*, 379–380.

Forsythe, R., and C. Blackwelder (1998), Closed drainage crater basins of the Martian highlands: Constraints on the early Martian hydrologic cycle, *J. Geophys. Res.*, *103*, 31–41.

Gendrin, A., et al. (2005), Sulfates in Martian layered terrains: The OMEGA/Mars Express view, *Science*, *307*, 1587–1591.
Gíslason, S., and S. Arnórsson (1990), Saturation state of natural waters in Iceland relative to primary and secondary minerals in basalt, in *Fluid-Mineral Interactions: A Tribute to H. P. Eugster*, edited by J. Spencer and I.-M. Chou, *Spec. Publ. Geochem. Soc.*, *2*, 373–393.
Gíslason, S., and H. Eugster (1989), Meteoric water-basalt interaction. II. A field study in N. E. Iceland, *Geochim. Cosmochim. Acta*, *51*, 2841–2855.
Greeley, R., and J. Guest (1987), Geologic map of the eastern equatorial region of Mars. *U.S. Geol. Surv. Misc. Invest. Ser.*, *Map I-1038*.
Greeley, R., and P. Spudis (1981), Volcanism on Mars, *Rev. Geophys.*, *19*, 13–41.
Green, R. O., M. L. Eastwood, and C. M. Sarture (1998), Imaging spectroscopy and the Airborne Visible Infrared Imaging Spectrometer (AVIRIS), *Remote Sens. Environ.*, *65*, 227–248.
Grotzinger, J. P., et al. (2005), Stratigraphy, sedimentology and depositional environment of the Burns Formation, Meridiani Planum, Mars, *Earth Planet. Sci. Lett.*, *240*, 11–72.
Hall, L., R. Beebe, and B. Knopf (2005), Planetary Data System Archive Preparation Guide, *JPL Doc. D-31224*, Jet Propul. Lab., Pasadena, Calif.
Hamilton, V. E., and P. R. Christensen (2005), Evidence for extensive, olivine-rich bedrock on Mars, *Geology, 33*, 433–436.
Hamilton, V. E., P. R. Christensen, H. Y. McSween, and J. L. Bandfield (2003), Searching for the source of the Martian meteorites using MGS TES: Integrating Martian meteorites into the global distribution of igneous materials on Mars, *Meteorit. Planet. Sci.*, *38*, 871–885.
Hay, R., and R. Sheppard (1977), Zeolites in open hydrologic systems, in *Mineralogy and Geology of Natural Zeolites*, edited by J. Boles et al., pp. 93–102, Mineral. Soc. of Am., Washington, D. C.
Hoefen, T. M., R. N. Clark, J. L. Bandfield, M. D. Smith, J. C. Pearl, and P. R. Christensen (2003), Discovery of olivine in the Nili Fossae region of Mars, *Science*, *302*, 627–630.
Horodyski, L., and R. Knauth (1994), Life on land in the Precambrian, *Science*, *263*, 494–498.
Houck, J., J. Pollack, C. Sagan, D. Schaak, and J. Decker (1973), High altitude spectroscopic evidence for bound water on Mars, *Icarus*, *18*, 470–480.
Jakosky, B., and C. Farmer (1982), The seasonal and global behavior of water vapor in the Mars atmosphere: Complete global results from the Viking atmospheric water detector experiment, *J. Geophys. Res.*, *87*, 2999–3019.
Jakosky, B., and R. Haberle (1992), The seasonal behavior of water on Mars, in *Mars*, edited by H. Kieffer et al., pp. 969–1016, Univ. of Ariz., Tucson.
Joshi, M. M., R. M. Haberle, and R. T. Clancy (2003), Modelling the annual cycle of carbon monoxide in the Martian atmosphere, paper presented at Mars Atmosphere Modelling and Observations, Cent. Natl. d'Etudes Spatiales, Granada, Spain.
Jouglet, D., F. Poulet, J. Mustard, R. Milliken, J. P. Bibring, Y. Langevin, and B. Gondet (2006), Observation of 3 $\mu$m hydration feature on Mars from OMEGA/Mars Express data, *Lunar Planet. Sci.*, *XXXVII*, Abstract 1741.
Kahn, R., T. Martin, R. Zurek, and S. Lee (1992), The Martian dust cycle, in *Mars*, edited by H. Kieffer et al., pp. 1017–1053, Univ. of Ariz., Tucson.
Kieffer, H., and T. Titus (2001), TES mapping of Mars' north seasonal cap, *Icarus*, *154*, 162–180.
Kieffer, H. H., T. N. Titus, K. F. Mullins, and P. R. Christensen (2000), Mars south polar spring and summer behavior observed by TES: Seasonal cap evolution controlled by frost grain size, *J. Geophys. Res.*, *105*, 9653–9700.
Kirkland, L, J. Salisbury, J. Mustard, R. Clark, P. Lucey, and S. Murchie (1999), Spectroscopy of the Martian surface: What next?, *LPI Contrib. 1149*, Lunar and Planet. Inst., Houston, Tex.
Kirkland, L., K. Herr, E. Keim, J. Salisbury, and J. Hackwell (2000), A field study of thermal infrared spectra of carbonates, with implications for studies of Mars, *Lunar Planet. Sci.*, *XXII*, 1876.
Klingelhöfer, G., et al. (2005), MIMOS II on MER—One year of Mössbauer spectroscopy on the surface of Mars: From jarosite at Meridiani Planum to goethite at Gusev Crater, *Lunar Planet. Sci.*, *XXXVI*, 2349.
Kodama, H., C. DeKimpe, and J. Dejou (1988), Ferrian saponite in a gabbro saprolite at Mont Mégantic, Quebec, *Clays Clay Miner.*, *36*, 102–110.
Kraft, D., T. G. Sharp, and J. R. Michalski (2003), Thermal emission spectra of silica-coated basalt and considerations for Martian surface morphology, *Lunar Planet. Sci.* [CD-ROM], *XXXIV*, Abstract 1420.
Kristmannsdóttir, H. (1982), Alteration in the IRDP drill hole compared with other drill holes in Iceland, *J. Geophys. Res.*, *87*, 6525–6531.
Langevin, Y., F. Poulet, J.-P. Bibring, and B. Gondet (2005a), Sulfates in the north polar region of Mars detected by OMEGA/Mars Express, *Science*, *307*, 1584–1586.
Langevin, Y., F. Poulet, J.-P. Bibring, B. Schmitt, S. Douté, and B. Gondet (2005b), Summer evolution of the north polar cap of Mars as observed by OMEGA/Mars Express, *Science*, *307*, 1581–1584.
Lees, J., E. Schaefer, and M. Fasold (2005), Design of the CRISM cryogenic system and focal plane assembly isolation system, in *Optomechanics 2005*, edited by A. E. Hatheway, *Proc. SPIE Int. Soc. Opt. Eng.*, *5877*, 265–275.
Malin, M. C., and K. S. Edgett (2001), Mars Global Surveyor Mars Orbiter Camera: Interplanetary cruise through primary mission, *J. Geophys. Res.*, *106*(E10), 23,429–23,570.
Malin, M. C., et al. (2007), Context Camera Investigation on board the Mars Reconnaissance Orbiter, *J. Geophys. Res.*, doi:10.1029/2006JE002808, in press.
Mars Exploration Payload Analysis Group (MEPAG) (2004), Scientific Goals, Objectives, Investigations, and Priorities: 2003, analysis report, Natl. Aeronaut. and Space Admin., Washington, D. C. (Available at http://mepag.jpl.nasa.gov/reports/index.html)
McCleese, D. J., J. T. Schofield, F. W. Taylor, S. B. Calcutt, M. C. Foote, D. M. Kass, C. B. Leovy, D. A. Paige, P. L. Read, and R. W. Zurek (2007), Mars Climate Sounder: An investigation of thermal and water vapor structure, dust and condensate distributions in the atmosphere, and energy balance of the polar regions, *J. Geophys. Res.*, doi:10.1029/2006JE002790, in press.
McEwen, A., M. Malin, M. Carr, and W. Hartmann (1999), Voluminous volcanism revealed on early Mars, *Nature*, *387*, 584–586.
McEwen, A. S., et al. (2007), Mars Reconnaissance Orbiter's High Resolution Imaging Science Experiment (HiRISE), *J. Geophys. Res.*, doi:10.1029/2005JE002605, in press.
McLennan, S. M., et al. (2005), Provenance and diagenesis of the evaporate-bearing Burns formation, Meridiani Planum, Mars, *Earth Planet. Sci. Lett.*, *240*, 95–121.
McSween, H. Y., Jr., et al. (1999), Chemical, multispectral, and textural constraints on the composition and origin of rocks at the Mars Pathfinder landing site, *J. Geophys. Res.*, *104*(E4), 8679–8716.
McSween, H. Y., Jr., T. L. Grove, and M. B. Wyatt (2003), Constraints on the composition and petrogenesis of the Martian crust, *J. Geophys. Res.*, *108*(E12), 5135, doi:10.1029/2003JE002175.
Mehegan, J., J. Robinson, and J. Delaney (1982), Secondary mineralization and hydrothermal alteration in the Reydarfjordur Drill Core, East Iceland, *J. Geophys. Res.*, *87*, 6511–6524.
Milliken, R. E., J. F. Mustard, F. Poulet, J.-P. Bibring, Y. Langevin, B. Gondet, S. Pelkey, and the Mars Express OMEGA Team (2006), The $H_2O$ content of the Martian surface as seen by Mars Express OMEGA, *Lunar Planet. Sci.*, *XXXVII*, Abstract 1987.
Minitti, M. E., J. F. Mustard, and M. J. Rutherford (2002), Effects of glass content and oxidation on the spectra of SNC-like basalts: Applications to Mars remote sensing, *J. Geophys. Res.*, *107*(E5), 5030, doi:10.1029/2001JE001518.
Moroz, V. (1964), The infrared spectrum of Mars (1.1–4.1 $\mu$m), *Sov. Astron.*, *8*, 273–281.
Morris, R. V., et al. (2001), Phyllosilicate-poor palagonitic dust from Mauna Kea volcano (Hawaii): A mineralogical analogue for magnetic Martian dust?, *J. Geophys. Res.*, *106*, 5057–5083.
Morris, R. V., T. G. Graff, S. A. Mertzman, M. D. Lane, and P. R. Christensen (2003), Palagonitic Mars from rock rinds to dust: Evidence from visible, near-IR, and thermal emission spectra of poorly crystalline materials, in *Lunar Planet. Sci.* [CD-ROM], *XXXIV*, Abstract 1874.
Morris, R. V., et al. (2004), Mineralogy at Gusev Crater from the Mössbauer Spectrometer on the Spirit Rover, *Science*, *305*, 833–836.
Murchie, S., J. Mustard, J. Bishop, J. Head, C. Pieters, and S. Erard (1993), Spatial variations in the spectral properties of bright regions on Mars, *Icarus*, *105*, 454–468.
Murchie, S., L. Kirkland, S. Erard, J. Mustard, and M. Robinson (2000), Near-infrared spectral variations of Martian surface materials from ISM imaging spectrometer data, *Icarus*, *147*, 444–471.
Murchie, S., O. Barnouin-Jha, K. Barnouin-Jha, J. Bishop, J. Johnson, H. McSween, and R. V. Morris (2004), Old desert varnish-like coatings and young breccias at the Mars Pathfinder landing site, *Lunar Planet. Sci.*, *XXXV*, Abstract 1740.
Murchie, S., E. Guinness, and S. Slavney (2006), CRISM Data Product Software Interface Specification, Natl. Aeronaut. and Space Admin., Washington, D. C. (Available at http://wwwpds.wustl.edu/missions/mro/index.htm)
Mustard, J., and S. Murchie (2001), Unusual spectral properties observed in Valles Marineris, *Lunar Planet. Sci.*, *XXXII*, 2194.
Mustard, J., and C. Pieters (1987), Quantitative abundance estimates from bidirectional reflectance measurements, Proc. Lunar Planet. Sci. Conf. 17th, Part 2, *J. Geophys. Res.*, *92*, supp., E617–E626, suppl.

Mustard, J. F., S. Erard, J.-P. Bibring, J. W. Head, S. Hurtrez, Y. Langevin, C. M. Pieters, and C. J. Sotin (1993), The surface of Syrtis Major: Composition of the volcanic substrate and mixing with altered dust and soil, *J. Geophys. Res.*, *98*, 3387–3400.

Mustard, J., S. Murchie, S. Erard, and J. Sunshine (1997), In situ compositions of Martian volcanics: Implications for the mantle, *J. Geophys. Res.*, *102*, 25,605–25,615.

Mustard, J. F., F. Poulet, A. Gendrin, J.-P. Bibring, Y. Langevin, B. Gondet, N. Mangold, G. Bellucci, and F. Altieri (2005), Olivine and pyroxene diversity in the crust of Mars, *Science*, *307*, 1594–1597.

Nedell, S., S. S. Squyres, and D. Andersen (1987), Origin and evolution of the layered deposits in the Valles Marineris, Mars, *Icarus*, *70*, 409–441.

Pelkey, S. M., et al. (2007), CRISM multispectral summary products: Parameterizing mineral diversity on Mars from reflectance, *J. Geophys. Res.*, doi:10.1029/2006JE002831, in press.

Pimental, G., P. Forney, and K. Herr (1974), Evidence about hydrate and solid water in the Martian surface from the 1969 Mariner infrared spectrometer, *J. Geophys. Res.*, *79*, 1623–1634.

Poulet, F., J.-P. Bibring, J. F. Mustard, A. Gendrin, N. Mangold, Y. Langevin, R. E. Arvidson, B. Gondet, C. Gomez, and the OMEGA Team (2005a), Phyllosilicates on Mars and implications for the early Mars history, *Nature*, *438*, 570–571.

Poulet, F., Y. Langevin, J.-P. Bibring, B. Gondet, R. E. Arvidson, and the OMEGA Team (2005b), Mineralogy of the northern high latitude regions of Mars, *Lunar Planet. Sci.*, *XXXVI*, 1828.

Presley, M., and R. Arvidson (1988), Nature and origin of materials exposed in the Oxia Palus–Western Arabia–Sinus Meridiani region, Mars, *Icarus*, *75*, 499–517.

Robert, C., and B. Goffé (1993), Zeolitization of basalts in subaqueous freshwater settings: Field observations and experimental study, *Geochim. Cosmochim. Acta*, *57*, 3597–3612.

Robinson, M. S., E. Malaret, and T. White (2003), A radiometric calibration for the Clementine HIRES camera, *J. Geophys. Res.*, *108*(E4), 5028, doi:10.1029/2000JE001241.

Rodin, A., R. T. Clancy, R. Wilson, and M. Richardson (1999), Dynamical properties of Mars water ice clouds and their interactions with atmospheric dust and radiation, *Adv. Space Res.*, *23*, 1577–1585.

Schmitt, B., S. Douté, Y. Langevin, F. Forget, J.-P. Bibring, B. Gondet, and the OMEGA Team (2005), Northern seasonal condensates on Mars by OMEGA/Mars Express, *Lunar Planet. Sci.*, *XXXVI*, 2326.

Scott, D., and K. Tanaka (1986), Geologic map of the western equatorial region of Mars, *U.S. Geol. Surv. Misc. Invest. Ser.*, *Map I-1802–A*.

Seu, R., et al. (2007), SHARAD sounding radar on the Mars Reconnaissance Obiter, *J. Geophys. Res.*, doi:10.1029/2006JE002745, in press.

Shau, Y., and D. Peacor (1992), Phyllosilicates in hydrothermally altered basalts from DSDP Hole 504B, Leg 83—A TEM and AEM study, *Contrib. Mineral. Petrol.*, *112*, 119–133.

Sherman, D., R. Burns, and V. Burns (1982), Spectral characteristics of the iron oxides with application to the Martian bright region mineralogy, *J. Geophys. Res.*, *87*, 10,169–10,180.

Silverglate, P. R., and D. E. Fort (2004), System design of the CRISM (Compact Reconnaissance Imaging Spectrometer for Mars) hyperspectral imager, in *Imaging Spectrometry IX*, edited by S. S. Shen and P. E. Lewis, *Proc. SPIE Int. Soc. Opt. Eng.*, *5159*, 283–290.

Singer, R., T. McCord, R. Clark, J. Adams, and R. Huguenin (1979), Mars surface composition from reflectance spectroscopy: A summary, *J. Geophys. Res.*, *84*, 8415–8426.

Smith, M. D. (2002), The annual cycle of water vapor on Mars as observed by the Thermal Emission Spectrometer, *J. Geophys. Res.*, *107*(E11), 5115, doi:10.1029/2001JE001522.

Smith, M. D. (2004), Interannual variability in TES atmospheric observations of Mars during 1999–2003, *Icarus*, *167*, 148–165.

Smith, M., J. Pearl, B. Conrath, and P. Christensen (2001), Thermal Emission Spectrometer results: Mars atmospheric thermal structure and aerosol distribution, *J. Geophys. Res.*, *106*, 23,929–23,945.

Smith, M. D., J. L. Bandfield, P. R. Christensen, and M. I. Richardson (2003), Thermal Emission Imaging System (THEMIS) infrared observations of atmospheric dust and water ice cloud optical depth, *J. Geophys. Res.*, *108*(E11), 5115, doi:10.1029/2003JE002115.

Squyres, S. W., et al. (2004a), The Spirit rover's Athena science investigation at Gusev Crater, Mars, *Science*, *305*(5685), 794–799.

Squyres, S. W., et al. (2004b), The Opportunity rover's Athena science investigation at Meridiani Planum, Mars, *Science*, *306*(5702), 1698–1703.

Stamnes, K., S. Tsay, W. Wiscombe, and K. Jayaweera (1988), Numerically stable algorithm for discrete-ordinate-method radiative transfer in multiple scattering and emitting layered media, *Appl. Opt.*, *27*, 2502.

Sunshine, J., C. Pieters, and S. Pratt (1990), Deconvolution of mineral absorption bands: An improved approach, *J. Geophys. Res.*, *95*, 6955–6966.

Surdam, R. (1977), Zeolites in closed hydrologic systems, in *Mineralogy and Geology of Natural Zeolites*, edited by J. Boles et al., pp. 65–92, Mineral. Soc. of Am., Washington, D. C.

Swayze, G. A., R. N. Clark, A. F. H. Goetz, T. G. Chrien, and N. S. Gorelick (2003), Effects of spectrometer band pass, sampling, and signal-to-noise ratio on spectral identification using the Tetracorder algorithm, *J. Geophys. Res.*, *108*(E9), 5105, doi:10.1029/2002JE001975.

Titus, T. N., H. H. Kieffer, K. F. Mullins, and P. R. Christensen (2001), TES premapping data: Slab ice and snow flurries in the Martian north polar night, *J. Geophys. Res.*, *106*, 23,181–23,196.

Titus, T. N., H. H. Kieffer, and P. R. Christensen (2003), Exposed water ice discovered near the south pole of Mars, *Science*, *299*, 1048–1051.

Tomasko, M., L. Doose, M. Lemmon, P. Smith, and E. Wegryn (1999), Properties of dust in the Martian atmosphere from the Imager on Mars Pathfinder, *J. Geophys. Res.*, *104*, 8987–9007.

Troll, J., P. Thompson, and D. Humm (2005), Boresight and gimbal axis alignment for the CRISM instrument, in *Optomechanics 2005*, edited by A. E. Hatheway, *Proc. SPIE Int. Soc. Opt. Eng.*, *5877*, 93–101.

Wagner, C., and U. Schade (1996), Measurements and calculations for estimating the spectrometric detection limit for carbonates in Martian soils, *Icarus*, *123*, 256–268.

Wang, A., et al. (2005), Sulfate deposition in regolith exposed in trenches on the plains between the Spirit landing site and Columbia Hills in Gusev Crater, Mars, *Lunar Planet. Sci.*, *XXXVI*, 2236.

Wilson, D., P. Maker, R. Muller, P. Mouroulis, and J. Backlund (2003), Recent advances in blazed grating fabrication by electron-beam lithography, in *Current Developments in Lens Design and Optical Engineering IV*, edited by P. Mouroulis, W. Smith, and R. Johnson, *Proc. SPIE Int. Soc. Opt. Eng.*, *5173*, 115–126.

Wolff, M. J., and R. T. Clancy (2003), Constraints on the size of Martian aerosols from Thermal Emission Spectrometer observations, *J. Geophys. Res.*, *108*(E9), 5097, doi:10.1029/2003JE002057.

Wyatt, M., and H. McSween (2002), Spectral evidence for weathered basalt as an alternative to andesite in the northern lowlands of Mars, *Nature*, *417*, 263–266.

Zurek, R. W., and S. E. Smrekar (2007), An overview of the Mars Reconnaissance Orbiter (MRO) science mission, *J. Geophys. Res.*, doi:10.1029/2006JE002701, in press.

Zurek, R., J. Barnes, R. Haberle, J. Pollack, J. Tillman, and C. Leovy (1992), Dynamics of the atmosphere of Mars, in *Mars*, edited by H. Kieffer et al., pp. 835–933, Univ. of Ariz., Tucson.

Zurek, R., et al. (2001), Report of the NASA Science Definition Team for the Mars Reconnaissance Orbiter (MRO), Sci. Definition Team, Natl. Aeronaut. and Space Admin., Washington, D. C, 9 Feb.

R. Arvidson, E. Guinness, P. McGuire, and S. Slavney, Department of Earth and Planetary Sciences, Washington University, Campus Box 1169, One Brookings Drive, St. Louis, MO 63130, USA.

P. Bedini, K. Beisser, J. Boldt, P. Cavender, T. Choo, E. H. Darlington, D. Fort, J. Hayes, K. Heffernan, J. Hemmler, G. Heyler, D. Humm, J. Hutcheson, N. Izenberg, R. Lee, J. Lees, D. Lohr, J. A. McGovern, S. Murchie, E. Rhodes, E. Schaefer, G. Seagrave, F. Seelos, W.-J. Shyong, P. Silverglate, K. Strohbehn, H. Taylor, P. Thompson, B. Tossman, and M. Wirzburger, Applied Physics Laboratory, 11100 Johns Hopkins Road, Room MP3-W165, Laurel, MD 20723, USA. (scott.murchie@jhuapl.edu)

J.-P. Bibring, Institut d'Astrophysique Spatiale, Batiment 120, Orsay Cedex F-91405, France.

J. Bishop, D. Des Marais, and T. Roush, NASA Ames Research Center, Moffett Field, CA 94035, USA.

R. T. Clancy and M. Wolff, Space Science Institute, 4750 Walnut Street, Suite 205, Boulder, CO 80301, USA.

R. Espiritu, C. Hash, and E. Malaret, Applied Coherent Technology, Herndon, VA 20170, USA.

R. Green and T. Martin, NASA Jet Propulsion Laboratory, Mail Stop 306-438, 4800 Oak Grove Drive, Pasadena, CA 91109, USA.

R. Morris, NASA Johnson Space Center, Houston, TX 77058, USA.

J. Mustard and S. Pelkey, Department of Geological Sciences, Brown University, 324 Brook Street, Campus Box 1846, Providence, RI 02912, USA.

M. Robinson, Center for Planetary Sciences, Northwestern University, Locy Hall 309, 1850 Campus Drive, Evanston, IL 60208, USA.

M. Smith, NASA Goddard Space Flight Center, Greenbelt, MD 20771, USA.